Growth, Integration, and Functional Characterization of AlScN Thin Films for RF MEMS Devices

Thèse N° 9188

Présentée le 22 février 2019

à la Faculté des sciences et techniques de l'ingénieur
Laboratoire de céramique
Programme doctoral en science et génie des matériaux

pour l'obtention du grade de Docteur ès Sciences

par

FAZEL PARSAPOUR

Acceptée sur proposition du jury

Dr S. Mischler, président du jury
Prof. P. Muralt, directeur de thèse
Dr M. Moridi, rapporteur
Dr T. Metzger, rapporteur
Prof. G. Villanueva, rapporteur

2019

ÉCOLE POLYTECHNIQUE
FÉDÉRALE DE LAUSANNE

Acknowledgements

I would like to thank Professor Paul Muralt, for offering me the opportunity to do my Ph.D. thesis with his group, and for his constant support and scientific expertise throughout the thesis years. I highly respect his deep knowledge of the field. Much less would have been achieved if it were not for his supervision.

I would like to thank the members of the jury, Dr. Stefano Mischler, Prof. Paul Muralt, Prof. Guillermo Villanueva, Dr. Thomas Metzger, and Dr. Mohesn Moridi for reviewing and evaluating my thesis.

I acknowledge the support of the RF360, joint venture of Qualcomm and TDK, Carinthian Tech Research AG (CTR), and Hasler foundation for funding this thesis.

I am very grateful to Professors Dragan Damjanovic who was always available and patient enough to answer my questions, and helped me greatly in my understanding of the difficult physics of piezoelectricity and acoustic waves in solids.

I would not have been successful in my work without the support of Ramin Matloub, my senior in Paul's group on all matters of experimental work, material behavior, and fabrication. I would like to thank him for constant availability, help, and friendship. I am also very much indebted to Vladimir Pashchenko who taught me a lot on acoustic waves physic in solid mediums and modeling of complex acoustic devices.

I am also very thankful to my colleagues of the Electroceramic thin films group, which I always learned from discussing with them: Robin Nigon, Daesung Park, Xiao Di, and especially my office mates Mahmoud Hadad, Stefan Mertin and Vladimir Pashchenko. Great thanks to my former colleagues, Cosmin Sandu, for all the TEM imaging in this work and to Elmira Shahrabi for all her kind supports, and Sina Hashemizadeh for our old friendship from the bachelor studies in the University of Tehran up to the common Ph.D time at EPFL.

I am also very thankful of my dear friend Ebrahim Jahanbaksh for reviewing the manuscript and for all his constant support and friendship in the last seven years. I would also like to thank Seyed Mohammad Hashemi, Hasan Pezeshgi

and Hamza Herkus who kindly accepted to review parts of the manuscript. Their precious comments greatly improved the quality of the final text.

I would like to deeply thank my dear friend Marie Simon for her valuable support and kindness to me and my family and also for the French version of the abstract.

Finally, I express my deepest gratitude to my parents Shahrzad and Barat, my sisters Khadijeh and Hadis and my brother, the solid support of my life, Rasoul. My heart is always warm by their unconditional love.

Last but not least, I would like to thank my beloved wife Fatemeh for her constant and unconditional love, support, inspiration, and patience. Nothing is difficult to reach with her presence. In particular, I am very grateful to her for taking care of our lovely daughter, Samieh, during the last ten months. She did that almost all on her own and shared only Samieh's happy moments with me.

Abstract

Mobile communication has grown explosively in recent years, leading to a strong demand for cheap, but high-performing bandpass filters with low insertion loss and smaller size. Surface acoustic wave (SAW) and thin film bulk acoustic wave (BAW) resonators realized with piezoelectric materials are currently the only ones used in radio frequency (RF) passband filters for mobile communication in the LTE bands situated in the range of 0.3 to 3 GHz. SAW devices are more suitable for the lower frequency range, while BAW devices are more suited for the higher frequency range. It is of high interest to dispose of a micro resonator type that would combine the advantages of these two technologies, and that would cover the complete frequency range. The lowest order symmetric Lamb wave mode (S_0) propagating in a thin film structure appears to be a good solution for this challenge. The frequency is mostly defined by the periodicity of an interdigitated electrode system, and to a lesser extent by the thickness of the piezoelectric thin film. Realizations with AlN thin films were studied since 2002. Advantageous properties of such devices were demonstrated. However, only moderate electromechanical coupling factors (k^2) of around 1%, combined with too low quality factors (Q) were achieved. The so-called figure of merit (FoM) for filter applications, Qk^2, turned out to be much too low and never achieved more than 8.

Recently, it was shown that the piezoelectric coefficients of the wurtzite structure AlN can be strongly increased by partial substitution of Al by Sc. In this work, we investigated Lamb wave resonators (LWR) by theory and experiment using thin films of $Al_xSc_{1-x}N$ with Sc concentrations of x = 0.15, and 0.3 for application frequencies around 1.4 GHz. The device design contained a floating bottom electrode and an interdigitated top electrode. Free standing (free LWR) and solidly mounted (SM-LWR) LWRs were studied. The latter were grown on an acoustic Bragg mirror containing 5 alternating layers of SiO_2 and W. The free LWRs based on 15% AlScN thin films showed k^2 values of typically 2.5%, which clearly shows the enhanced piezoelectric response of Sc doped AlN. However, the moderate quality factor in the range of 200 to 400 resulted in a FoM that again did not exceed 8. However, the SM-LWR has lead to a significantly enhanced Q factor, while k^2 was

almost unchanged. With a Q of 1300, and a k^2 of 2.3% , a FoM of 30 was reached.

We could further improve the results by increasing the Sc content to 30%. An impressive FoM of 70 (Q=1350, k^2=5.2%) was achieved with the SMR-LWR. Using AlN instead of W in the Bragg reflector has resulted in a FoM of 59 (Q=1300, k^2=4.6%). These FoM values are by far the best ones ever achieved in MEMS-type LWRs.

The design of LWRs requires a full set of elastic, dielectric, and piezoelectric material constants. Shape resonators vibrating at well-defined modes constitute the most precise tools for their derivation. We designed and fabricated dual mode BAW resonators for the extraction of longitudinal constants (c_{33}^E, e_{33}) and shear mode constants (c_{44}^E, e_{15}). The AlScN thin film grew in a slightly tilted c-axis texture during the first 200 nm, as planned. But then, massive secondary nucleation lead to a film dominated by abnormally oriented grains. Combining TEM nano diffraction mapping and finite element modelling, we nevertheless managed to derive the targeted material constants.

Abstract

La communication mobile croît rapidement ces temps, créant une forte demande de filtres passe-bande peu chers, mais trés performants, à perte d'insertion faible et de taille réduite. Les SAW, convenant mieux à une plage de fréquences inférieure, et les BAW à une plage supérieure, réalisés avec des matériaux piézoélectriques sont les seuls utilisés dans les filtres passe-bande RF pour la communication mobile dans les bandes LTE situées à certaines fréquences, comprises entre 0.3 à 3 GHz.

Il est intéressant de disposer de micro résonateurs combinant les avantages de ces deux technologies et couvrant toute la gamme de fréquences. Le S_0 se propageant dans une structure à couche mince semble être réponse à ce problème. La fréquence se définit notamment par la périodicité d'un système d'électrodes interdigitées et, dans une moindre mesure, par l'épaisseur du film mince piézoélectrique. On étudie les réalisations à films minces AlN depuis 2002. Les avantages de tels dispositifs sont démontrés. Mais seuls ont été atteints des facteurs de couplage électromécaniques modérés (k^2) d'environ 1%, associés á des facteurs de qualité trop faibles (Q). Le FoM pour les applications de filtrage, Qk^2, s'est avéré beaucoup trop bas et n'a jamais atteint plus de 8.

Récemment, il a été montré que les coefficients piézoélectriques de la structure de wurtzite AlN peuvent être fortement augmentés par substitution partielle de Al par Sc.

Ici, nous avons étudié les résonateurs à ondes de Lamb (LWR) en théorie et en pratique en utilisant des couches minces de AlxSc1-xN avec des concentrations de Sc de x = 0.15 et 0.3 pour des fréquences dapplication proches de 1.4 GHz. L'appareil contient une électrode inférieure flottante et une électrode supérieure interdigitée. Des LWR libres et des LWR solidement montés (SM-LWR) ont été étudiés. Les SM-LWR ont été cultivés sur un miroir de Bragg acoustique contenant 5 couches alternées de SiO_2 et de W. Les LWR libres basés sur des films minces de 15% d'AlScN ont montré des valeurs de k^2 typiquement de 2.5%, soit une nette amélioration de la réponse piézoélectrique de l'AlN dopé Sc. Cependant, le facteur de qualité modéré dans la gamme de 200 à 400 a donné un FoM nexcédant toujours pas 8. Toutefois, le SM-LWR a mené à un facteur Q considérablement amélioré,

alors que k^2 était presque inchangé. Avec un Q de 1300 et un k^2 de 2.3%, un FoM de 30 a été atteint.

Améliorons encore les résultats en augmentant le contenu en Sc à 30%. Avec un SM-LWR, nous obtenons un joli FoM de 70 (Q = 1350, k^2 = 5.2%). L'utilisation de AlN au lieu de W dans le réflecteur de Bragg a donné un FoM de 59 (Q = 1300, k^2 = 4.6%). Ces FoM sont de loin les meilleurs jamais atteints dans les LWR de type MEMS. Les LWR nécessitent un ensemble complet de constantes de matériau élastique, diélectrique et piézoélectrique. Les résonateurs de forme vibrant selon des modes bien définis constituent les outils les plus précis pour leur dérivation. Nous avons conu et fabriqué des résonateurs BAW bimodes pour l'extraction de constantes longitudinales (c_{33}^E, e_{33}) et de constantes de mode cisaillement (c_{15}^E, e_{33}). Le film mince AlScN s'est développé selon une texture d'axe c légèrement inclinée dans les 200 premiers nm, comme prévu. Mais après, la nucléation secondaire massive a conduit à un film dominé par des grains anormalement orientés. En combinant la cartographie par nanodiffraction et la FEM, nous avons néanmoins réussi à dériver les constantes de matériau ciblées.

Contents

List of Figures

List of Tables

Chapter 1

Introduction, Background and Objectives

1.1 Bandpass Filters

Mobile communication systems operating at radio frequencies (RF) of 0.8 to 6 GHz have grown significantly in the last decades. These systems continuously demand cheaper bandpass filters with higher performance and smaller size. The filters must transmit/receive signals within a particular bandwidth at a certain frequency and suppress the rest. A vast range of applications including mobile telecommunication systems (GSM, UMTS, LTE), global positioning systems (GPS), data transfer technologies (Bluetooth, Wireless Local Area Network WLAN), etc. are employing such filters. Figure 1.1 shows a simplified schematic view of a bandpass filter usage in a GSM and in CDMA mobile phones. Even more filters are needed in a real mobile phone. However, the detailed architecture of mobile phones is outside the scope of this thesis. Nowadays a smart-phone communicates in several GSM and LTE bands. For instance, Apple's iPhones starting from version 6 work in GSM bands at GSM 850 / 900 / 1800 / 1900 and in several LTE bands ranging from 850 to 2100 MHz. These devices also communicate with WLAN and Bluetooth technologies as well. A vast number of miniaturized high-performance RF filters are employed to create such a communicative device.

An electromagnetic wave oscillating at 1GHz has wavelength around 30cm in the air. This value is reduced to half (15cm) for the same wave at 2GHz. Filtering equipment of such signals must have comparable size to the wavelength of the carrier wave. Transforming the electromagnetic wave to an acoustic wave is the key to filter GHz range signals by microacoustic filters. The typical propagation velocity of acoustic waves in solids is in the range of 3000-11000 m/s, which is five

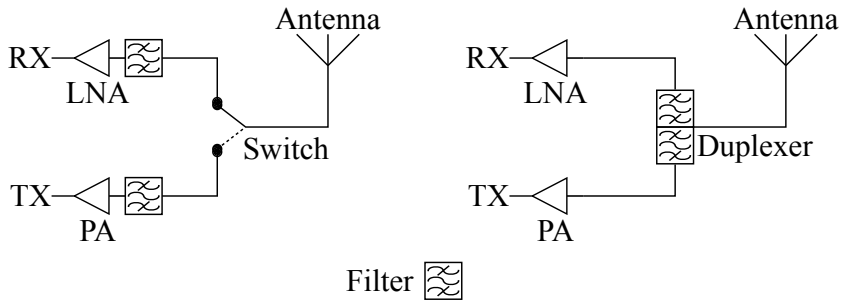

Figure 1.1: Pass-band filters in the front-end of a GSM phone (left) and a CDMA phone (right). RX stands for receive path and TX for transmitting path.

order of magnitude less than electromagnetic propagation velocity. The wavelength is reduced accordingly to micrometer range for GHz-range frequencies. Thus, sub-millimeter acoustic filters could be fabricated to filter signals oscillating in the GHz range.

1.2 Piezoelectric RF-Filters

1.2.1 Piezoelectricity

Piezoelectricity is the ability of a material to acquire electrical charge under mechanical stress, and vice versa. The word "Piezoelectricity" originated from the Greek word "Piezen" which means "to press". The effect discovered by Jacques and Pierre Curie in 1880 [1]. Applying an electric field to these materials changes the mechanical dimensions. Conversely, applying a mechanical constraint induces an electrical field in the material. Generating and collecting acoustic waves are the major applications of the piezoelectric materials. The absence of an inversion symmetry is the key characteristic in the lattice of a piezoelectric material. It leads to a linear relation between electrical and mechanical quantities of the form $D = d \times T$ (direct effect) and $S = d \times E$ (converse effect). It allows for a bilinear coupling in the thermodynamic potential of the piezoelectric material. Considering the electric field E_i, stress T_{ij} and temperature θ as independent variables, the Gibbs free energy G of a dielectric is written as:

$$G = U - \sigma\theta - S_{ij}T_{ij} - D_i - E_i \tag{1.1}$$

where U, σ, S_{ij}, and D_i represent the internal energy of the system, the entropy, the strain, and the dielectric displacement, respectively. The differential free energy dG is written as:

$$dG = -\sigma d\theta - S_{ij} dT_{ij} - D_i dE_i \tag{1.2}$$

For piezoelectrics, D depends on the stress, replacing D_i by $D_i + d_{kij} T_{kl}$, and integrating the equation (assuming constant coefficients), we obtain:

$$\widetilde{G} = -\frac{1}{2} s^E_{ijkl} T_{kl} T_{ij} - \frac{1}{2} \varepsilon^T_{ij} E_i E_j - d_{ijk} T_{kl} E_i \tag{1.3}$$

when $d\theta = 0$. The dielectric, elastic and thermal equations of state can be derived from Eq.1.3 [2, 3]. Considering a constant temperature, one can derive the isothermal piezoelectric equations as:

$$S_{ij} = -\frac{\partial \widetilde{G}}{\partial T_{ij}} = s^E_{ijkl} T_{kl} + d_{kij} E_k \tag{1.4}$$

$$D_i = -\frac{\partial \widetilde{G}}{\partial E_i} = d_{ijk} T_{jk} + \varepsilon^T_{ij} E_j \tag{1.5}$$

s_{ijk} is the elastic compliance, d_{ijk} is the piezoelectric constant and ε_{ij} is the permittivity (dielectric constant). The mechanical properties of a piezoelectric material depend on the electrical conditions. The E-field can be constant, or the D-field can be constant. There are thus 2 sets of compliance constants: the ones at constant E (s^E), and the ones at constant D (s^D). Likewise, the electrical permittivity depends on mechanical conditions. There is a set for constant stress (ε^T) and one for constant strain (ε^S). Mixed conditions are possible as well in practice. A thin film for instance is clamped to a substrate in the plane of the film (constant strain), but free to move in the thickness direction (constant stress, i.e. zero stress). The actual dielectric constant of a thin film lies between the fully clamped ε^S and the fully free ε^T.

Equations 1.4 and 1.5 are useful choices when we know or define the stress and the electric field. This is quite often the case when dealing with a free body, equipped with electrodes, to which we apply mechanical forces and electrical voltage differences. In many other situations, like for a thin film, or a wave propagation, we deal with mixed conditions depending on boundary conditions, or the direction of the wave vector. In any case, one set of equations for one choice of independent variables is sufficient to derive all other situations. For instance we can pass from the (T, E) system to the (S, E) system, i.e. to introduce S as an independent

variables. To do so, one needs to write the piezoelectric stress matrix e, the stiffness matrix c, and the permittivity matrix ε at constant strain.

$$e = d(c^E) \tag{1.6}$$

$$c = (S^E)^{-1} \tag{1.7}$$

$$\varepsilon^S = \varepsilon^T - dc^E d^t \tag{1.8}$$

Introducing these variables into equations 1.4 and 1.5 gives:

$$T_{ij} = c^E_{ijkl} S_{kl} - e_{kij} E_K \tag{1.9}$$

$$D_i = e^E_{ijk} S_{jk} + \varepsilon^T_{ij} E_j \tag{1.10}$$

where c_{ijkl} and e_{ijk} denote the stiffness and piezoelectric tensors, respectively.

If the constant parameter is the D-field, one has to transfer the constitutive equations for the constant D:

$$\begin{aligned} T &= c^E S - e(\frac{D - eS}{\varepsilon^T}) \\ &= (c^E + \frac{e^2}{\varepsilon^T})S - \frac{eD}{\varepsilon^T} \\ &= c^D S - \frac{eD}{\varepsilon^T} \end{aligned} \tag{1.11}$$

c^D is known as the piezoelectrically stiffened stiffness constant.

In a hexagonal symmetry class, like the AlN structure, d_{33}, d_{31}, and d_{15} are the non-zero piezoelectric coefficients. When the applied electric field is parallel to the polarization vector, the provoked stain is proportional to the longitudinal piezoelectric coefficient d_{33}, and the transversal piezoelectric coefficient d_{31}. In thin films, the longitudinal piezoelectric coefficient $d_{33,f}$, is smaller than the bulk value d_{33}, due to the lateral clamping of the film by the substrate.

$$d_{33,f} = \frac{e_{33}}{c^E_{33}} = d_{33} - \frac{2d_{31}s^E_{13}}{s^E_{11} + s^E_{12}} \tag{1.12}$$

The FEM assisted Double Beam Laser Interferometry (DBLI) technique was employed in this work to measure $d_{33,f}$ of thin films. This method is considered as the most accurate technique to measure the $d_{33,f}$, since substrate bending and it's thickness change are taken into account. Details of this method are described in references [4].

The transversal piezoelectric coefficient, e_{31}, is an important parameter for MEMS devices in which the performance is based on a cantilever and plate deflection.

In the thin film boundary conditions, the absolute value for this coefficient, $e_{31,f}$, is always larger than the bulk value.

$$e_{31,f} = \frac{d_{31}}{s_{11}^E + s_{12}^E} = e_{31} - \frac{c_{13}^E}{c_{33}^E} e_{33} \tag{1.13}$$

In this work, the transversal piezoelectric coefficient $e_{31,f}$ was determined with a four-point bending setup of aixACCT Systems [5, 6].

1.2.2 Piezoelectric Resonators

Practically, all acoustic wave devices, including RF filters, use a piezoelectric material to generate the acoustic wave. Different types of acoustic resonators have been developed based on the traveling nature of the acoustic wave in the piezoelectric substrate. Here we introduce surface acoustic wave (SAW), bulk acoustic wave (BAW), and Lamb Wave resonators (LWR). The resonators can be connected in different ways e.g. Ladder topologies to produce an RF filter. Figure 1.2.a shows a common ladder filters configuration [7] which employs resonators in both series and shunt branches. In each branch, all resonators have the same series resonance frequency (f_s) and the same parallel resonance frequency (f_p), which are different from f_s and f_p of the other branches' resonators. Actually, the resonance frequency of the shunt-resonators is shifted down by adding a layer as a mass loading, in comparison to the resonance frequency of series branch resonators. The center frequency of the ladder filter, as it is shown in Figure 1.2, is usually equal to the f_s of the resonators in the series branch. At the center of the passband the series resonators have the minimum impedance, and thus let the signals pass. Meanwhile, the maximum impedance of shunt resonators does not shunt the passing signal [8,9]. Figure 1.2 shows the typical frequency response of a ladder filter.

The bandwidth (BW), skirt, shape factors, out of band rejection, and in-band insertion loss are the noticeable performance parameters in a filter. The bandwidth is mainly determined by the effective coupling coefficient of the resonators. The steepness is defined by the number of resonators, which also affects to a certain extent the bandwidth as well. To minimize the insertion loss, a resonator must have a high quality factor; moreover, the shunt resonators must show the large impedance at f_p and the series resonator must show low impedance at f_s.

SAW

The RF filter market has been dominated for several years by SAW resonators. Small size, relatively simple manufacturing process which leads to low cost, and

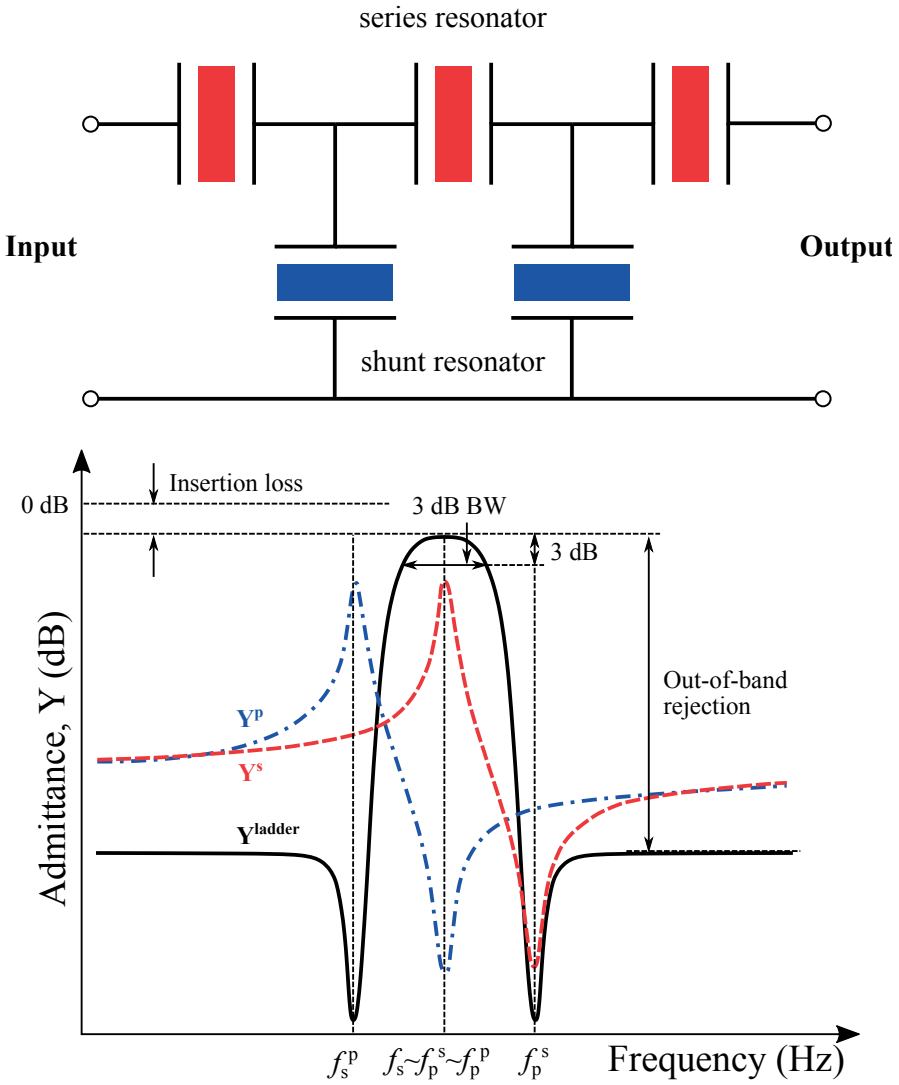

Figure 1.2: A ladder filter schematic with the series and shunt branches (top), and the typical frequency response of such filter (bottom).

excellent performance made the SAW devices the first choice for many RF and IF filter applications. In 1885, Rayleigh discovered surface acoustic waves propagation in solids [10]. The topic was extensively investigated in the 19th and 20th centuries. However, it has never been exceeded furtherer than a scientific curiosity with few applications. The revolutionary point of SAW technology was the invention of the

Interdigitated transducers (IDT) by White and Voltmer in 1965 [11], which led to the ability of direct generation and detection of elastic surface waves through the piezoelectric effect. Figure 1.3 shows schematic of a one-port SAW resonator. Metal lines of IDTs on a piezoelectric substrate generate and pick up the so-called Rayleigh wave. The lateral period of the fingers is designed to fit the acoustic wave pattern at the passband frequency. Fingers' width is usually equal to $\lambda/4$ and therefore the IDT pitch Λ as well as the grating period is half of the wavelength ($\lambda/2$). Surface acoustic waves are generated by applying RF signals to the IDTs. The generated wave propagates along the direction perpendicular to the transducer length. Energy loss is reduced by putting grating type reflectors at both ends of the IDTs to reflect the generated SAWs. $LiNbO_3$ single crystals are the dominating piezoelectric

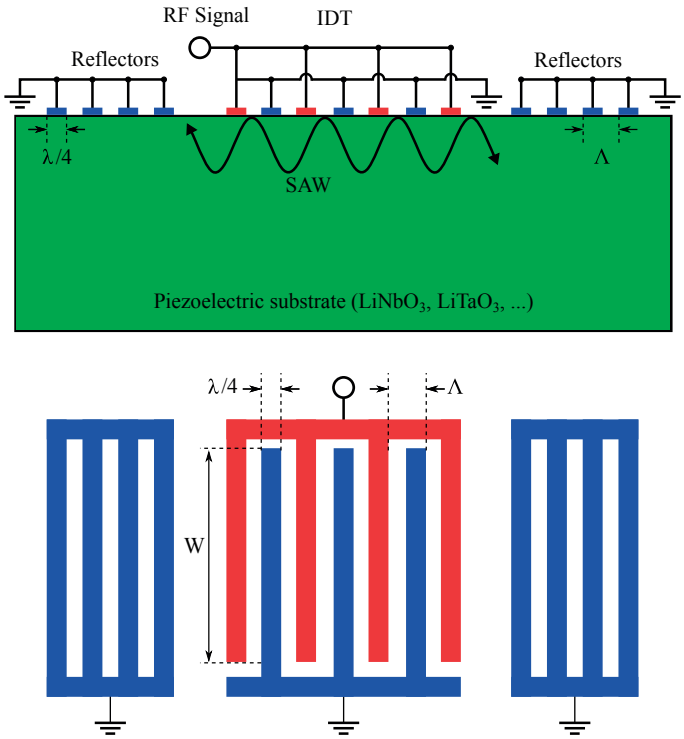

Figure 1.3: Schematic cross sectional view (top) and top view (bottom) of a one port SAW resonator.

substrate for SAW devices. However, other monocrystalline piezoelectric materials such as quartz, lithium tantalate, and other exotic materials can also be used. As it is explained, the wavelength of the propagating SAW is manipulated by IDT's

pitch. Considering the SAW phase velocities in the common substrates such as quartz, $LiNbO_3$, and $LiTaO_3$, which are below 4000 m/s, lithography resolution of 0.25μm is needed to approach operation frequency of 2GHz. This increases the production cost dramatically. Practically, for the operation frequency above 2.5 GHz, SAW devices are not available. Reducing the width of the transducers, not only increases the photolithography cost, but also reduces the power handling capability of the devices. Because reducing the finger width leads to the increase of the current density at narrow comb fingers, which causes problems like electromigration and overheating. The latter was the main barrier of using SAW devices in the antenna-duplexer of CDMA phones at 1900 MHz. Becoming vulnerable to electrostatic discharges is another consequence of tight spacing between the fingers. Low quality factor (Q) is the next drawback of SAW devices. The loss mechanism such as viscous loss, acoustic stray waves, and electrical resistance cannot be avoided without significant enlargement of the device. Therefore, the Q factor of SAW RF filters, which directly affects the steepness of the passband skirt, hardly exceeds 1000. Furthermore, relatively large temperature drift of frequency and lack of compatibility with standard microelectronic manufacturing process are the other limits of SAW technology [8, 12, 13].

BAW

In BAW resonators the acoustic wave propagates through the bulk of the material. Therefore, three modes of resonance, i.e., longitudinal wave, shear horizontal (SH) wave, and shear vertical (SV) wave define as BAW modes. In the longitudinal mode, the polarization vector is in the same direction as the applied electric field, while in shears mode they are orthogonal. Terms of *horizontal* and *vertical* in shear modes refer to the direction of the polarized plane. Among these modes, the longitudinal one, which also called the primary wave, has the highest propagation velocity and it is also the most used one.

The basic structure of a BAW resonator consists of a piezoelectric layer which is sandwiched between two metal electrodes, as in a parallel plate capacitor. The electric field is applied in the thickness direction of the piezoelectric layer, thereby longitudinal acoustic waves are generated (Figure1.4). The plate resonates when the thickness of the film is equal to odd integer multiple of half-wavelength of the acoustic wave:

$$f_N = \frac{v_l N}{2t}, \tag{1.14}$$

where v is the acoustic velocity of the shear or longitudinal wave, N is an odd integer, and t is the thickness of the piezoelectric slab.

In thin film BAW resonators (TFBAR), the piezoelectric layer as well as the

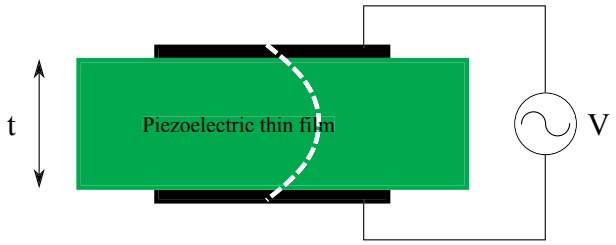

Figure 1.4: Basic structure of a BAW resonator. The dashed line represents the stress distribution of the fundamental half-wavelength thickness resonance mode.

electrodes are deposited with the vacuum techniques deposition. A substrate such as a silicon or a glass wafer provides the mechanical support for the films. Standard lithography and etching methods are usually employed to pattern the films into micrometer-range dimensions, which enables the devices for GHz-range operation frequencies.

In order to have the desired resonating mode in a TFBAR, the acoustic wave must be trapped in the acoustic cavity defined by the piezoelectric layer. There are mainly two methods to provide such trapping, which discriminate the two type of devices that, nowadays, are in mass production [14–16]: the membrane type resonators (often called FBAR) and solidly mounted resonators (SMR). The FBAR technology uses an air interface at the lower surface of the resonator to confine the acoustic wave in the resonator. This air interface could be provided by either using a sacrificial layer, released through isotropic etching [17, 18], or by etching part of the substrate underneath the resonator [19–22].

In SMRs the BAW resonator is solidly mounted on a reflector array which is called Bragg reflector [23]. The Bragg reflector, which was introduced by Newell in 1965, consists of a set of quarter-wavelength thick sections of alternating layers of high and low acoustic impedance materials, which provide efficient isolation of the acoustic wave inside the resonator cavity [24]. The acoustic wave amplitude diminishes by propagating through the reflector depth [25, 26]. However, due to the leakage of acoustic energy to the reflector, the effective coupling coefficient in SMR devices are smaller than the FBARs [27]. The number of the required alternating layers, to achieve the desired reflection, depends on the difference of the acoustic impedance between the layers. The larger difference yields a more

efficient reflection. For instance, a smaller number of the alternating layers would be required if one employs tungsten ($Z \simeq 104$ MRayl), and SiO_2 ($Z < 15$ MRayl) instead of AlN ($Z = 38.3$ MRayl) with SiO_2. It is also possible to tune the thickness of the layers from quarter wavelengths in order to reflect the shear waves as well. This modification can significantly enhance the quality factor [28]. Figure 1.5 illustrates schematics of FBARs and SMR technologies.

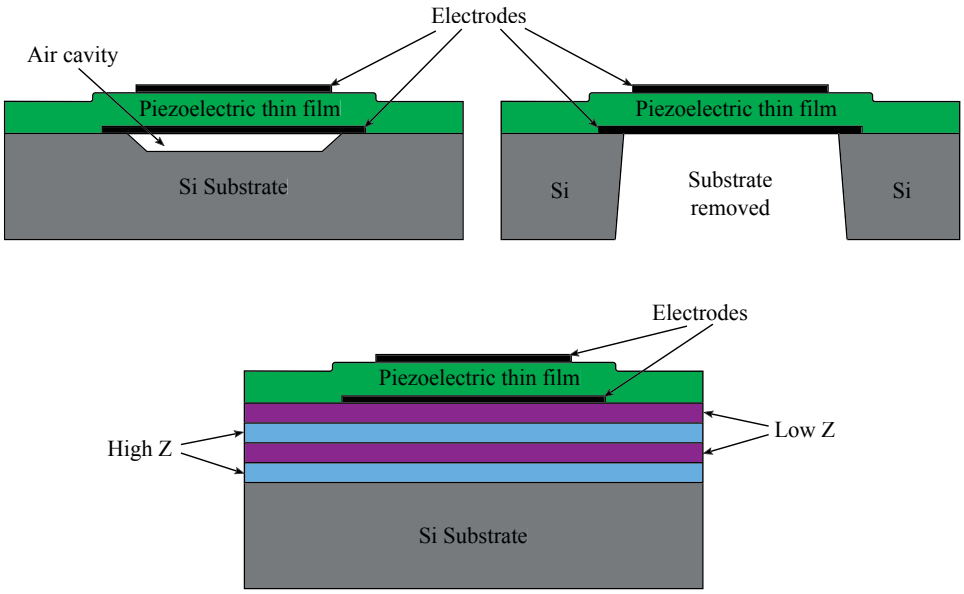

Figure 1.5: Different types of TFBARs regarding liberation from the Si substrate. Air-gap type (top left), fabricated by etching a sacrificial layer. The top-right shows the self-supported membrane resonator, liberated from the Si substrate by anisotropic Si etching (Bosch process). The bottom image shows an SMR type resonator which benefits from the Bragg reflector instead of the air interface to define the resonance cavity.

Aluminum Nitride (AlN) [29, 30] and Zinc Oxide (ZnO) [20, 30–35] were the most commonly used piezoelectric materials for the development of the BAW technology. Cadmium Sulfide (CdS) based BAW devices were also studied by some groups [36], but they have been abandoned since a while due to the low coupling coefficient. Table 2.1 shows the main mechanical and electrical properties of these materials. All these materials have the same crystallographic structure, 6mm, and are classified as a wurtzite crystal [31, 37]. Nowadays, almost all of the commercial applications of BAW employ AlN based thin films as the piezoelectric material.

Table 1.1: Mechanical and electrical properties of different piezoelectric materials used for the development of the BAW technology.

Material	$c_{33}[N/m^2]$	$\rho[Kg/m^3]$	$e_{33}[C/m^2]$	ε_r	$V_p[m/S]$	$Z_a[Kg/m^2s]$	k_t^2
AlN	395	3260	1.5	10.5	11340	3.70e7	$\sim 6.1\%$
ZnO	211	5680	1.32	10.2	6370	3.61e7	$\sim 9.1\%$
CdS	94	4820	0.44	9.5	4500	20150e7	$\sim 2.4\%$

This is mainly due to its compatibility with standard CMOS process technology, unlike the ZnO. It means that regular IC facilities can be used to fabricate an AlN BAW and there is no need for dedicated facilities. The high sound velocity, low temperature drift, and high electrical resistivity are the other parameters that help AlN dominate the market.

Recently, it was shown that partial substitution of Al by Sc could enhance the electromechanical coupling significantly [38, 39]. When the Sc content is 43 at.% the electromechanical coupling is up to five times of pure AlN. Sputtering is the most common technique for deposition of AlN and AlScN thin films. The sputtering parameters must be precisely controlled in order to achieve a high quality piezoelectric thin film. Growth and properties of AlN and AlScN thin films will be discussed in detail in Chapter 2.

Lamb Wave Resonators

In thin plates there exists yet another type of waves: the Lamb waves. Imagine SAW waves propagating on both sides of a plate. If the plate becomes thinner than a certain multiple of the wavelength, the two SAW waves start interacting, and also mix with bulk waves. The so formed modes in such thin plates are called Lamb modes, and their corresponding waves, Lamb waves [40]. Lamb wave modes are categorized into symmetric (S) and asymmetric (A) modes based on the symmetry of the particles displacements, which is usually just in X and Z directions, regarding the median plane of the plate. Figure 1.6 shows a schematic view of symmetric and asymmetric modes. Higher orders of symmetric and asymmetric modes are usually denoted as S_n and A_n, respectively. The complexity of wave shape increases with increasing n. For very thin plates ($t \ll \lambda$), the basic asymmetry mode (A_0) corresponds to a simple plate deflection mode, which is also known as the flexural mode. Figures1.7 shows the Comsol simulation of displacement filed for different

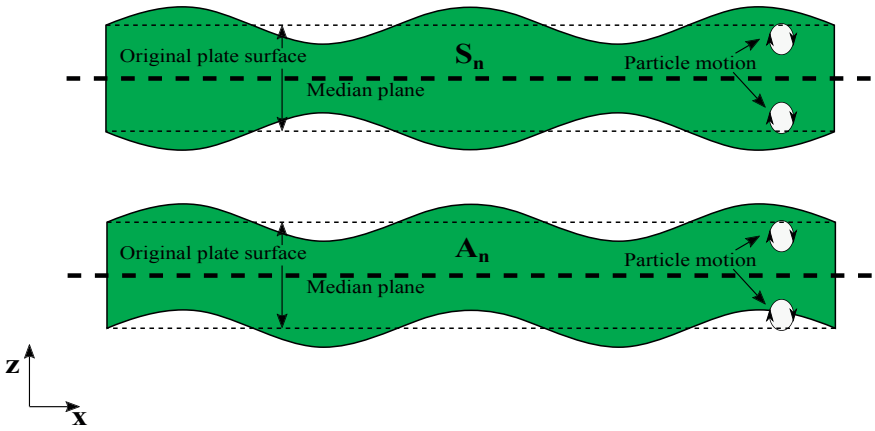

Figure 1.6: Schematic view of symmetric and asymmetric Lamb wave modes.

modes of a Lamb wave.

Employing AlN based lamb wave resonators for electro-acoustic application suggested by Piazza and Yantchev since 2002. As the lamb wave device has the advantages of both mature technologies of BAW and SAW. The frequency depends not only on the layer thickness but also on the period of the interdigitated electrodes. Therefore, LWRs simultaneously solve the low resonance frequency limit faced by the SAW resonators and the multiple frequency capability problems faced by the BAW resonators. From the acoustic point of view, the lowest order symmetric mode (S_0) in a c-textured AlN slab attracts more attention due to its high phase velocity close to 10,000 m/s. Therefore, this mode has been widely explored for different applications [41–49]. Such devices excel with a high phase velocity, a weak phase velocity dispersion, a small temperature coefficient of frequency, and a high quality factor (Q). However, only moderate electromechanical coupling factors (k^2) were achieved.

Like the SAW devices, the lamb wave modes can be generated by applying RF signals to the IDTs. The produced waves propagate in the piezoelectric thin film and are reflected by either periodic grating reflectors (like SAW) [41–44] or by the suspended free edges at both sides of the piezoelectric plate [45–51], Figure 1.8 illustrates both topologies. Some of the Lamb wave modes, especially the higher orders, could be converted to other modes while getting reflected from the suspended free edges [52]. Such conversion usually associated with noticeable loss, which mainly depends on the mode, film thickness, and wavelength. No conversion had been observed so far for the lowest order modes upon reflection, and these modes can be fully reflected [53].

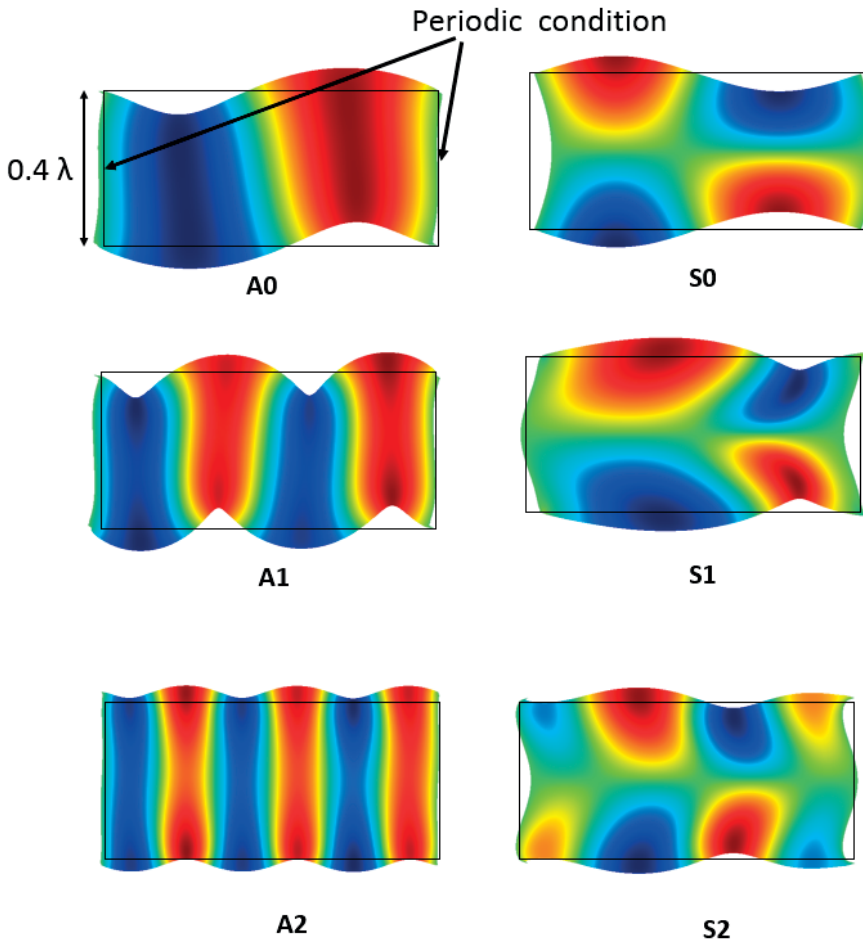

Figure 1.7: Displacement field for different Lamb wave modes from a finite element simulation.

1.3 Key Parameters of Resonators

Piezoelectric resonators are electromechanical devices which convert reciprocally electrical and mechanical energies. Two-way coupling takes place at resonance frequency between electric filed and stress in the piezoelectric material. Furthermore, in every vibration half cycle (Figure 1.9), conversion of energy from kinetic to potential form and vice-versa takes place for both electrical energy, which applied through the metallic electrodes, and the mechanical energy in the resonator body. These two conversion mechanisms determine the overall performance of a resonator. Electromechanical coupling factor, k^2, and quality factor, Q, are the parameters which are defined to evaluate the efficiency of the above-mentioned

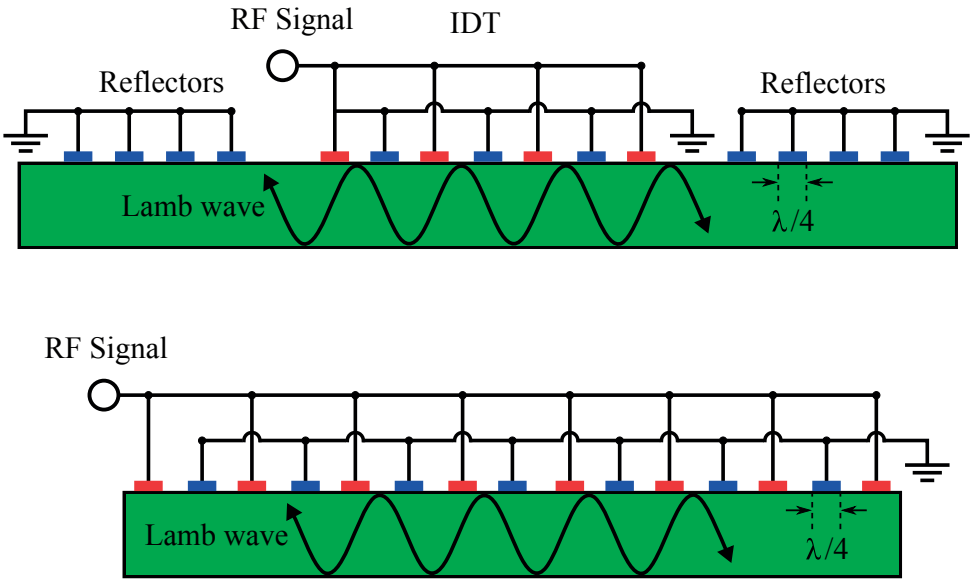

Figure 1.8: Cross-sectional schematic of two types of Lamb wave resonators regarding reflectors configuration. The top shows the periodic grating type reflectors and the bottom shows the free-edges configuration.

energy conversions in resonators.

1.3.1 Quality Factor

The quality factor, Q, is an indication of the energy loss in a resonator. During each conversion of energy from one form to another, a portion of it either is directly wasted or turned into a non-restorable form, e.g., heat. The quality factor generally defined as:

$$Q = 2\pi \frac{\text{peak energy stored}}{\text{energy dissipated per cycle}} \tag{1.15}$$

There are several sources of loss in a resonator. Therefore, all the dissipated energies must be considered in the overall quality factor calculation.

$$Q_{total} = 2\pi \frac{E_{stored}}{\Sigma_i E_{dissipated_i}/cycle} = (\Sigma_i \frac{1}{Q_i})^{-1} \tag{1.16}$$

Figure 1.9: Schematic diagram of energy flow in a piezoelectric resonator [54].

Since resonators are usually characterized by frequency measurements, it is more convenient to introduce a frequency based formula for Q. Equation 1.17 is such this kind of formula.

$$Q = \frac{f_0}{BW_{3dB}} \tag{1.17}$$

where f_0 is the resonance frequency and BW is the bandwidth of the peak. Using slope of the electronic impedance phase ϕ at resonance or antiresonance frequency is the other method to determine a deceive quality factor. m is the slope of the phase at resonance/antiresonance

$$m = \frac{\partial \tan\phi}{\partial \omega} \tag{1.18}$$

Quality factor $Q_{r,a}$ can be expressed in terms of impedance phase slope at $\omega_{r,a}$: $\phi \longrightarrow 0$

$$Q_{r,a} = \frac{f_{r,a}}{2} \frac{\partial \phi}{\partial f}\bigg|_{f_{r,a}} \tag{1.19}$$

Sources of Loss

Propagation of an acoustic wave in a piezoelectric medium is associated with different sources of loss. These mechanisms can be categorized into two groups: intrinsic and extrinsic. Intrinsic loss mechanisms are fundamentally linked to material properties. Dielectric loss, piezoelectric loss, and elastic loss are the three well-known mechanisms of this category. Dielectric loss is the loss associated with the polarization process of the material. Therefore, various components of polarization mechanisms i.e. domain, dipolar, ionic and electronic contribute to this loss. That is why this loss is frequency dependent. The piezoelectric loss comes from the conversion of the electric energy to the mechanical energy. In AlN based materials, the contribution of these two mechanisms is minimal due to the absence of the domains and polarizability. The elastic loss is the most important loss mechanism for AlN. When an acoustic wave faces grain boundaries, domains or other defects, acoustic energy dissipate to heat or diffusion. One can consider

these losses source in wave propagation equations by writing them in complex form. In the elastic loss case, the elastic constant can be written as:

$$c_{ij}^{E} \rightarrow c_{ij}^{'E} + ic_{ij}^{''E} \tag{1.20}$$

The imaginary part is dependent on the frequency and on the viscosity constants η, which depends on the wave direction and polarization.

$$c_{ij}^{''E} = \omega\eta_{ij}^{E} = \omega c_{ij}^{E}\tau_{ij} \tag{1.21}$$

τ is the time constant. Then, the acoustic quality factor defined as:

$$Q_A = \frac{1}{\omega\tau} \tag{1.22}$$

In addition to the intrinsic loss sources, there are several other loss mechanisms mainly originating from the practical aspect of design and fabrication, and not fundamentally related to materials properties. These mechanisms are known as the extrinsic loss. Anchor loss and ohmic loss are two well-known examples of this category. Anchor loss, which strongly depends on the dimensions, position, and shape of the anchors, represents the acoustic energy loss from a resonator body to the farm holding the resonator (Figure 1.10). Several analytical models conducted to investigate anchor loss in a variety of designs [55, 56]. As an overall conclusion, it can be said that putting the anchor at the positions which has virtually zero displacements on resonance, reduces the anchor loss significantly. Center-support bulk mode disc resonators [57] and notch attached supports in ring shape resonators [58] are practical examples of this technique.

The ohmic loss is the next extrinsic loss mechanism. This source of loss comes from the ohmic resistivity of the resonator electrodes and their associated paths. Therefore, one can mitigate its effect by choosing the proper electrodes' material (low resistance) and reducing the elector thickness and the path's length.

1.3.2 Coupling Factor

The electromechanical coupling is the next parameter (after Quality factor) which assess the performance of a resonator. This parameter describes the efficiency of the energy conversion process between mechanical and electrical form in a resonator. Various approaches are introduced to define the coupling factor of a piezoelectric material, analytical point of view, most of them result in almost the same expression [59]. One needs to distinguish the electromechanical coupling factor of a resonator, from the coupling factor of a piezoelectric material. The later is a material property, and despite the first, it is not dependent on resonator design and fabrication process.

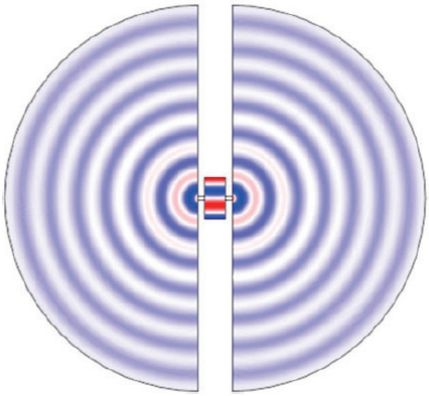

Figure 1.10: 2D model of a lateral-extensional resonator (3^{rd} harmonic) held on the substrate by anchors. The color code represents the strain on the resonator and the substrate, but the color intensity is not a true representation of the strain intensity [54].

Piezoelectric Coupling Factor

Piezoelectric coupling factor is a measure of piezoelectric material ability in the mutual conversion of electrical energy into mechanical energy. In an ideal case with no loss, one can define the piezoelectric coupling factor as follows:

$$k^2 = \frac{W_M}{W_M + W_E} \tag{1.23}$$

W_M is the mechanical work delivered by a mechanically free piezoelectric material, which is connected to an electrical source and pre-loaded with potential energy equal to: $W_M + W_E$ [60]. This ratio is a function of material properties as follows:

$$k^2 = \frac{e^2}{c^E \epsilon^T} \tag{1.24}$$

where e is the piezoelectric coefficient in the direction of electric field and mechanical stress, c^E is the stiffness at zero electric field, and ϵ^T is the dielectric constant at the direction of the electric field at zero stress. For instance, in the thickness extensional mode k_t^2 reads

$$k_t^2 = \frac{e_{33}^2}{c_{33}^D \varepsilon_0 \varepsilon_{33}^S} \tag{1.25}$$

In a piezoelectric resonator, the energy conversion efficiency can never exceed the coupling factor of the piezoelectric material. Thus, k^2 is the upper boundary of efficiency in a piezoelectric resonator. Table 1.2 presents the coupling factor for most commonly used piezoelectric materials [61–63].

Table 1.2: Piezoelectric coupling factor for common piezoelectric materials.

Material	Quartz	PZT	ZnO	AlN
$k_t^2\%$	0.86	23	8.5	6.5

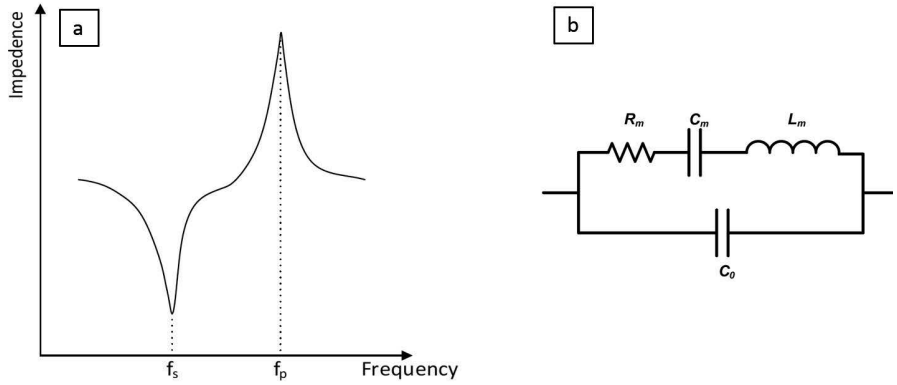

Figure 1.11: (a.) Schematic typical impedance characteristic for a one-port piezoelectric resonator. (b.) basic BVD model of a resonator. [54]

Effective Electromechanical Coupling Factor

Effective electromechanical coupling factor k_{eff}^2 describes the energy conversion efficiency on a piezoelectric resonator. It can be defined as:

$$k_{eff}^2 = \frac{f_p^2 - f_s^2}{f_p^2} \tag{1.26}$$

where f_p is the parallel resonance frequency (impedance max) and f_s is the series resonance frequency (impedance min), as depicted schematically at Figure 1.11.a. The piezoelectric materials properties like k^2 as well as the design and fabrication process can influence the k_{eff}^2, significantly.

The components of the equivalent electrical circuit (e.g BVD model [64]) of the resonator is also used for defining the resonator coupling factor.

$$k_{eff}^2 = \frac{C_m}{C_0} \tag{1.27}$$

where C_m is the motional capacitance and C_0 is the static capacitance of the resonator.

1.3.3 Figure of Merit

Figure of Merit (FoM) represents the overall performance of a piezoelectric resonator considering both quality factor and effective coupling factor. It is defined as:

$$FoM = \frac{k_{eff}^2.Q}{1 - k_{eff}^2} \tag{1.28}$$

for the small value of k_{eff}^2 it would be re-write as:

$$FoM = k_{eff}^2.Q \tag{1.29}$$

the higher value of FoM means better signal to noise ratio, which is the figure of merit for all the electrical system.

1.4 Thesis Objectives and Outline

- The aim of this project is the assessment of the potential of AlScN based Lamb wave resonators for RF filter application. To do so, we design and fabricate Lamb wave resonators by 15% and 30% Sc AlScN thin films. We investigate two types of devices: Freestanding (membrane type), and for the first time, solidly mounted (SM) Lamb wave resonators . The latter one, is studied on two types of Bragg reflectors including W/SiO_2 and AlN/SiO_2 as the alternating layers. Design, fabrication, and characterization of these resonators are presented in Chapter 5.

- Reliable material parameters are essential to design and predict properties of ultrasonic devices, particularly when they are based on the more complex mode shapes. e.g., Lamb wave resonators. In the general case, a full set of elastic, dielectric, and electromechanical coefficients is required. The parameters are preferentially extracted either from SAW devices [65] or from simple mode resonators, which depend on a very reduced set of coefficients [66]. Excitation of the pure mode resonances is one of the most precise techniques which can be employed to determine material constants for the bulk piezoelectric crystals [67]. In this work, we design and fabricate shape resonators with proper geometry in order to excite pure modes in piezoelectric thin film and later on extract the materials parameters by resonance analysis of the pure modes. Thickness extensional mode, length-extensional mode, radius extensional mode, and thickness shear mode are the excited shape modes resonances. This procedure implemented for 15 %Sc AlScN thin film. Results are presented in Chapter 4.

- Satisfying the goals mentioned above, we needed to fabricate the various types of devices including Lamb wave resonators (different types), length-extensional mode resonator, thickness extensional mode resonator, radius extensional mode resonator and lateral shear mode resonator. These devices have different geometries, critical dimensions, operation frequencies and etc. Therefore, we needed to employ different fabrication approaches based on the device requirements and fabrication limits. A vast range of fabrication techniques were employed to fabricate a functional set of devices. Chapter 3 describes the microfabrication process, the challenges we faced during the process and the solutions we developed for them.

- A c-textured piezoelectrically active AlScN thin film is the key element of all the devices we aimed to fabricate and characterize in this thesis. Obtaining such a film is not always straightforward. Bottom electrode has a significant role in achieving the desired film. Lack of the proper bottom electrode or its patterning has severe consequences on the film quality. In Chapter 2, we describe the sputtering process employed in this work. Then we show how to achieve a c-textured piezoelectric AlScN film on a non-metallic substrate (no bottom electrode), which is of interest for specific modes e.g. lateral shear mode. Then we discussed the ab-normal grains phenomenon, which is a hot topic and challenge nowadays in the AlScN community and gets more severe by patterning the bottom electrode and also increasing the Sc content.

- Chapter 1 is the introduction. It is dedicated to give an overview of backgrounds and motivations of this work. Firstly, we discussed the importance of high performance RF filters in the today enormous and competitive market of communication systems. Resonators as the critical component of RF filters were discussed in continue and TFBAR and SAW resonators, as the two standard types of the employed resonator in RF filters, were introduced. Then we introduced the Lamb wave resonator, which evaluating of it's potential for RF filter application is one of the ultimate goals of this project. In the end, we introduced the key parameters of a resonator which are essential to assess the performance of a resonator from any kind.

Chapter 2

From AlN to $Al_{1-x}Sc_xN$

2.1 AlN

AlN emerged as the most suitable material for vast range of the RF MEMS devices working based on piezoelectric thin film technology [23, 61, 68]. Very reliable and reproducible deposition process, CMOS compatibility despite PZT and ZnO, very high thermal conductivity, relatively low TCF, along with excellent acoustic characteristics such as high acoustic velocity and low acoustic loss, make AlN an excellent compromise between performance and mass production ability. Furthermore, the large band gap of 6.2 ev accompanied by a large intrinsic resistance ($> 10^{13}\Omega.cm$), a low dielectric constant, a low loss tangent and high thermal conductivity of $3.19W.cm^{-1}.K^{-1}$ (at RT) make the AlN an ideal candidate for high power applications. Due to this combination of properties RF MEMS based on AlN technology exhibit high quality factor at high frequency, limited drift with temperature and capability of working in harsh environments. Table 2.1 represents the physical properties of AlN as well as the ZnO and GaN as the most common piezoelectric thin films for high frequency acoustic applications. From the crystallographic point of view, AlN grows in the wurtzite structure. Therefore, it belongs to the hexagonal crystals family with point group 6mm. Figure 2.1 illustrates the hexagonal wurtzite structure of the AlN with a lattice constant of $a = 3.11\mathring{A}$ and $c = 4.98\mathring{A}$.

The wurtzite AlN is a piezoelectric material with a spontaneous polarization along the c-axis of the unit cell. Therefore, randomly oriented polycrystalline AlN does not show the piezoelectric effect because of zero net polarization. Non-ferroelectric nature of AlN does not allow reorientation of the polarization vector. Therefore, one needs to grow the AlN in single crystal or c-textured structure in order to have a piezoelectric AlN thin film.

Table 2.1: Physical properties of AlN, ZnO and GaN [25, 69–73].

	AlN	ZnO	GaN
Density [Kg/m^3]	3260	5680	6150
Longitudinal acoustic wave velocity [m/s]	~ 11300	~ 6350	~ 8050
Shear acoustic wave velocity [m/s]	~6000	~ 2720	~4130
Lattice constant, a [$\AA$]	3.112	3.249	3.1890
Lattice constant, c [$\AA$]	4.982	5.207	5.186
Thermal expansion at 300 K, α_a [$10^{-6}/°C$]	5.27	4.75	5.59
Thermal expansion at 300 K, α_c [$10^{-6}/°C$]	4.15	2.92	3.17
Piezoelectric coefficient, e_{33} [C/m^2]	1.55	1.32	0.65
Piezoelectric coefficient, e_{31} [C/m^2]	-0.58	-0.57	-0.33
Piezoelectric coefficient, e_{15} [C/m^2]	-0.48	-0.48	-0.33
Electromechanical coupling coefficient, k^2,[%]	~6.5	~8.5	~ 1.2
Thermal conductivity [W/mK]	280	60	130
TCF [$ppm/°C$]	-25	-60	-

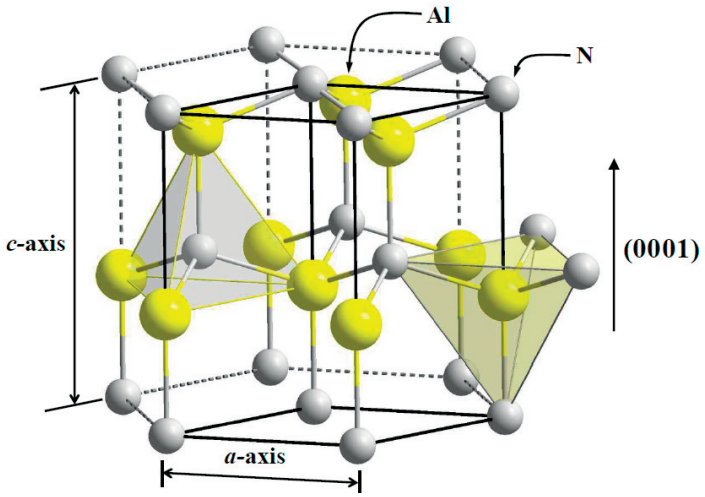

Figure 2.1: Hexagonal wurtzite crystal structure of AlN.

The hexagonal symmetry of AlN crystal (6mm) reduce the number of independent elements and non-zero elements of the matter tensors. Conventionally the axis 3 (z) consider as the polar axis. Of special interest are dielectric constants (ε), piezoelectric coefficients (d) and compliance tensors (s) as follow [74, 75]:

$$\varepsilon = \begin{pmatrix} \varepsilon_{11} & 0 & 0 \\ 0 & \varepsilon_{11} & 0 \\ 0 & 0 & \varepsilon_{33} \end{pmatrix} \tag{2.1a}$$

$$d = \begin{pmatrix} 0 & 0 & 0 & 0 & d_{15} & 0 \\ 0 & 0 & 0 & d_{15} & 0 & 0 \\ d_{13} & d_{13} & d_{33} & 0 & 0 & 0 \end{pmatrix} \tag{2.1b}$$

$$s = \begin{pmatrix} s_{11} & s_{12} & s_{13} & 0 & 0 & 0 \\ s_{12} & s_{11} & s_{13} & 0 & 0 & 0 \\ s_{13} & s_{13} & s_{33} & 0 & 0 & 0 \\ 0 & 0 & 0 & s_{44} & 0 & 0 \\ 0 & 0 & 0 & 0 & s_{44} & 0 \\ 0 & 0 & 0 & 0 & 0 & s_{66} \end{pmatrix} \tag{2.1c}$$

In hexagonal symmetry structure, the s_{66} is not independent and is equal to $2(s_{11} - s_{12})$. In some measurements it is more convenient to use the elastic stiffness matrix c and the piezoelectric e coefficients; these matrices are presented below for the hexagonal symmetry classes [76] .

$$e = \begin{pmatrix} 0 & 0 & 0 & 0 & e_{15} & 0 \\ 0 & 0 & 0 & e_{15} & 0 & 0 \\ e_{13} & e_{13} & e_{33} & 0 & 0 & 0 \end{pmatrix} \tag{2.2a}$$

$$c = \begin{pmatrix} c_{11} & c_{12} & c_{13} & 0 & 0 & 0 \\ c_{12} & c_{11} & c_{13} & 0 & 0 & 0 \\ c_{13} & c_{13} & c_{33} & 0 & 0 & 0 \\ 0 & 0 & 0 & c_{44} & 0 & 0 \\ 0 & 0 & 0 & 0 & c_{44} & 0 \\ 0 & 0 & 0 & 0 & 0 & c_{66} \end{pmatrix} \tag{2.2b}$$

The c_{66} is not independent for 6mm and ∞m symmetry classes and is given by $^1/_2(c_{11} - c_{12})$. The e coefficients are obtained from equation 2.3 [75]:

$$e_{31} = d_{31}(c_{11}^E + c_{12}^E) + d_{33}c_{13}^E \tag{2.3a}$$

$$e_{33} = 2d_{31}c_{13}^E + d_{33}c_{33}^E \tag{2.3b}$$

$$e_{15} = d_{15}c_{44}^E \tag{2.3c}$$

2.2 AlN Thin Film growth

As mentioned in the previous section, AlN has hexagonal point group symmetry which leads to isotropic properties in the plane up to fourth rank tensor. Therefore, a c-textured dense polycrystalline thin film theoretically could demonstrate identical properties as a single crystal. Thus, deposition techniques of AlN are of particular interest in all applications of the AlN thin film. AlN thin films can be produced by various methods including thermal evaporation [77,78], chemical vapor deposition [79], Molecular Beam Epitaxy, MBE [80,81], Pulsed Laser Deposition, PLD [82], RF diode and RF sputtering [82–84], DC Sputtering [85], pulsed DC magnetron sputtering [86], and dual ion beam sputtering. Among all these methods the magnetron sputtering from a pure Al target in a nitrogen (N_2)-noble gas (usually argon) mixture, is the dominating method for mass production. Because it is the only technique delivering thin films with high quality microstructure at relatively low temperatures, which is essential for MEMS, with a reasonable growth rate. Moreover, it is relatively simple and inexpensive in comparison to the others methods [4], and despite the CVD techniques, the film stress can be adjusted. AlN is a semiconductor with a relatively large bandgap of 6.2 eV. Therefore, in the sputtering chamber the electrical power must be supplied in radio frequency (RF) or pulsed DC forms in order to avoid sparks on target, anode, and shields [4,87]. Highly c-oriented piezoelectric films can be obtained by this method at 300°C [77].

The structure and morphology of AlN films deposited by reactive magnetron sputtering is a function of all process parameters such as the total pressure of the gas mixture, the nitrogen content, the substrate bias voltage (RF bias), the cathode power, and the growth temperature [84,87–89]. The AlN film morphology and microstructure can be well-described by Thornton's growth zone model for sputter depositions [90]. This diagram shows the film morphology as a function of substrate temperature and sputter gas pressure. The low process pressure leads to high ion bombardment and going towards high pressure results in shadowing effect. The best quality of the film is obtained at zone T which characterized by surface diffusion beyond thermal equilibrium mainly due to the ion bombardment (and partially due to thermal activation). As it is depicted in Figure 2.2, Zone T is located at the low-pressure zone between the low-temperature zone 1 (at which no diffusion takes place) and intermediate temperature zone 2 (at which grain boundary and surface diffusions are enabled by thermal activation) [90,91]. T-zone microstructure is obtained in the presence of plasma impact and is characterized by an intensive surface diffusion forced by ion bombardment, and the absence of grain boundary and bulk diffusions. A certain level of ion bombardment is required to obtain well (0001) or $(000\overline{1})$-textured AlN thin film with a uniform polar orientation. The latter is reflected in the size of the piezoelectric response.

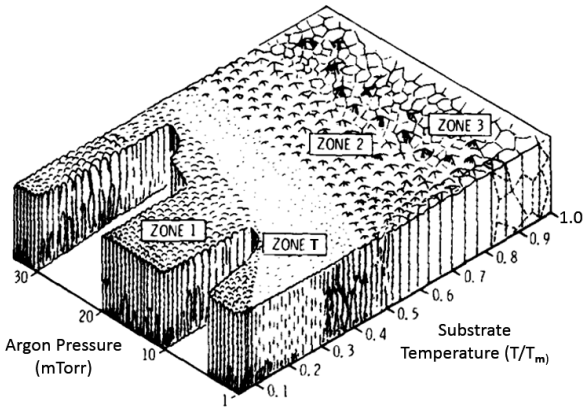

Figure 2.2: Schematic representation of the substrate temperature and argon pressure effects on the microstructure of films deposited by a magnetron sputtering source [91].

Zone T conditions are well-satisfied in AlN case by $T/T_M \approx 0.25$ and sputter gas pressure smaller than 1 Pa, the result is a dense and fibrous microstructure with a smooth surface [61].

The crystalline substrate is not necessary for the epitaxial growth of AlN and it can grow epitaxial on the amorphous substrates like silicon glass, as well. Despite the 11% lattice mismatch of AlN and Pt, AlN (0001) growth well on the polycrystalline Pt (111) thin films based on the local epitaxy [87,92–95]. AlN (0001) can be grown on polycrystalline diamond, (110) textured Mo, and W substrates as well [95,96].

Properties of AlN thin films grown on Pt electrodes studied by Loebl et al. [97]. They investigated the effect of texture quality of AlN thin film on electromechanical coupling factor, they reported k_t^2 of 6.3%. The effect of film thickness on the piezoelectric response in the AlN thin film was studied by Martin et al. [98]. They reported a direct correlation between piezoelectric response and film thickness up to $2\mu m$. A $d_{33,f}$ of 5.2 pm/V for a $2\mu m$ thick film was reported.

Internal stress is the other relevant parameter which influences the piezoelectric properties of a thin film. This parameter is also very much dependent on process conditions. Dubois and Muralt reported a steep internal stress transition from tensile to compressive by decreasing the pressure [87]. Adatom mobility and surface diffusion along with the smoothness of the substrate are parameters which are playing a role in this context. The high diffusion rate generally favors the minimum surface-energy plane, which is (0002) plane in the case of wurtzite AlN [99]. Surface diffusion is governed by substrate temperature and ion bombardment. The high temperature of the substrate leads to high mobility of ad-atoms which directly

influence the crystallization and orientation of the growing film [4, 87].

The ion bombardment is controlled by the deposition pressure and bias applied to the substrate. Decreasing the pressure reduces the number of the collisions between ions. Therefore, ions gain more kinetic energy in the plasma which consequently increases the kinetic energy of ad-atoms on the growing film surface. Ion bombardment also results in a more dense film and changes the built-in stress from tensile to compressive by the peening effect [4, 87].

2.3 AlScN

The electromechanical coupling factor , k_t^2, of the fundamental thickness mode resonance determines the filter bandwidth and is thus one of the key parameters of a BAW resonators. In a perfect resonator, this value is a characteristic property of the piezoelectric thin film material. As already mentioned , AlN (001) with a maximal k_t^2 of 6.8% is the only well-established piezoelectric material for TFBARs. The resulting bandwidth of roughly 3% is sufficient for today mobile communication standards [4, 100, 101]. But mobile communication systems continue to demand higher data rates, requiring wider bands, and thus materials with larger coupling coefficients. Actually, the low coupling factor could be called as the major limit of AlN. It would be of great interest to increase the coupling factor of AlN thin films while the other properties do not change dramatically.

Partial substitution of Al atoms looks a promising way to enhance piezoelectric coefficients in AlN thin films. The effect of the Cr doping on the microstructure and piezoelectric properties of AlN thin film was investigated by J. Luo et al. in 2009 [102]. They reported that a moderate Cr doping up to 6% enhanced the (0002) texture of AlN by the compensation of the lattice mismatch of AlN and substrate, and increases the piezoelectric response from 4 to 7 pm/V by transferring the tensile residual stress to a compressive one (see Figure 2.3).

The effect of the Er doping on the piezoelectric response of AlN films was studied by Kabulski et al. [103]. They reported that adding 1% Er improves the piezoelectric response of the film when the thickness is less than 400 nm. Increasing the concentration of Er to 3% improves the piezoelectric response independent of the film thickness.

H. Liu et al. did the same study for Ta, in 2013 [104]. They claimed that Ta content of 5.1% improved the piezoelectric response by 100%. Expansion of unit cell volume leads to an enhancement of nitrogen displacement in an electric field, which consequently results in larger piezoelectric responses. Figure 2.3.b shows the piezoelectric coefficient d_{33} as a function of the tantalum content.

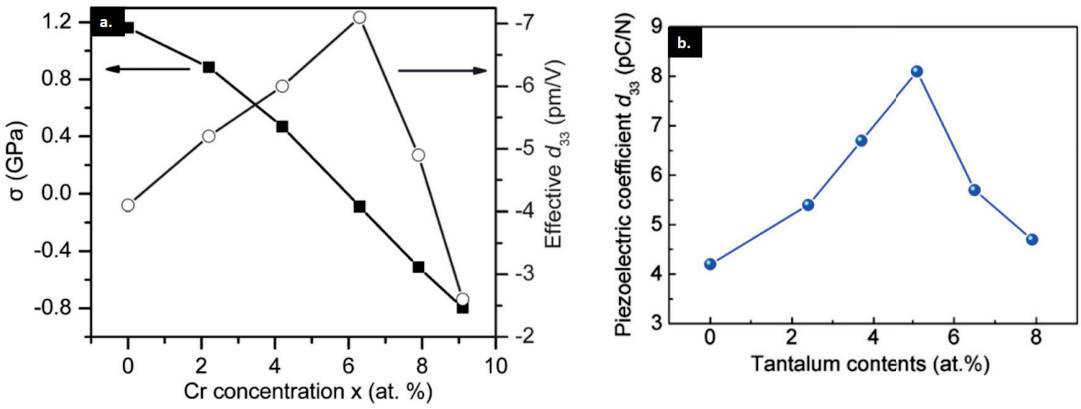

Figure 2.3: Residual stress and piezoelectric response of $Al_{1-x}Cr_xN$ films (x = 0, 2.2, 4.2, 6.3, 7.9 and 9.1 @ %) [102].

The most impressive enhancement of the piezoelectric response for AlN based thin films has been reported by Akiyama et al. [39]. They reported up to 4 times larger piezoelectric response in the sputter deposited $Al_{1-x}Sc_xN$, $0 < x < 0.56$, thin films on Si substrate, in comparison to pure the AlN thin film. They also studied the influence of the growth temperature effect on the piezoelectric response and concluded that films grown at $400°C$ had better quality than films prepared at $580°C$ where grain growth was less ordered [105]. Figure 2.4 depicted the dependency of the piezoelectric response to Sc concentration at two different growth temperature. One must notice that the reported response corresponds rather to d_{33} than to $d_{33,f}$, as the piezotest measurement tool stretches the film in the plane when pressing film and substrate together.

Such an effect was predicted earlier for the (Ga,Sc)N system based on first-principles calculations [106, 107]. The prediction comes from the fact that the piezoelectricity usually peaks at a para-to-ferroelectric phase transition and at a morphotropic phase boundary of a solid solution system. Same physics takes place in this case; the transition occurs between piezoelectric wurtzite structure on the Ga rich side and non-piezoelectric rocksalt structure on the Sc rich side. In 2010, F. Tasnadi et al. explained the origin of the abnormal increase in piezoelectric response in $Al_{1-x}Sc_xN$ in the frame of density functional theory [108]. There is a competition between Al and Sc atoms about coordination of the nitrogen, since Al^{+3} prefers 4-fold (tetrahedral), and Sc^{+3} prefers 6-fold (octahedral)coordination. Therefore, Sc in AlN tries to find more space by stretching out the nitrogen tetrahedral. It is shown that the lattice constant a is increased practically, while the lattice constant c is almost untouched (see Figure 2.5) [61, 109, 110], which lead to lower c/a ratio and elastically softening of the wurtzite structure. Therefore, ions become less

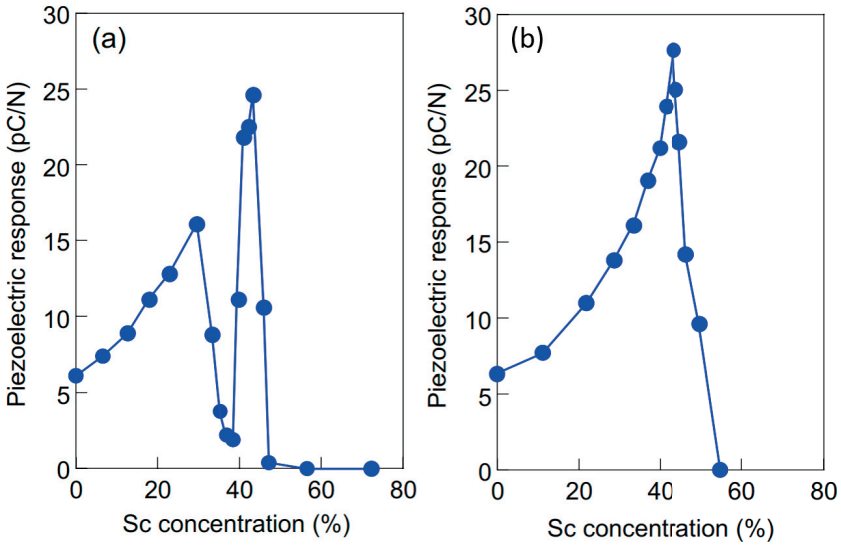

Figure 2.4: Piezoelectric response of $Al_{1-x}Sc_xN$ films deposited by reactive RF-dual magnetron sputtering on Si(001) substrate as a function of Sc content at (a.) $580°C$, (b.) $400°C$ [105].

tightly bound, (shallower potential well) meaning that the piezoelectric responses as well as the dielectric constant increase while the stiffness decrease. Increasing the Sc content make the potential well shallower which leads to larger ion displacement in a certain electric field. This means larger piezoelectric response and dielectric constant. This trend is valid as far as the wurtzite phase is kept.

Matloub et al. studied the piezoelectric properties and coupling coefficient, k_t^2, of $Al_{0.88}Sc_{0.12}N$ TFBAR test structures. They reported over 40% relative increase for $d_{33,f}$ value [111]. They also investigated the transverse coefficient $e_{31,f}$, of $Al_{1-x}Sc_xN$ as a function of composition. It increased up to 50% from $x = 0$ to $x = 0.17$ [109]. In the same work it was also found that the dielectric constant does not increase as much as $e_{31,f}$, which is an important result for energy harvesting applications. Moreira [112] and Fichtner et al. also measured the $d_{33,f}$ value experimentally for different Sc concentration than Matloub et al. Same trend of enhancement has been reported by Moreira, while Fitchner values needed adjustment to meet the reference-AlN values ($4pC/N$). Beside the experimental measurements, first principles density function theories (DFT) calculations also employed by Caro et al. [113] and Tasnadi et al. [108] to determine piezoelectric properties of $Al_{1-x}Sc_xN$ thin film. DFT reported values for piezoelectric coefficients are usually larger than the experimental ones. The differences could be originated from calculated stiffness constants. For instance, too large s_{13} would result in

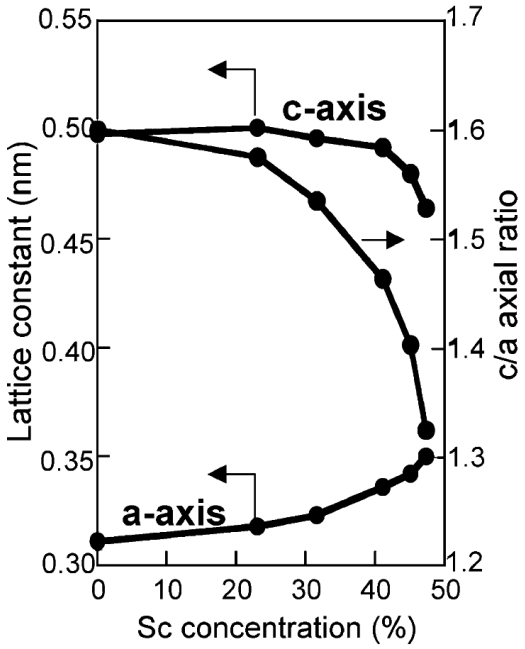

Figure 2.5: $Al_{1-x}Sc_xN$ lattice constants as a function of Sc content in wurtzite structure [39].

smaller $d_{33,f}$ in DFT calculations. Figure 2.6 shows $d_{33,f}$ and $e_{31,f}$ for different Sc concentration reported by different groups.

2.4 AlScN Thin Film Growth

Initial attempts for AlScN deposition were based on RF co-sputtering from Al and Sc targets mounted on a two magnetron source. Similar to the AlN deposition, the mixture of nitrogen and argon employed as the sputtering gas [38,39]. Later on, the pulsed DC power applied on magnetron instead of the RF power [112]. From the industrial point of view, sputtering from single source alloy target is preferred due to the higher deposition rate. Matloub et al. produced the identical microstructure, film morphology, and growth mode as with pure AlN up to 17% of Sc, by pulsed DC magnetron sputtering from an alloy target [4].

In this work, polycrystalline $Al_{1-x}Sc_xN$ films were deposited by a pulsed DC reactive magnetron sputtering chamber mounted into a cluster tool (Spider machine from Pfeiffer). The Spider consist of four sputtering chambers. Each chamber is allocated to an individual target. Wafers are loaded in a cassette and the load lock, from where the transfer module distributes the wafers between the chambers. The

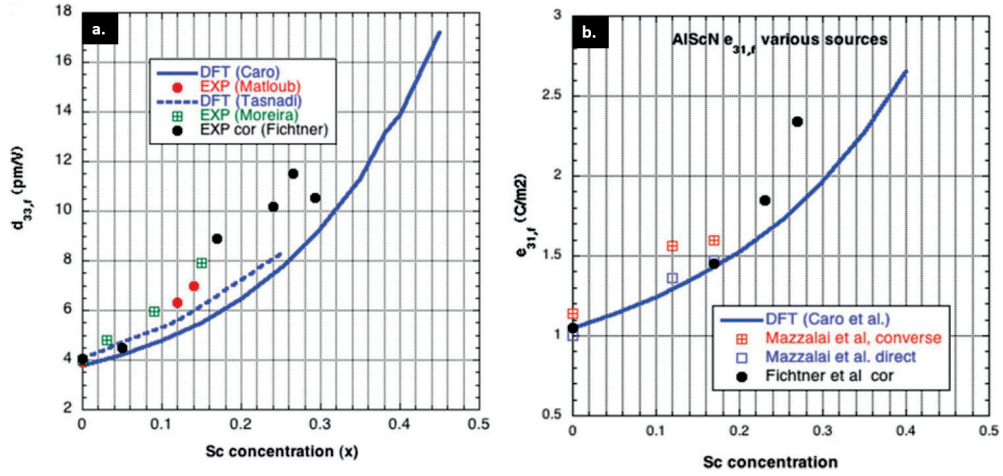

Figure 2.6: (a). $d_{33,f}$ in $Al_{1-x}Sc_xN$ thin films. Caro DTF curve is from Ref. [113]. Tasnadi DFT curve is from Ref. [108]. Matloub et al. experimental values were achieved by FEM-assisted DBL method. Moreira values obtained through TFBAR characterization [112]. The Fichtner et al. values obtained by DBLI and adjusted to meet the reference value of pure AlN sample, 4 pC/N. (b). $e_{31,f}$. The experimental $e_{31,f}$ values are from Mazzali et al. [114]. Fichtner values were adjusted for getting 1.05 C/m^2 for pure AlN [39].

whole system is always kept under vacuum. Figure 2.7 shows a top view of Spider sputtering system.

The target is a 200 mm diameter, 6 mm thick plate alloy target which was prepared by powder metallurgy technique with the nominal composition of $Al_{0.83}Sc_{0.17}$ with purity of 99.99%. Prior to deposition, the system was pumped down to a base pressure smaller than 1×10^{-7} mbar. A mixture of 50 sccm nitrogen and 35 sccm Ar, to enhance the bombardment, was employed as the sputtering gas. A Pinnacle pulsed DC generator powers the magnetron. The pulse duration is 5μs which is applied by the frequency of 20 kHz on the target. This avoids the formation of arcs which leads to particle formation and causing defects in the deposited thin film. This phenomenon well described in references [86] and [115]. Figure 2.8 shows typical voltage on the substrate during a pulsed DC deposition of AlN [78]. Alternating bombarding of the substrate by ions and electrons is clearly seen on the substrate bias. The Applied DC pulsed power adjust at 1500 W which approximately yields $1nm/s$ deposition rate. The substrate is around 10cm below the target on the chuck and was subjected to RF power of 4 W. The Spider did not utilize a shutter during target cleaning step. Instead a dummy wafer was coated before each batch of depositions for thermalizing the chamber to the process temperature (350°C) and for cleaning the target. The sputtering parameters are

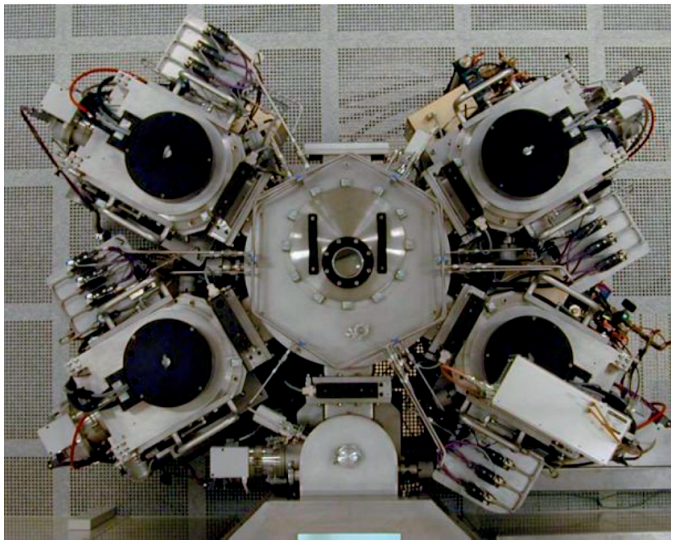

Figure 2.7: Top view of the Spider sputtering tool consisting, four sputtering chambers, load lock, and transfer Module. From cmi.epfl.ch.

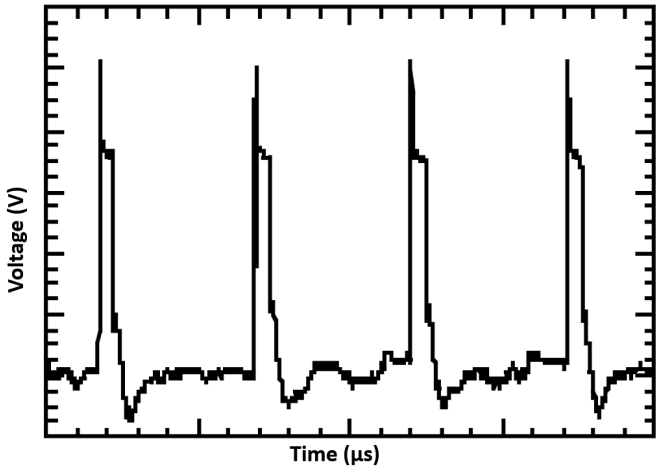

Figure 2.8: Substrate voltage variation during a pulsed DC magnetron sputtering of AlN thin film [78]

presented in Table 2.2.These parameters are identical as what used by R.Matloub et al. [4, 109] in the same sputtering cluster.

Table 2.2: Sputter process conditions for AlScN thin film deposition

Target (200 *mm* dia)	$Al_{1-x}Sc_x$
Ar gas flow	35 *sccm*
N_2 gas flow	50 *sccm*
Sputter pressure	4-7$\times 10^{-3}$ mbar
Growth temperature	350 °C
DC power	1500 *W*
Substrate RF Bias	4-6 *W*
Substrate DC Bias	80-90 *V*
Deposition Pressure	0.006-0.008 *mbar*
Deposition rate	0.8-1 nm/s

We used a Pt (111) as the bottom electrode (Full wafer coverage), on which we already knew that AlScN grows well with (0001) texture. XRD investigation showed a perfect c-textured AlScN film with was obtained. The Full width half maximum (FWHM) of the rocking curve is usually an indicator of film microstructure quality. It is already shown that the smaller value of rocking curve FWHM is correlated with larger $d_{33,f}$ and ${k_t}^2$ values in piezoelectric AlN thin film [116, 117]. The excellent value of 1.4° has been measured for FWHM rocking curve for the 0002 peak. Figure 2.9 shows the XRD measurement as well as the rocking curve measurement for the 0002 peak.

SEM investigations on the surface and cross section of the film confirm fibrous columnar structure corresponds to the T-zone growth behavior. Grains' size and roughness of the surface studied by an AFM. Grains diameter varied in the range of 20nm-40 nm. The RMS value for the film roughness was 0.8nm at the center of the wafer and increased by moving towards the edges. This value measured 1.1nm at the edges (Figure 2.10)

Sc concentration and film thickness studied by a depth profile analyses by secondary ion mass spectrometry (SIMS). Results showed about 1% variation in Sc content through the 1.2μm thickness of the film. The thickness varied by 80 nm (out of 1200 nm targeted film thickness) in a radius of the wafer from the center to

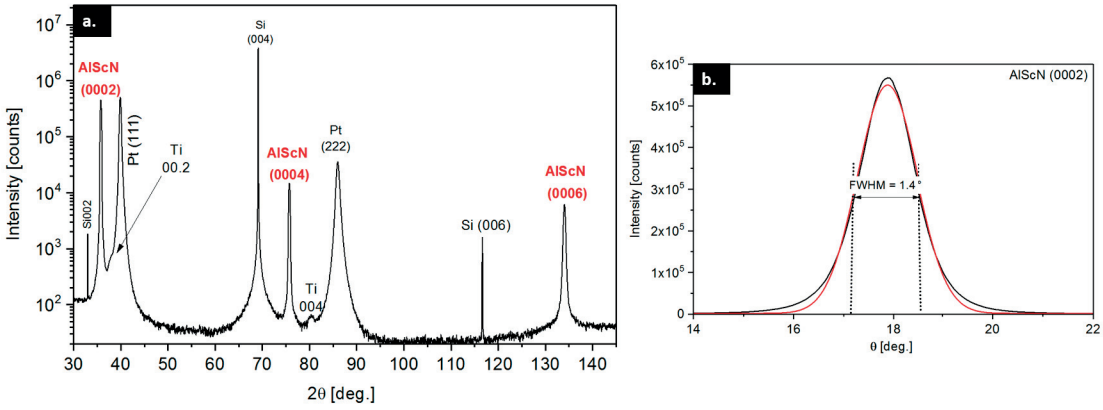

Figure 2.9: (a.) XRD measurement for the AlScN thin film deposited on 100nm Pt bottom electrode with deposition parameters as presented in Table 2.2. The perfectly c-oriented film obtained. (b.) Rocking curve measurement of (0002) peak. The FWHM shows the excellent value of 1.4°.

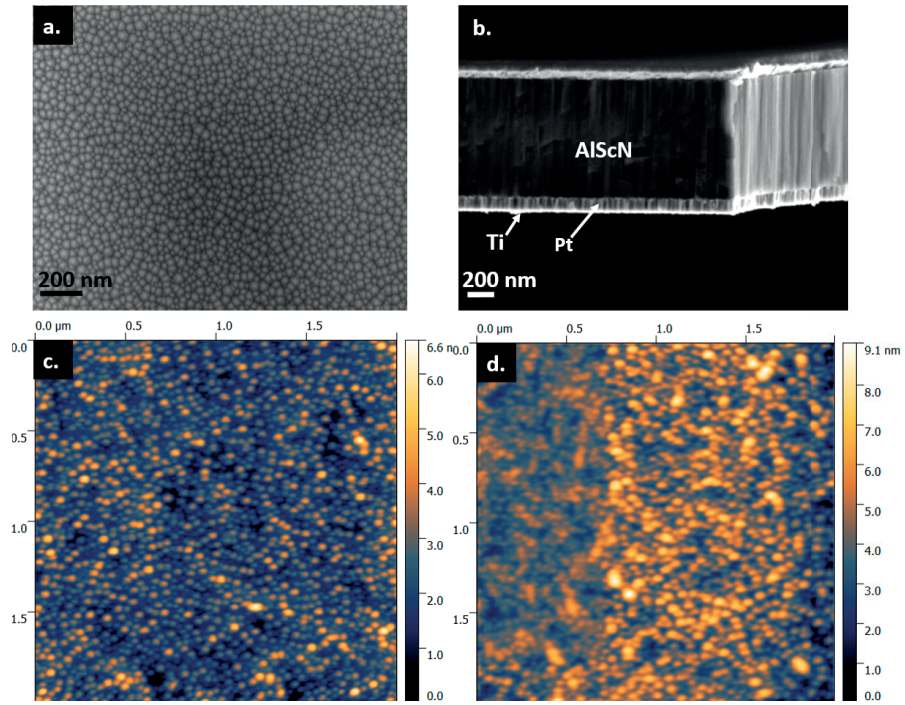

Figure 2.10: SEM images of $Al_{0.83}Sc_{0.17}N$ film growth on 100 nm Pt bottom electrode (a.) Fibrous morphology of surface. (b.) Cross section view of the columnar structure.(c.) AFM picture at the center of the wafer shows RMS= 0.8 nm and (d.) RMS=1.1 nm at the edge.

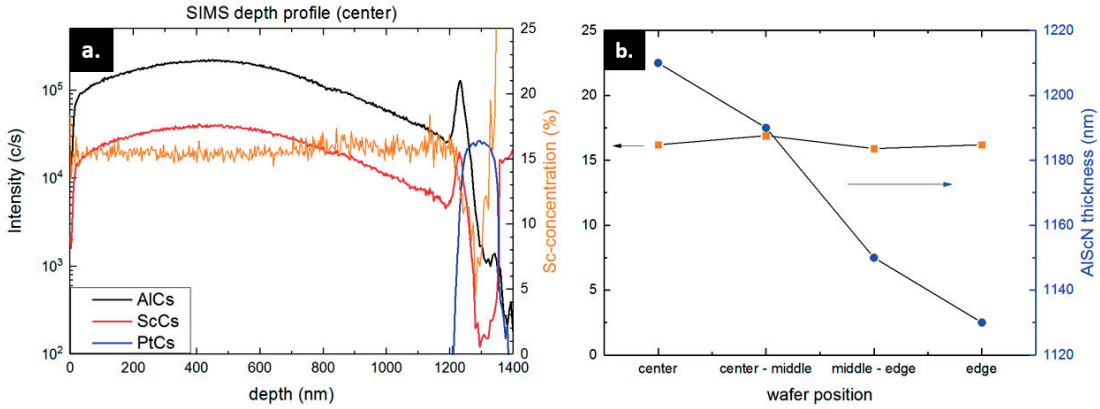

Figure 2.11: SIMS depth profile study showed the Sc varies within 1% range along and in depth of the wafer. The film thickness reduced by 80 nm moving from center to edge. (a.) SIMS depth profile in the wafer center. (b.) Results of SIMS depth profile in different positions along the wafer.

the edge. (Figure 2.11)

The Dielectric constant of the film measured in a parallel plate electrode configuration (capacitance measurement), which was 14.1±0.08. The reference sample of AlN film showed the value of 10.3 by the same setup.

The longitudinal piezoelectric coefficient of the thin film, $d_{33,f}$ measured by FEM assisted double beam laser interferometry(DBLI). The full description of this measurement technique is explained in references [4, 118].The value of the 6.9 pm/V obtained for 1.2 μm thick film. The transverse piezoelectric coefficient $e_{31,f}$ measured by four-points bending measurement Aixact tool which showed value equal to -1.57 $\pm$ 0.07 C/m^2.

2.5 Ex-situ AlN Seed Layer for (0001)-textured $Al_{0.85}Sc_{0.15}N$ Thin Film Grown on SiO_2 Substrate

This section has been already published as an article with the identical title as the section title in IEEE Ultrasonics Symposium (IUS), 2017 [119]. The content reproduced under the permission of IEEE.

Introduction

As described, partial substitution of Al by Sc in AlN wurtzite films leads to a significant enhancement of the piezoelectric properties as long as the wurtzite phase is maintained [38, 39]. This is very promising for improving piezoelectric MEMS devices and enlarging their application range [65, 109, 111, 120]. Nucleation of (0001)-AlScN works particularly well on Pt (111) thin films [87, 92]. However, in some applications such as shear mode or Lamb wave resonators, the growth on insulating substrates may be required [121, 122]. Even though AlN can be grown well oriented on smooth amorphous surfaces of SiO_2 [122, 123], it is not the case for AlScN. AlN seed layers are an evident solution when there is no vacuum break between the AlN and AlScN growth [112, 124, 125]. However, when a vacuum break is unavoidable, an oxide layer is formed on AlN, which makes the regrowth difficult. In this contribution, we show that a mild RF etch can solve the problem.

Experimental and Methods

The employed substrates were a 380 μm thick, double side polished 100 mm silicon wafers with a 200 nm thick thermal oxide layer. First, a 10 nm thick Ti adhesion layer, and a 100 nm thick Pt (111) layer were sputter-deposited. A reactive, pulsed DC magnetron sputtering technique was employed for deposition of the 100 nm thick AlN seed layer, followed by the 900 nm thick polycrystalline $Al_{0.84}Sc_{0.16}N$ film in the same chamber after vacuum break and target change. All the deposition are carried out at 300°C. Metallic Al and $Al_{0.84}Sc_{0.16}$ alloy targets were used for AlN and AlScN deposition, respectively. The deposition carried out by the Spider cluster which described in detail in section 2.4. The RF etch cleaning of AlN was carried out in the same cluster tool, applying an RF power of 200 W for 30 minutes to the substrate chuck of the RF-etch module. The $d_{33,f}$ of the deposited film was measured using an in-house built Double Beam Laser Interferometer (DBLI).

Results and Discussions

Microstructure

The AlN seed layer grew with a pure (0001) texture on the Pt (111) layer. Without prior RF etch cleaning, the AlScN thin film grown on this seed layer showed still a majority of grains with (0001) orientation, however, there was a substantial population of other orientations having the plane indices $(10\bar{1}1)$, $(10\bar{1}2)$, $(10\bar{1}3)$ and $(10\bar{1}4)$, as revealed by X-ray diffraction (Figure 2.12). Correspondingly, DBLI measurements show a poor $d_{33,f}$ $(= e_{33}/c_{33}^{E})$ value of 1.1 pm/V for this film. The

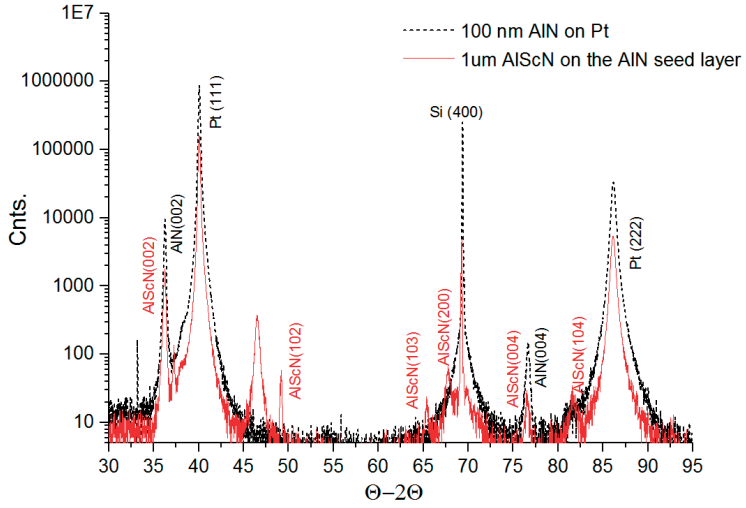

Figure 2.12: XRD pattern of the 1μm thick AlScN grown on a 100 nm thick AlN seed layer. The double layer obtained without RF-etch cleaning of the first layer.

reason for the poor texture becomes evident by TEM investigation (Figure 2.13). EDX hyper mapping highlights an 8 nm thick oxide layer at the AlScN/AlN interface. High-resolution TEM shows that this oxide layer is disturbing the epitaxial growth of AlScN, and hence the 0002 texture is not copied from the AlN layer. The inserted FFT images taken of both sides of the interface confirmed the texture loss. With RF-etch cleaning, the AlN layer regained its function as a seed layer. X-ray diffraction revealed a completely (0002)-textured film with no other orientations (Figure 2.14). There is still a very thin, residual layer with oxygen at the interface, having a composition of about $N_{3/4}O_{1/4}$ on the N-site, based on EDX studies. The local epitaxy is confirmed by high-resolution TEM images (Figure 2.15). Diffraction patterns confirms the pure (0002)-texture on both sides of the AlN/AlScN interface. Hence, the partially oxidized interface (mono) layer does not impede epitaxy.

Piezoelectric Characterization

The films were characterized by FEM-assisted double beam laser interferometry (DBLI) to determine the clamped thin film coefficient $d_{33,f}$. Figure 2.16 shows a schematic of the fabricated stack and the notation used for the calculations and simulations. DBLI measures the displacement between the bottom of the Si substrate (D), and the top Pt electrode surface (C). The piezoelectric coefficient $d_{33,f}$ is defined as: $d_{33,f}^{DC} = \frac{\Delta_{DC}}{U}$, where Δ_{DC} is the displacement between the D-C planes and U is the applied voltage between the top and the bottom electrode. The

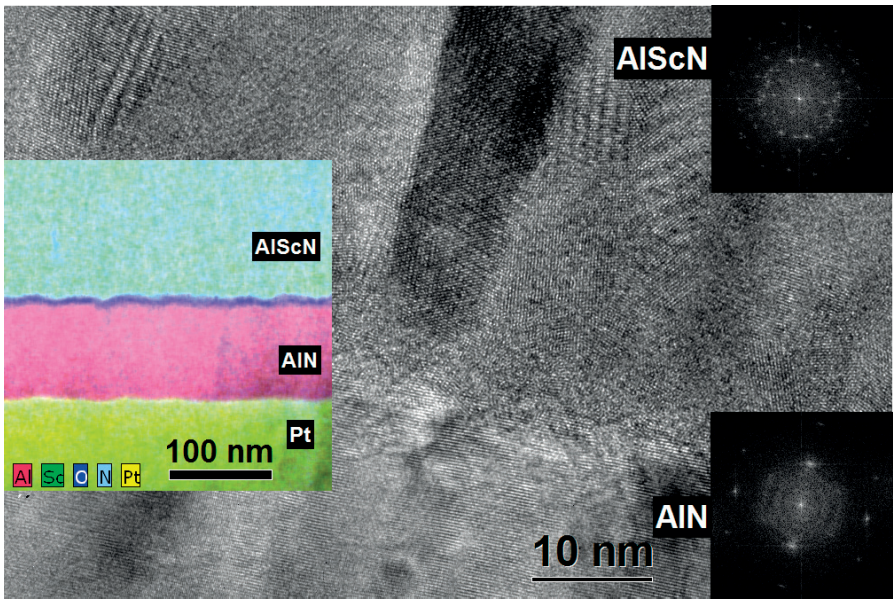

Figure 2.13: High-resolution TEM, FFT diffraction pattern, and EDX hyper map of AlScN film grown on untreated air-exposed AlN seed layer. An 8 nm thick oxide layer is seen at the AlN/AlScN interface.

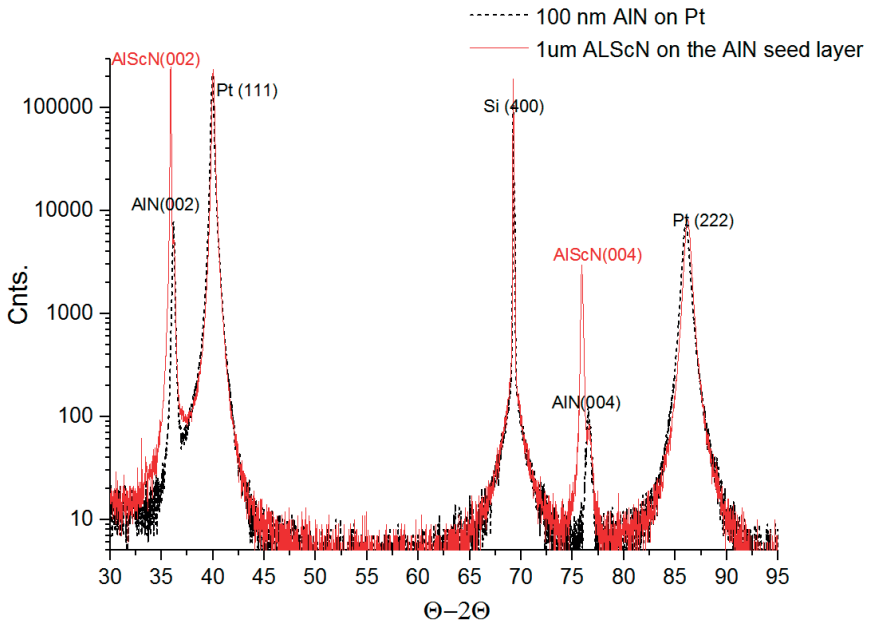

Figure 2.14: XRD pattern of AlScN/AlN/Pt layers. An RF etching was applied to the AlN seed layer prior to AlScN deposition.

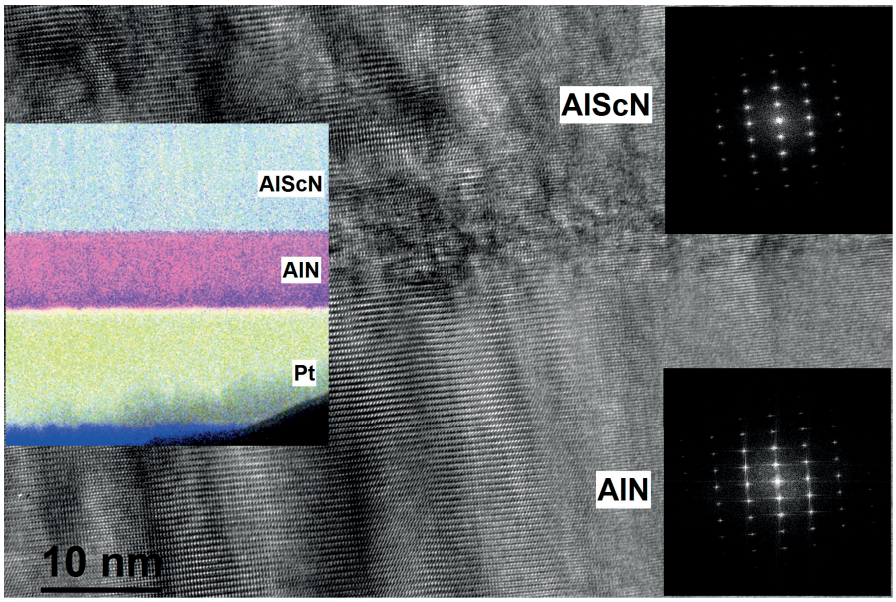

Figure 2.15: High-resolution TEM, FFT diffraction pattern, and EDX hyper map of AlScN/AlN double layer processed with RF etch cleaning of the AlN seed layer.

top electrode diameter impacts significantly on the measured displacement due to the impact of $e_{31,f}$ (see also [6]). In this work, we have a composite active layer. FEM simulation was applied to assess the $d_{33,f}$ of the AlScN layer. In fact, one cannot evaluate $d_{33,f}$ precisely without finite element modeling. Assuming that the composite behaves like a film with average piezoelectric properties, one can derive the response also by analytical expressions. In this frame, we consider the AlN and AlScN layers as series pistons acting in phase for the mechanical part, and considering that we deal with a series capacitors for the dielectric part. The applied voltage between the top and bottom Pt electrodes, U, is the sum of the

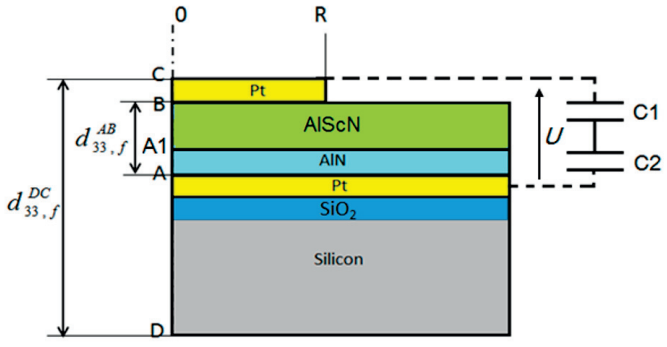

Figure 2.16: Schematic view of the produced and simulated stack of thin films.

voltage across each capacitor: U=U_1+U_2. Likewise, the mechanical deflection of AlScN/AlN composition layer is the sum of the mechanical displacements:

$$\Delta_{AB} = \Delta_{AA_1} + \Delta_{A_1B} \tag{2.4}$$

Thus, the piezoelectric coefficient of each layer is:

$$\begin{cases} d_{33,f}^{AlScN} = \frac{\Delta_{A_1B}}{U_1} \\ \\ d_{33,f}^{AlN} = \frac{\Delta_{AA_1}}{U_2} \end{cases} \tag{2.5}$$

The piezoelectric coefficient of the complete layer stack is:

$$d_{33,f}^{AB} = \frac{\Delta_{AB}}{U} = d_{33,f}^{AlScN}\frac{U_1}{U} + d_{33,f}^{AlN}\frac{U_2}{U} \tag{2.6}$$

The piezoelectric coefficient of AlScN layer alone is then derived as:

$$d_{33,f}^{AlScN} = d_{33,f}^{AB} + \frac{\varepsilon_1}{\varepsilon_2}\frac{d_2}{d_1}(d_{33,f}^{AB} - d_{33,f}^{AlN}) \tag{2.7}$$

where ε_1, ε_2, d_1, and d_2 are dielectric permittivity and thickness of AlScN and AlN layer, respectively. For AlN, the standard values $d_{33,f}^{AlN}$ =3.9 pm/V and ε=10.3 were used [61]. Dielectric permittivity of AlScN is extracted from the static capacitance measurements of four different diameters of electrodes from 500 to 800 μm (Figure 2.17.a) which resulted in the value of ε_1=14.1. Using this value for the analytical derivation, a $d_{33,f}^{AlScN}$ of 6.9 pm/V was derived from the complete stack response of $d_{33,f}^{AB}$ = 6.3 pm/V. For comparison, 3D FEM modeling was carried out by COMSOL. Top electrodes diameters were swept in a range of 500 to 800 μm in steps of 100 μm. The applied voltage magnitude was 1 V. The mechanical displacement of the stack simulated by varying $d_{33,f}^{AlScN}$ and results fitted with DBLI experimental measurements of the whole stack fitting the behavior for all capacitor diameters. (Figure 2.17.b). The best so obtained fit resulted in $d_{33,f}^{AB}$ = 6.6 pm/V, and $d_{33,f}^{AlScN}$ = 6.85 pm/V, which is very close to the less demanding procedure proposing that the good $d_{33,f}$ values are valid for 525 μm diameter dots.

Conclusion

The vacuum break between deposition of an AlN seed layer and the AlScN film leads to oxidation of AlN surface, preventing AlScN epitaxial growth on the seed layer. This results in a poor texture and a low piezoelectric response. The introduction of a suitable RF etch step before AlScN deposition eliminates the oxide layer and

enables AlScN to follow the seed layer texture. Therefore, c-texture AlScN films can be produced in this way. The experiments were made including a Pt electrode layer below the seed layer in order to assess piezoelectric properties. Of course, the same seed layer may also be used on insulating layers like SiO_2 or Si_3N_4. The $d_{33,f}$ of AlScN film was assessed by FEM assisted DBLI measurements. A value of $d_{33,f}^{AlScN}$=6.9 pm/V was obtained, which is somewhat higher than predicted by Caro et al. (5.9 pm/V) [113].

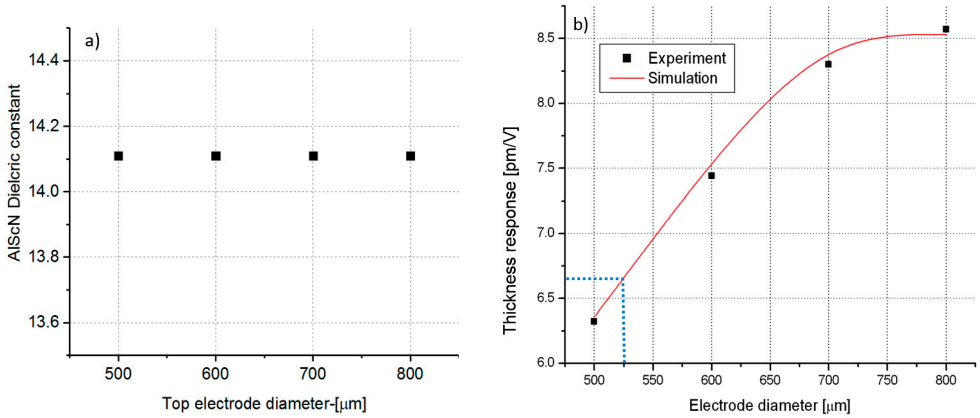

Figure 2.17: (a) Dielectric constant of AlScN layer vs capacitor electrode size. (b). Simulated and experimental results for $d_{33,f}^{DC}$ vs top electrode diameter. Piezoelectric coefficient of stacked AlScN/AlN is $d_{33,f}^{AB} = 6.6$ pm/V which corresponds to spot size of D=525 μm .

2.6 Abnormal Grain Growth in AlScN Thin Films Induced by Complexion Formation at Crystallite Interfaces

This section was published as a journal paper with the same title as the section title [126]. The content reproduced under the permission of Wiley.

Introduction

It is explained in Section 2.4 that the Dc-pulsed reactive magnetron sputtering is the optimal process to obtain a c-textured piezoelectric AlN thin film for MEMS

applications.Of course, the growth conditions must correspond to the so-called T-zone of Thorntons growth classification [90]. By adding scandium to the AlN thin film, it is often observed that abnormal grains (AG) with different morphology and crystallographic orientation are formed, as reported earlier by Fichtner et al. [127], and as shown lately by Mertin et al. for various film compositions [6, 128]. Their density increases with increasing Sc content [6, 127, 128], but they are also observed at relatively low Sc concentrations [129]. They enhance the roughness of the film and reduce the piezoelectric activity. They degrade the electromechanical coupling coefficient k^2 and the quality factor. In surface acoustic wave devices, rough surfaces lead to wave attenuation and wave scattering. Fichtner et al. attributed the existence of AG grains to the nucleation of different orientations at the film-electrode interface. Of course, it was always observed that grains of other orientations than (0001) were also growing during pure AlN deposition, so for instance with (1000) or $(10\bar{1}1)$ orientations. But this was due to different process conditions than those known for promoting (0001) growth [87, 130]. For instance, misoriented grains were reported by Hrkac [131] in pure AlN films deposited by sputtering at 400°C, but the authors did not report about a different morphology of these grains. The remarkable issue with abnormal grains in AlScN is the fact that they grow at deposition process conditions at which AlN grows perfectly in (0001) orientation. It is clear that the AG growth occurs due to the presence of Sc atoms. No evidence of an effect due to the presence of Sc was presented by Fichtner et al. A reduction in (0001) texture with increasing Sc content in AlScN films reported by Zywitzki et al. [132]. Also, other impurities may cause the same effect. Mayrhofer et al. [133] reported a reduction in the preferential (0001) texture and an increase in the surface roughness with increasing Y content in $Al_{1-x}Y_xN$ films. A general finding between these studies is that the high content of impurity species (which in the case of the present study is Sc) can disrupt growth or nucleation behavior, causing nucleation of AOGs and the loss of the desirable (0001) film texture.

The question of where abnormal grains nucleate is often treated controversial in the literature, as reported by Nicolay et al. for the case of ZnO, [134]. In this work, we shall show that the origin of AGs in $Al_{1-x}Sc_xN$ is not the primary nucleation on the substrate, but a secondary nucleation in the course of uniaxial, columnar growth. We show that specific deposition conditions promote abnormal oriented grains (AOG) nucleation, which have a specific range of crystallographic orientations deviating substantially (60°-90°) from the (0001) growth direction. We also show that AOGs can be formed even at lower Sc concentrations of 10 to 16%, i.e. far away from the existing limit of the wurtzite phase. We characterized in detail the structure of films having Sc concentrations (x) in the range from 0 to 43 at.%, using advanced TEM techniques in order to determine the chemical composition of grain boundaries, and the orientations of the observed AOGs. The

combined results allowed for a consistent scenario on the growth mechanisms in the metastable Al-Sc-N ternary system.

Based on the statistical crystallographic information provided by nanodiffraction mapping of plain-view TEM samples, we could prove that the faceted AOGs have rather random growth directions. The AOGs appear at a later stage of film growth. We presume that the segregation of Sc to grain boundaries disrupts the growth behavior due to a secondary nucleation of a Sc rich composition in the rocksalt structure, followed by nucleation of a wurtzite AOG as the Sc flux is not large enough to maintain the embryonic grain in the rocksalt structure. As such, growth direction and polar direction are lost. We show that higher Sc contents lead to a larger fraction of AOGs. In addition to the influence of Sc concentration, other specific deposition conditions were found to promote AOG growth.

We emphasize that it is not the purpose of this study to present optimal deposition condition for functional piezoelectric properties of the AlScN films, nor to find detailed correlations between process parameters and film characteristics. For this reason, the details concerning the deposition processes are omitted. The main focus of our paper is to describe the features involved and explain the occurrence of AOGs in AlScN thin films.

Experimental

AlScN thin films were deposited at 300°C to 350°C by a reactive magnetron sputter deposition process using a pulsed DC source, as first described in ref [86] for pure AlN, and later also used for AlScN [109, 111, 128]. AlScN cannot be grown at much higher temperatures. At 800°C, a phase separation into AlN and ScN rich phases was observed [135]. Scanning Electron Microscopy (SEM) was used to image the topography of the surface of the different films and measure their thickness. The chemical composition was measured in SEM-EDX at 8 kV for all the films. Because the SEM-EDX spectra were taken under similar conditions, differences greater than $\pm$ 0.5 at.% in Sc content (Sc/(Al+Sc) were considered as relevant in relative comparisons between investigations. The plain-view and cross-section TEM specimens were prepared following conventional methods: mechanical cutting, gluing, mechanical thinning and polishing and finally ion milling with Ar in a PIPS installation. The AlScN TEM samples are easily amorphized under the ion-milling beam. Amorphous material was observed in thin regions ($\leq$ 30 nm) even for low ion energies (0.1 keV) and even for samples ion milled at low temperature (-100°C). Such amorphization makes it difficult to observe the structure of the complexion phase situated at high angle GBs by Cs-corrected HR-STEM in cross-sectioned samples. The strain present in the investigated AlScN films together with the

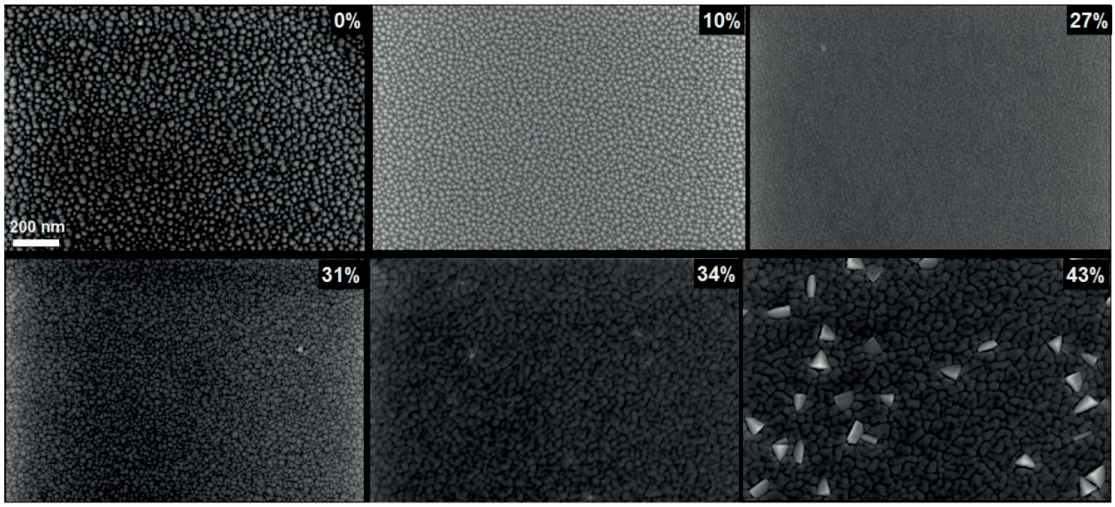

Figure 2.18: Series of six SEM images showing the increase of AOGs with increasing Sc content in 500 nm thick AlScN films.

presence of the piezoelectric effects made it difficult to observe these regions in the plain-view samples. The conical shape of the AOGs impedes the observation of Sc-segregation in the plan-view samples by STEM-EDX hypermap. TEM analysis was performed at 200 kV on different microscope platforms: OSIRIS and Talos for more conventional investigations (bright and dark-field, SAED, HAADF) and for Hyper-map STEM-EDX; and JEOL 2200FS for nanodiffraction mapping. The Automated Crystal Orientation Mapping (ACOMTEM) with the NanoMegas ASTAR system [136–138] employed in the present paper uses a transmission electron microscope (TEM) to collect and index nanodiffraction patterns over a scanned area of 2 μm^2. NanoMegas ASTAR system was mounted on the JEOL 2200FS, having a spatial resolution of 1nm with a 0.5nm step with C2 aperture of 10μm. The colors in the maps are given with respect to the growth direction. Red corresponds to (0001) orientation, blue to $(11\bar{2}0)$ and green to $(10\bar{1}0)$ in the hexagonal wurtzite lattice.

Results and Discussion

We note that deposition conditions were aimed at producing AlScN thin films with a (0001) texture by using parameters optimized for pure AlN. The evolution of the surface morphology of a thin films series (identical substrate, film thickness, temperature, gas pressure, deposition equipment for co-sputtering from pure metal targets) with increasing Sc content is shown in Figure 2.18. Abnormal grains (facetted) were observed in this series with Sc content (x=Sc/(Al+Sc)) higher

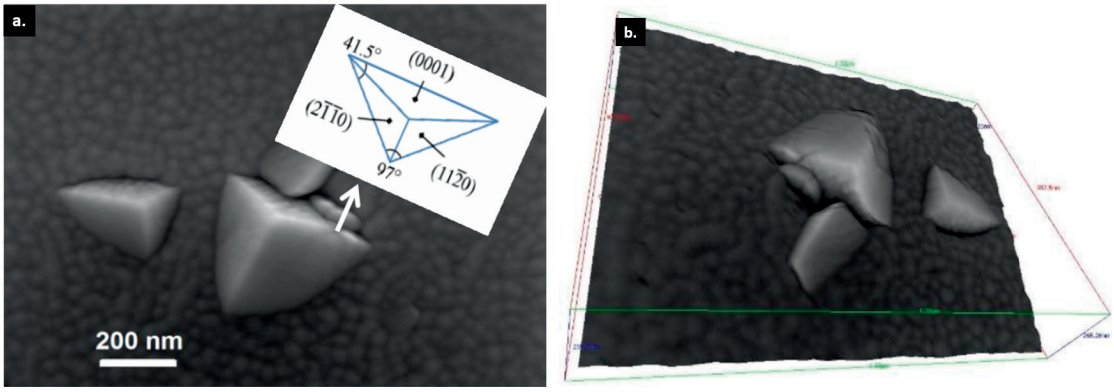

Figure 2.19: Details of the AOGs appearing on a 1000 nm thick AlScN thin film (16% Sc): (a.) Direct SEM observation, (b.) 3D-surface reconstruction based on the SEM-tilting method.

than 27 at.%. Their size and surface density increase with higher Sc content. A high-resolution SEM picture of such a facetted AOG is shown in Figure 2.19 for a 1 μm thick AlScN (16% Sc) film deposited on a different tool (Spider), and employing an alloy target. Two of the facets look smooth, the third facet appears rough and textured. The smooth facets have a morphology and orientation corresponding to the family of crystallographic planes $\{11\bar{2}0\}$ or $\{10\bar{1}0\}$, which pose lower diffusion barriers for ad-atoms than (0001) planes, as reported in ref [139] . The facet with a corrugated (striped) surface corresponds thus to a (0001) plane. The top of the largest grain was 140 nm above the film surface. The angles between the surface normal of the facets and the substrate normal were measured from SEM 3D-reconstruction (Figure 2.19.b) as 50°, 60° and 73°. The facet angles together with an estimation of the in-plane orientation of the facets indicate that the smooth facets are $\{11\bar{2}0\}$ planes, like in the case of biaxial texture development in AlN thin films [140]. Between two neighboring AOG (pyramidal morphology), the surface of the film is more recessed, due to the shadowing effect of the faster growing, pyramidal AOGs. The relative gain in height amounts thus to 14%. For comparison, the maximum height of 40 nm above the normal grains in the case of 500 nm thick, 43% Sc film is smaller (only 8 %). The AOG dimensions become larger with increasing film thickness, as deduced from Figure 2.20 that shows the surface morphology of 1 μm and 2 μm thick films deposited with similar conditions. The increase of the AOGs mean size is around 30%, and the increase of the surface coverage by AOGs is 80%. At these high-surface densities, AOGs form complex, compact block morphologies like those shown in Figure 2.20.b.

AOGs were observed in TEM cross-section specimens (Figure 2.21.c and Figure 2.22.a and b). The AOGs were not present near the substrate interface but at

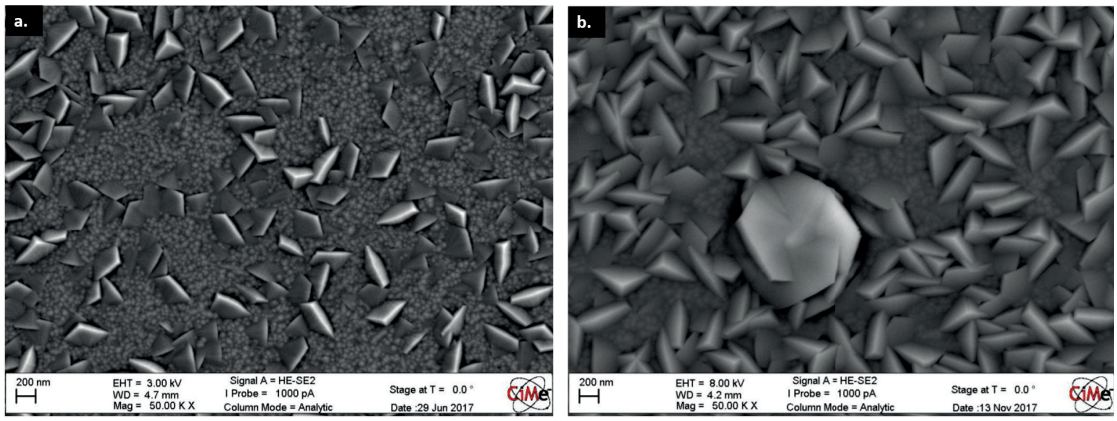

Figure 2.20: (a.)SEM image of 1 μm thick AlScN (16% Sc) film. (b.) SEM image of 2 μm thick AlScN (16% Sc) film.

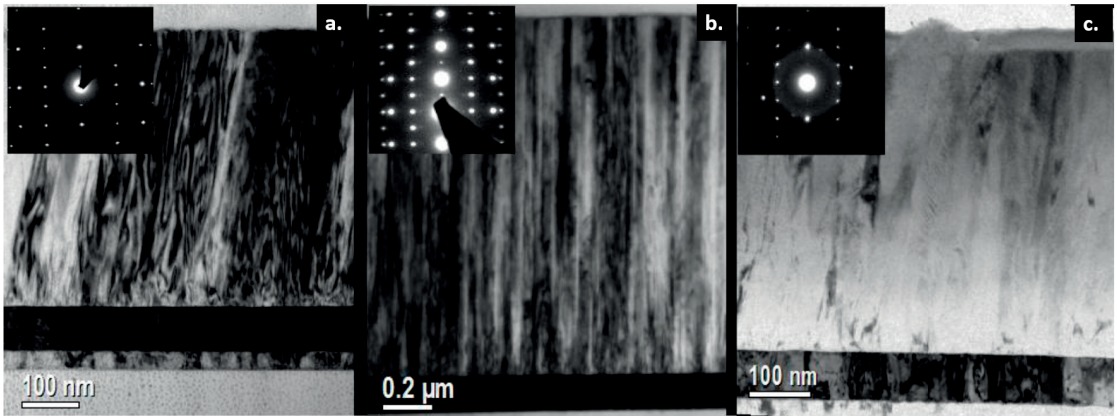

Figure 2.21: Series of 3 cross-sectional TEM images for: (a.) AlN, (b.) AlScN (16% Sc), and (c.) AlScN (43% Sc).

heights that are a few hundreds of nanometers away from the substrate.

As observed in the DF-images and in Figure 2.23, these grains have a conical shape, which means that they grow faster into the width than the neighboring (0001) grains, resulting in an increase of the surface fraction occupied by these grains with increasing film thickness. The dark-field image in Figure 2.22.a was taken using the (0002) lattice reflection. The AOGs appear dark and have a different crystallographic orientation compared to other grains in the region. It was also confirmed by individual SAED patterns taken on some of the AOGs that they do not exhibit (0002)-orientations (not shown here). For some AOGs, (0002) diffraction spots were observed, though only at large specimen tilt angles with respect to the film growth direction. On average, the preferentially oriented (0001)

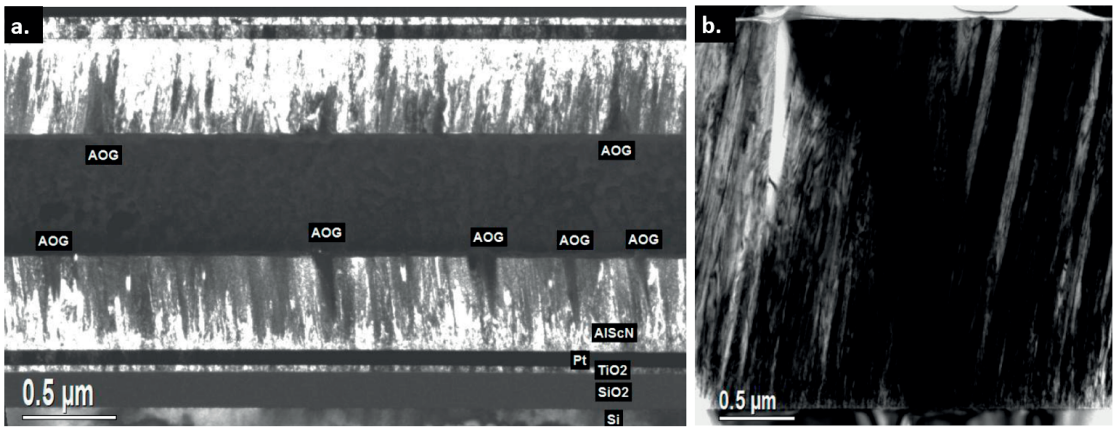

Figure 2.22: (a.)DF-TEM image based on the (0002) diffraction spot of an AlScN (43% Sc) film. AOGs are darker. (b.) BF-TEM cross-section image showing the development of an AOG (white) in an epitaxial AlScN (16% Sc).

grains have a small range tilt with a maximum of 5°. This tilt is due to the average direction of incoming flux, which varies slightly across a wafer [141]. From these observations, we conclude that the majority of these AOGs have an orientation that is different from the dominant (0001)-orientation, despite the fact that the (0001)-orientation is the exclusive one at the initial growth stage. Their orientation varies with respect to the substrate plane, in contrast to the situation when a competing texture nucleates directly on the substrate.

A reduction of the c-axis texture in AlScN films with increasing Sc content was also observed in TEM investigations by Zywitzki et al. [132], which supports our observations of AOGs nucleating in the later stage of film growth.

Comparing the in-plane and out of plane orientations obtained with the ACOM technique for plan-view TEM specimens from AlN and AlScN (43% Sc) films (Figure 2.23) we note the existence of coherency domains (low-angle GB) with similar sizes in both films. The difference between the two films is given by the AOGs, present in large number in 43% Sc films, which showed a different crystallographic orientation. These AOGs have different out of plane orientations, as already discussed, and thus have high-angle GBs with the adjacent c-axis grains. The angle of tilt between the growth direction and the (0001) crystallographic direction of the AOGs (indicated by a color other than red) vary between 60° and 90° as indicated in the Figure 2.23.c bottom row. This result supports our hypothesis that the facet with the roughest surface, as shown in Figure 2.19.b at a 73° inclined AOG, corresponds to a (0001) orientation. A cross sectional ACOM image is shown in Figure 2.24, highlighting the large angle mismatch between normally and abnormally oriented grains. It also shows clearly the formation of the

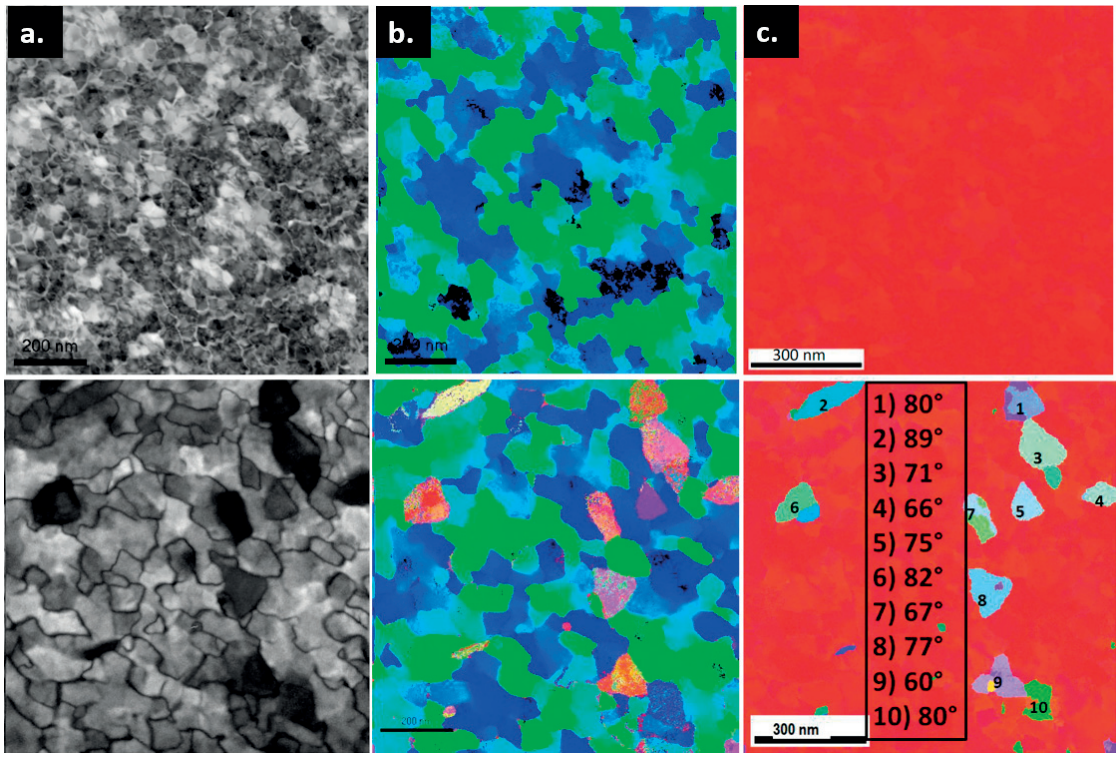

Figure 2.23: Nanodiffraction mapping of AlN (top row) and AlScN (43% Sc) (second row) films showing the orientation of the grains with respect to the c-axis, as obtained from plan view images: a. virtual BF image. b. in-plane orientation map (RD direction), c.out-of-plane orientation map (ND direction). Uniform colors have an angular width of 5°. Stereographic triangle shown in Figure 2.24 indicates the color code for crystallographic grain orientation.

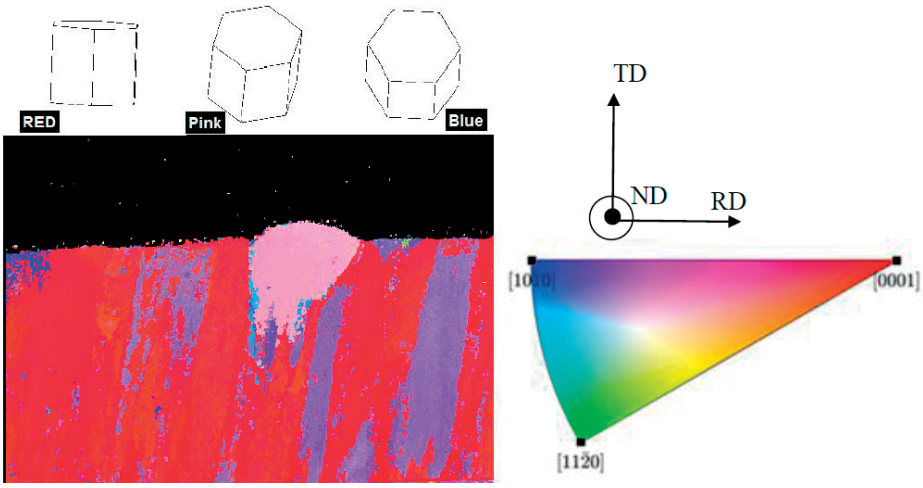

Figure 2.24: Automated crystal orientation mapping image of a cross-section TEM foil of the AlScN (43% Sc) thin film. The inverse pole figure map is taken along the TD direction (growth direction). Red color signifies grains oriented along (0001)-direction (c-axis), blue along (10$\bar{1}$0)-direction (a-axis).

AOG in the upper part of the film. The Hypermap STEM-EDX investigations (see Figure 2.25 show that the surface oxide layer of the AlScN films (with 10 and 16% Sc) is 3 to 4 times thicker than the oxide layer on AlN surfaces. Apparently, the Sc doped materials allow for a larger diffusion depth of oxygen, thus leading to a thicker oxide scale. We observed higher Sc concentrations at grain boundaries (Figure 2.26), as obtained at some given process conditions. Figure 2.26.a shows grain boundaries between normally oriented grains, and Figure 2.26.b, grain boundaries between abnormally oriented grains. In the latter case also the oxygen signal was plotted. The integrated line-scans clearly indicate the variation in the signal intensity of all elements in the sense that Sc and O are increased, and Al and N are decreased in the boundary. In compact AlScN films (16% Sc) having a microstructure with dense and even coherent grain boundaries (Figure 2.27.a), the Sc/Al signal ratio showed only a minute accumulation of Sc at grain boundaries, even for films with 43% Sc (Figure 2.27.b). Moreover, these compact grain boundaries did neither show an oxidation after TEM sample preparation and the exposure to air. The variation in Sc/Al ratio observable in Figure 2.27.b was measured across the start tip of an AOG cone. The minuscule concentration changes can only be observed by sensitive techniques like those using the FEI SuperX technology and acquiring STEM-EDX Hyper-maps, which probably explains that no such accumulation was found by Fichtner et al. [127]. More careful analysis (smaller electron beam, longer time) was performed and showed Sc segregation even in epitaxial films (16%) grown on sapphire (0001) (see the Sc/Al plot in Figure 2.27.a). The corresponding

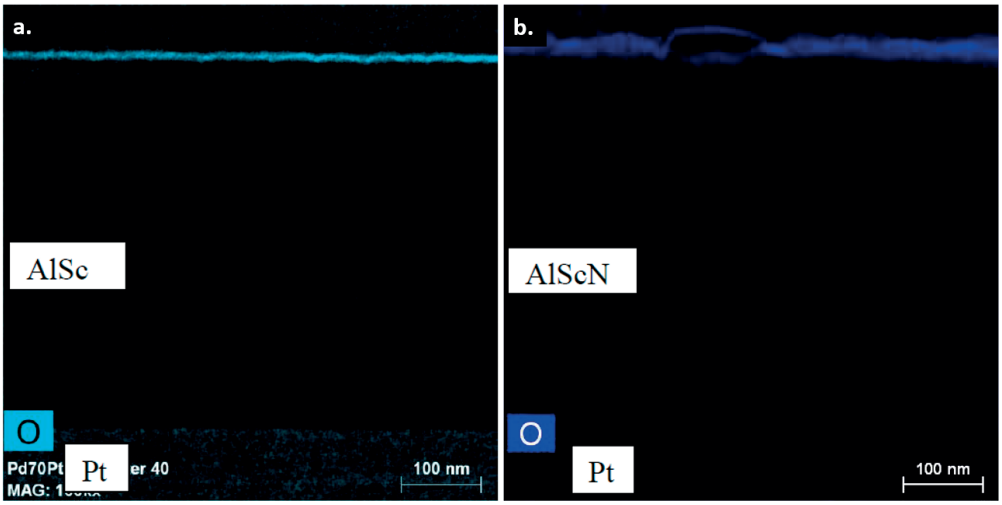

Figure 2.25: O-mapping in AlN (a), and AlScN, 43% Sc (b) thin films. Thickness of the oxidized layer is 3 to 4 times larger in AlScN films.

boundaries between the (0001)-oriented grains must be very dense, as no oxidation was observed. Because the oxidation was observed only at the non-compact grain boundaries, we assumed that it is a post-process phenomenon. In the case films of 43% Sc films grown on polycrystalline Pt (111), a small increase of the Sc/Al ratio signal was observed on a 5 nm wide region along AOG boundaries. The relative increase of the Sc concentration (Sc/(Al+Sc)) in this region was in the range of 8%. We observed that the signal variation at GBs depended also on the orientation of GB with respect to the electron beam, on the sample thickness and also on the type of GB (open, tight, disorientation angle). It would be very interesting to combine crystallographic and chemical information from plain-view experiments. Unfortunately, the conical shape of the AOGs together with the limited down thickness for film survival in the TEM plain-view sample (around 70 nm) impedes to prove Sc-segregation in the plain-view samples.

The formation of AOGs is a deviation from the optimized growth as known from high performing AlN thin films with their polar (0001) or (000$\bar{1}$) texture. First, a short description of growth properties for this case is given, and then we describe the influence of scandium on the growth dynamics. In an investigation on the texture preference between (10$\bar{1}$0) and (0001), Ishihara et al. [130] found that the nucleation and growth of (10$\bar{1}$0) oriented grains are promoted by process conditions leading to shorter mean free paths. Their experimental findings are as follow: growth of c-axis textured films was improved by increasing the mean free path (lower pressure), by decreasing the substrate-cathode distance (less scattering), by increasing the power (more secondary electrons ejected from the target), and

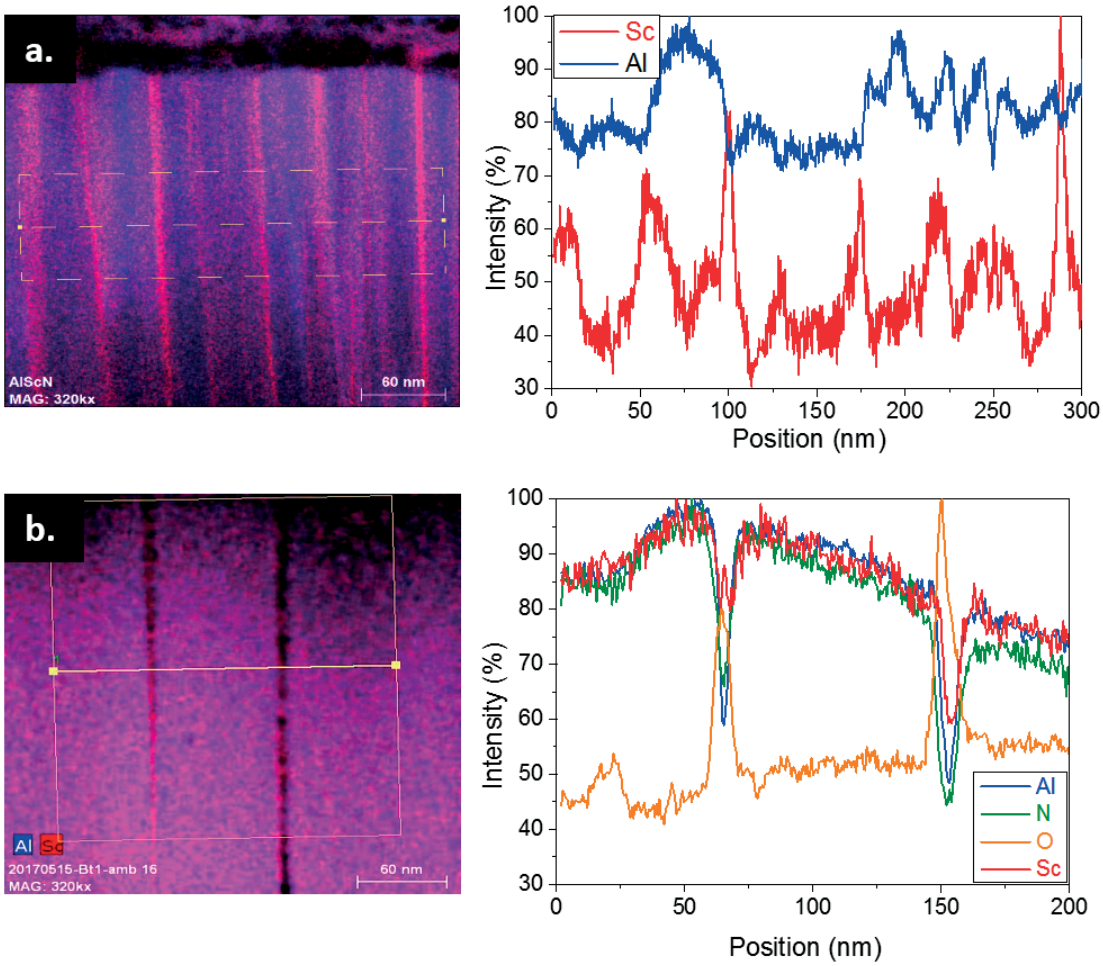

Figure 2.26: (a.) STEM-EDX Hyper-map on 10% Sc film having no AOGs, i.e. all grains are c-axis oriented, and the angular mismatch is limited to in-plane rotation. The film was grown on a Pt (111) electrode, mechanical stress = -350 MPa. The Sc enrichment at GBs is clearly observed in the transversal line scan (right). (b.) STEM-EDX Hyper-map of a film containing mainly AOGs (16% Sc) on Pt (111) electrode (low tensile stress). Oxygen is exclusively observed at grain boundaries (see the transversal line scan on the right) and substitutes there a part of the nitrogen.

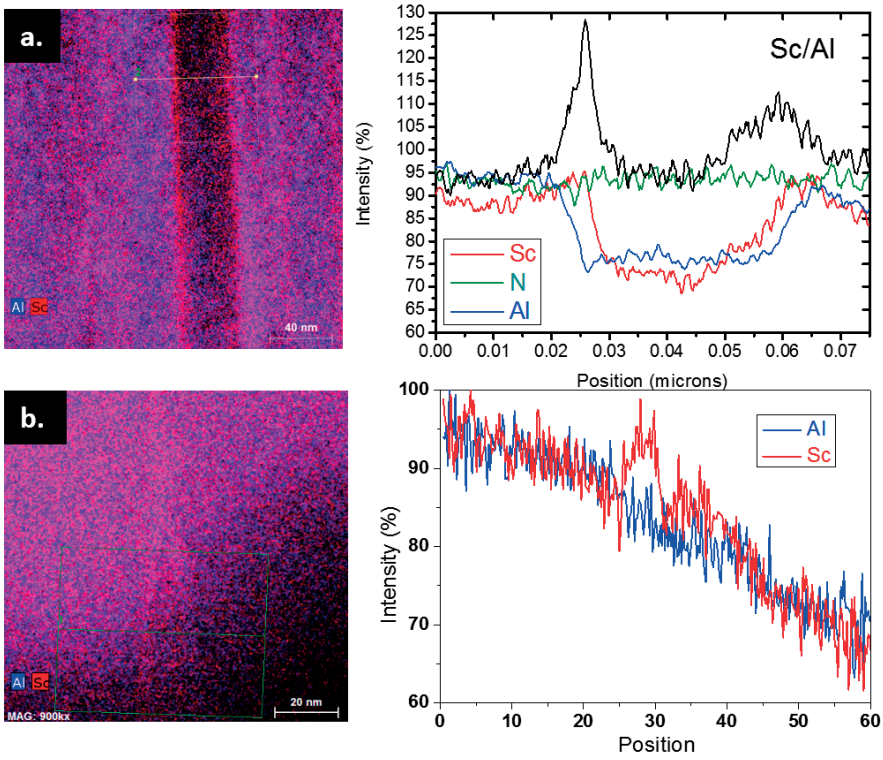

Figure 2.27: (a.) STEM-EDX Hyper-map and the corresponding transversal line scan showing Sc enrichment in an AlScN (16% Sc) film grown epitaxial on sapphire. No oxygen contamination at this compact GB was observed. (b.) STEM-EDX Hyper-map and the corresponding transversal line scan showing Sc enrichment at large angle GB in an AlScN (43% Sc) film on Pt. Here as well, no oxygen contamination was observed.

by increasing the nitrogen part in the sputter gas. All these observations are compatible with conditions for an increased energy of ions bombarding the growing film: less ion scattering by gas molecules, and a higher negative charging of the film surface by electron impact. This was indeed shown by Dubois and Muralt [87] by measuring the longitudinal piezoelectric coefficient as a function of these process parameters. They showed that the piezoelectric properties increased with the absolute value of the substrate bias voltage (it is negative) up to a given saturation, independently of which parameter was changed to get a higher value of the self-bias voltage. These experiments show also that a defined polar texture (N-polar in this case [142]) requires a minimal ion bombardment. The bias effect on the texture was also confirmed by the finding of Takikawa et al. vacuum arc deposition without bias produced $(10\bar{1}0)$ oriented films, and a transition to (0001)-orientation was observed with increased negative substrate bias voltage. Taking all these facts together, and considering as well the low deposition temperature, it is evident that (0001)-textured AlN grows in a process window corresponding to zone-T [90]. This means that diffusion occurs primarily on surfaces exposed to the energetic atomic and ionic fluxes. Diffusion processes are limited to ad-atom diffusion which is the controlling factor in growth. In high quality AlN thin films, ad-atom diffusion also takes place across grain boundaries. High resolution TEM, showed that the c-planes of neighboring grains are on the same height. No step and apparently no diffusion barrier is evidenced at such coherent grain boundaries. This type of GB was also observed in TiN growth by Mahieu et al. [143]. This growth mode was evidenced through the film microstructure evolution resulting from an oblique arrival of atoms. When the substrate is tilted with respect to the target plane, there is no grain tilting occurring for the first few 100 nm, and the c-planes grow parallel to the substrate plane [143]. In this stage of the growth, the immobilization (chemisorption) of the ad-atoms occurs only after surface diffusion, thus without any impact from the incidence angle. Only after a certain film thickness, grain boundaries start to incline. The c-planes, however, remain parallel to the surface. This means that after a certain thickness, asperities start to appear at the grain boundaries, and form an ad-atom barrier. The grain boundaries grow then towards the flux according to the well-known mechanism described by Nieuwenhuizen and Haanstra [144]. The c-planes do not continue across such grain boundaries. Only c-axis oriented grains are observed also in this case with tilted grain boundaries.

Scandium differs in three properties with respect to aluminum: It does not form 4-fold coordinated structures in simple compounds. In 6-fold coordination Sc^3+ exhibits a 21 pm larger radius than Al^{3+} in the same coordination [145] , and is then about 30% larger than Al^{3+}. Furthermore, Sc is less electronegative than Al, which explains in part the larger piezoelectric effect of AlScN. The Al position in wurtzite structure is not the ideal environment for Sc with respect to

coordination and available space. For this reason, chemisorption of Sc atoms occurs at a lower rate than the one of Al and in a stationary situation, Sc is then abundant in the ad-atom layer. The interior of grains is expected to grow with a composition corresponding to that of the physical vapor, if we neglect Sc desorption. (note that the measured compositions in the films corresponded very closely to the target compositions).

The results shown above indicate, however, that other bonding sites available at the grain boundaries are more attractive for Sc. There are defects generated due to bad in-plane alignment across the boundaries when the angle mismatch is large, which occurs in about half of the grain boundaries (see Figure 2.23). Some of the defects will offer more space or a higher coordination for Sc atom incorporation. These sites form Sc traps and lead to an enrichment of grain boundaries with Sc, as revealed in Figure 2.26 and Figure 2.27. The crystalline complexion phase at the grain boundaries remains in the wurtzite phase (Figure 2.26.a), however with a larger Sc concentration. The in-plane lattice constant a is expected to increase with increasing Sc concentration, leading to better accommodation of Sc, and thus to a larger Sc chemisorption rate. As a result of such segregation, the (0001)-oriented columnar grains have a Sc enriched surface layer at their side walls (kind of complexion). The resulting distortions will eventually lead to higher energy barriers at GB, and result in the formation of topographical anomalies. This self-stabilization of Sc rich grain boundary zones can lead to a situation that there is too much Sc present, which significantly distorts the unit cell and destabilizes the wurtzite structure. This will lead to the nucleation of a rocksalt phase. It can be imagined that at the same time the ad-atom diffusion across grain boundaries is hindered by such nuclei forming discontinuities, or nanoscale asperities. Following this reasoning, a higher Sc concentration is expected between grains with a bad match of in-plane orientation (leading to high energy grain boundaries), and therefore a higher nucleation density of abnormal grains. Figure 2.23 shows that many (0001)-oriented grains exhibit the same in-plane orientation as their neighbors (within about 5°rotation around the c-axis), but also many show a maximal rotation with respect of some of their neighbors (a rotation by 30°between $[10\bar{1}0]$ and $[11\bar{2}0]$ directions). It looks as if abnormal grains nucleate between grains with a large mismatch. The spatial resolution of the EDAX technique does not allow for a precise determination of the Sc concentration in grain boundaries. Taking a 43% Sc film as an example, the relative increase of Sc concentration in a 5 nm wide boundary zone was measured as 8 at.%. Stipulating that the grain boundary is in fact only 2-3 atomic layers wide, a Sc concentration of far higher values is obtained. Therefore, the complexion layer can be considered as an epi-layer with a composition close to ScN. Such a situation can explain the possibility of rocksalt nucleation. The nucleation of the rocksalt phase can also be promoted by the

very good matching of the basal N-N or Sc(Al)-Sc(Al) distance in the wurtzite (lattice constant $a = 3.2\mathring{A}$ for 17% Sc) and the corresponding distances in the rocksalt structure (half of face diagonal (3.18 $\mathring{A}$)). An atomistic view is given in Figur2.29.a. The tetrahedral coordination of the wurtzite phase would abruptly change to an octahedral one of the rocksalt structure. While the in-plane matching is perfect, the out of plane match is less perfect, and may give rise to a tilt of the octahedrons. The rocksalt phase cannot grow to large grains, as there is too much Al in the average composition. Hence the phase reverts to the wurtzite, for instance by putting the c-axis along the 3-fold axis ($\langle 111 \rangle$) of the rocksalt phase, thus growing a tetrahedron out of an octahedron facet. In the ideal case as drawn in Figure 2.29).a, the new polar direction would then be tilted by 55° from the original one. The c-axis of the AOGs are thus significantly tilted with respect to the c-textured grains. In this process, the orientation of the new c-axis of AOG tilts significantly with respect to the c-textured grains. In our results, we show that the growth of the AOGs is faster than that of the c-textured grains. This is explained by the faster growth at edges and tips of the AOG crystallite. A similar situation was described by Mahieu et al. [143]. The fast edge growth, combined with high mobility on the low surface energy facets, leads to well-formed facetted growth even in the zone-T growth mode. It is thus the combination of faster chemisorption at edges, and fast step growth on the adjacent facets, which leads to the observed habit (Figure 2.29).b. Typically, three facets are observed: two low energy, smooth $11\bar{2}0$ facets, together with the rougher (0001) facet (see more of such grains in Figure 2.28).

(0001) facets are rougher as the ad-atom mobility must be lower there. As a final reason for why abnormal grains are the dominant morphology with increasing film thickness, is the fact that they obtain a higher flux from the gas phase than the lower lying (0001)-textured film surface, as they capture better atoms and molecules that arrive under grazing angles.

Our results show that Sc-segregation at the grain boundaries is as much influenced by the growth conditions of the GBs, as it is by the Sc content in the film. Nonetheless, in the case of well (0001)-textured films (as shown in Figure 2.18), the increase of Sc concentration is followed by an increased nucleation rate of AOGs. AOG growth leads to the formation of large angle grain boundaries, which in turn leads to larger Sc segregation at such GBs. The development of a Sc-rich complexion phase at GBs in AlScN (27% Sc) films due to annealing induced segregation may result in the increase of dielectric losses observed by Mayrhofer [146]. The observed decrease of the piezoelectric coefficients $e_{31,f}$ and $d_{33,f}$ [6,129] with increased density of AOGs is simply due to the loss of (0001) film orientation. The observation that substrate temperatures below 300° C produce AlScN films having less losses [132] could explain the fact that the higher temperature will promote segregation of Sc

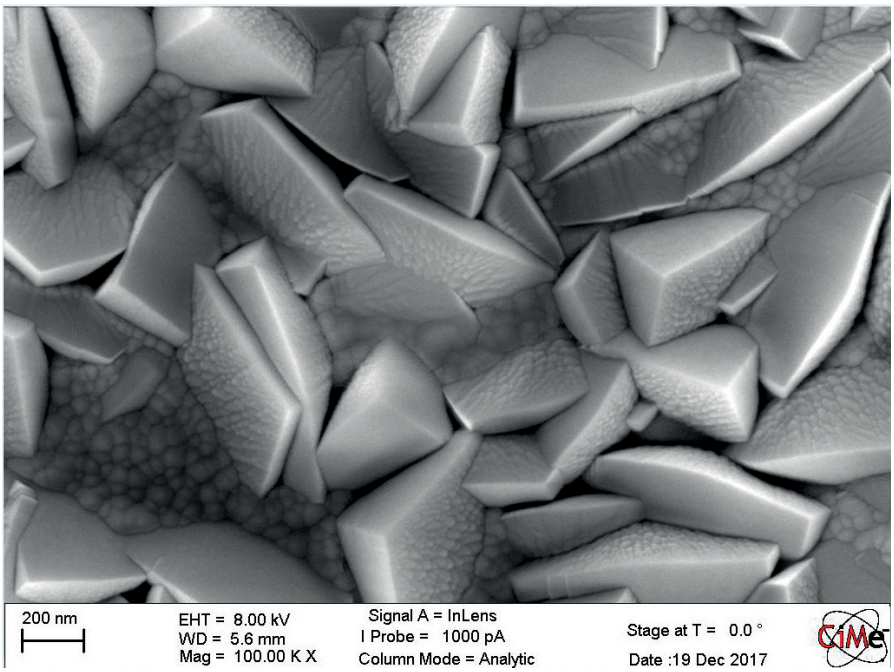

Figure 2.28: SEM image of a 2 μm thick AlScN 16% Sc film. This figure evidences better the pyramidal shape of the AOGs. They exhibit two smooth facets and a rough one (c-plane).

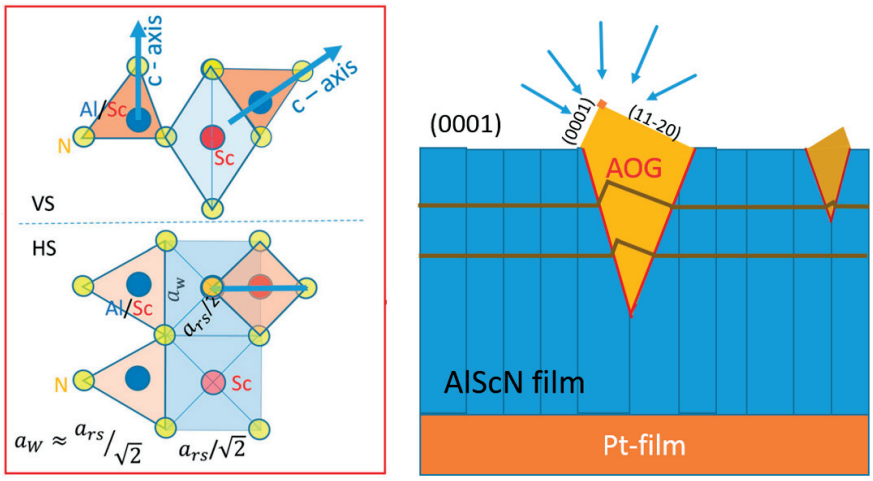

Figure 2.29: Sketch of the growth of AOGs in AlScN thin films. The incoming atom fluxes are indicated by blue arrows. The edges and the top corner of the AOG receive the highest fluxes.

at the GBs, because of the higher mobility of the ad-atoms. Diffusion activation by ion impact combined with sufficiently low energetic barriers at grain boundaries are essential to obtain a sufficient surface diffusion across grain boundaries in order to create and maintain a uniform and compact c-axis texture of the wurtzite structure. Higher ion fluxes, higher ion energies (up to a certain limit), lower substrate roughness, and less shadowing effects by more directional fluxes [129] work to prevent Sc accumulation and the formation of Sc-rich complexions at the grain boundaries. The impact of the Ar/N ratio, on the incidence of AOGs as reported in ref [129] , shows the sensitivity of the Sc segregation with respect to ion bombardment conditions during the film growth (an example of texture sensitivity to ion bombardment is shown in Figure 2.30). Epitaxial stabilization helps as well to obtain wurtzite AlScN thin films in extended process window, so for instance a 40 at. % Sc film grown at higher temperatures of 500°C-700°C [124].

Conclusions

The presence of the AOG in AlScN films leads to a partial or total loss of the c-axis texture in the surface layer of the films. Many of the AOGs have c-axis tilts of 50°to 90°. They nucleate during the growth at grain boundaries between the (0001)-oriented grains, which dominate growth initially. Hyper-Map EDX studies allowed us to prove a segregation of the Sc at grain boundaries between such grains, at least in some cases, with an indication that this concentration is higher when the relative in-plane mismatch between neighboring grains is larger. It is plausible that larger Sc concentrations may lead to the nucleation of the cubic rocksalt structure akin to a complexion phase. As such embryonic nuclei cannot persist to stay in the rocksalt structure when approaching the average composition at a larger grain size, they revert to the wurtzite phase. This mechanism leads to a loss of the original orientation. It even appears that a large tilt of the c-axis away from the vertical direction, is more favorable. AOGs grow faster than the c-oriented grains. The proposed growth mechanism to break the overall (0001)-texture considers the formation of a rocksalt nucleus in the Sc-rich complexion present at the grain interface between normal grains. In summary the AOG growth mechanism consists of four consecutive steps:

1. Sc accumulation between grains with a bad match of in-plane orientation.
2. Formation of a rocksalt complexion layer with a Sc rich composition.
3. Secondary nucleation and growth of wurtzite AOGs from the complexion interface

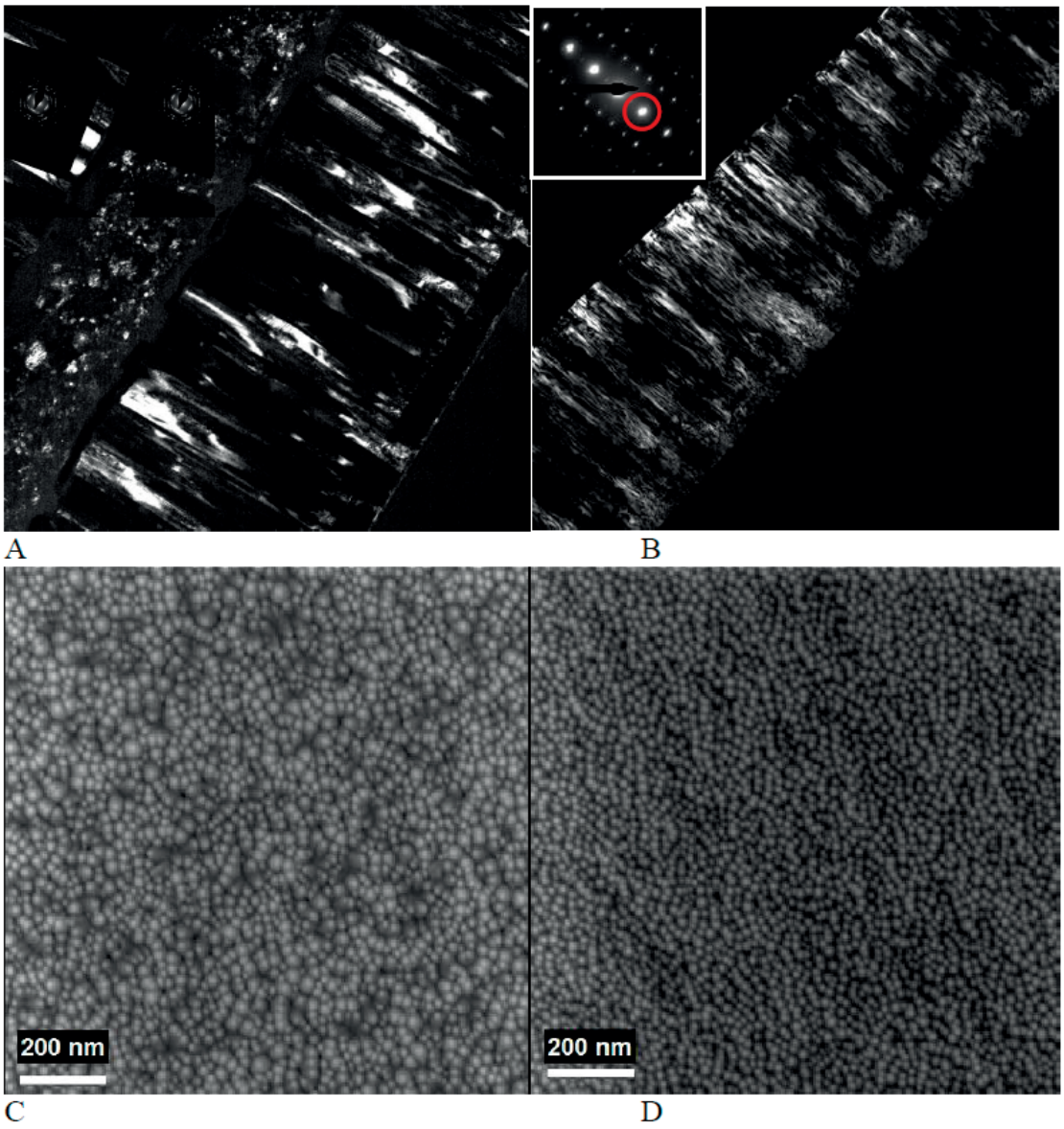

Figure 2.30: Dark Field TEM and SEM images of AlScN 10% (A) and (C) originate from the center region; (B) and (D) from the border region of a 6-inch wafer. Figure 2.26.a in the paper corresponds to the center region (A, C). The slight changes in growth conditions, as induced by a difference in the directionality of atomic fluxes and changes in ion bombardment intensity, strongly affect the film microstructure in terms of the lateral size of the columns and the perfection of c-texture.

4. Faster growth of AOGs because they obtain a higher incoming flux.

The conversion of the planar complexion into a vertical one at high-energy grain boundaries is at the origin of AOG growth mechanism: the Sc enriched surface layer created by preferential absorption of Al in the wurtzite phase generates at their side walls Sc-rich complexions in rocksalt phase which constitute the nuclei for AOGs. We also showed the importance of the material density and the roughness at grain boundaries. Smoother films with more coherent grain boundaries leave no space for impurity attachment and do not lead to AOGs, whereas badly matched, open grain boundaries promote Sc segregation and the nucleation of AOGs.

Chapter 3

Microfabrication

3.1 Process Flow Overview

Several types of piezoelectric resonators have been fabricated in this work, including thickness extensional mode resonator (TEMR), length-extensional mode resonator (LEMR), radius-extensional mode resonator (REMR), and Lamb wave resonator (LWR). TEMR, LEMR, and REMR are known as shape resonators which are employed to extract material parameters (Chapter 4). The microfabrication process for shape resonators has more steps and consequently more challenges than LWRs microfabrication. Therefore, in this chapter we focus on the microfabrication process for the shape resonators. Meanwhile, the remarks of LWRs fabrication process will be explained in the relevant fabrication steps. Firstly, we pass through the overall process, then we will explain the challenges associated with different steps.

Figure 3.1 represents schematically the employed process flow applied on a 100 mm diameter silicon wafer for shape resonators fabrication.

1. The process started with a double side polished 380 μm thick Si wafer as the substrate.

2. 200 nm SiO_2 was grown as an insulator layer by wet oxidation method on the silicon wafer to reduce electrical leakage to the Si substrate. 200 nm low-stress Si_3N_4 layer was deposited by LPCVD on the oxide layer in order to compensate the compressive stress of the oxide. This step is crucial to prevent cracking of the anchors (bridges) during the later releasing step. Both dielectric buffer layers together are also important for reduction of the parasitic capacitances and losses between the contact pads since silicon forms a lossy conductor [147, 148].

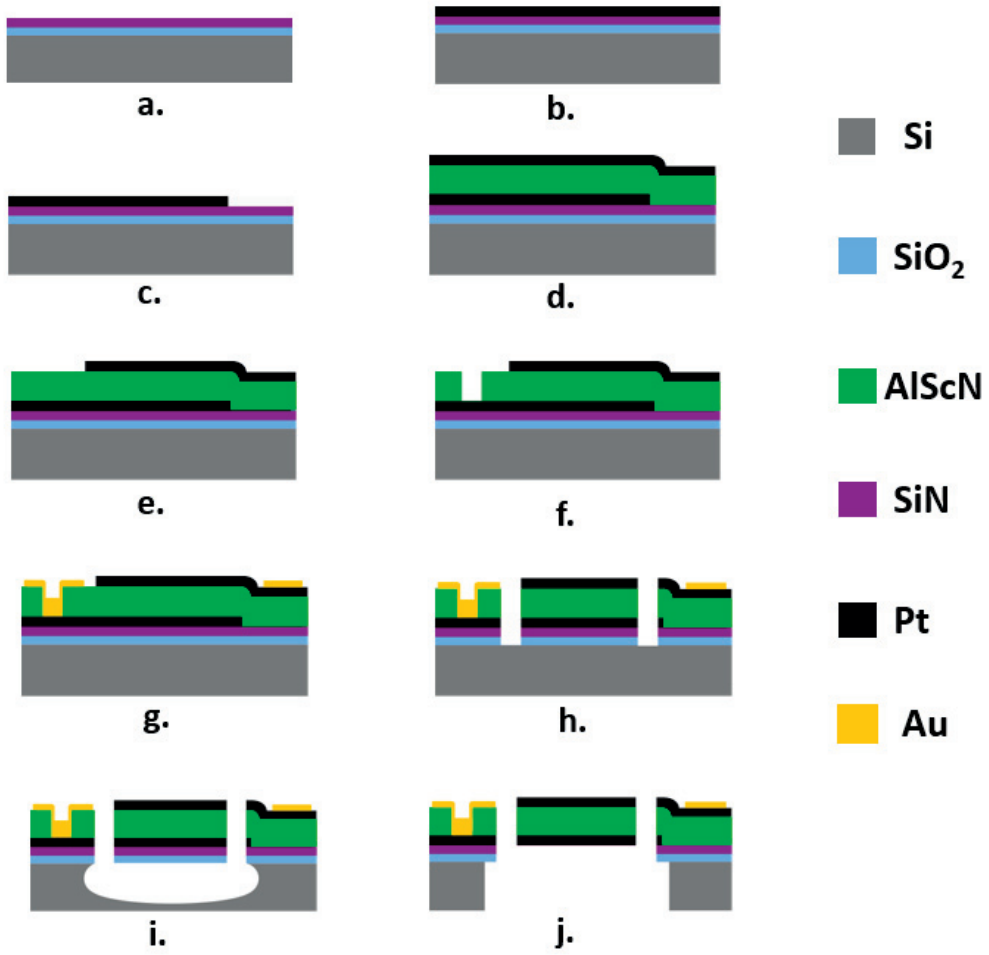

Figure 3.1: Schematic view of the process flow used to fabricate shape and LWR resonators with AlScN piezoelectric thin film. (a) Oxide and nitride layers deposition on the Si substrate. (b) Pt, BE deposition. (c) BE pattering by IBE. (d) AlScN and TE deposited on patterned Pt bottom electrode. (e) Pt, TE patterning by IBE. (f) open via access to the bottom electrode by wet etching. (g) Deposition Cr/Au layer on contact pads. (h) Define the prime of resonators by IBE. (i) Top side liberation of devices from the Si substrate by dry etching. (j) In LWRs instead of top side liberation, Bosch process is employed for deep anisotropic etching of Si substrate from the backside. Oxide and nitride layers are etched away later by Cl_2 chemistry dry etching.

3. 200 *nm* Pt was sputtered at 350℃ as the bottom electrode (BE).

4. Ion beam etcher (IBE) used to pattern the BE (1^{st} mask.)

5. 1.2 μm $Al_{0.85}Sc_{0.15}N$ was deposited by pulsed DC reactive magnetron sputtering process on the patterned Pt (111) bottom electrode. Detailed conditions of sputtering are explained in Section 2.4.

6. 200 *nm* Pt sputtered at 350℃ on the AlScN thin film as the top electrode (TE).

7. The top electrode Pt patterned by IBE (2^{nd} mask).

8. Hot phosphoric acid at 130℃ (H_3PO_4, 85% volume) was used to remove the AlScN film for opening an access to the bottom electrode (3^{rd} mask).

9. A contact metallization of 200 nm Au on 30 nm Cr was selectively deposited by sputter deposition combined with a lift-off process using a LOR resist. This improves electrical connection of pads with tips as well as the mechanical durability of the tips (4^{th} mask).

10. The in-plane dimensions of the resonators were defined by pulse IBE of the all layers from the top electrode to the Si substrate. ($AlScN/SiO_2/Si_3N_4$) using photoresist (PR) as the mask (5^{th} mask). The selectivity between PR and AlScN during the IBE process is about 1:2. Dry etching of AlScN film by IBE shows promising results, while the chemical dry etching by Cl_2 chemistry which is a standard method for etching AlN films, is not efficient for AlScN film. As Sc doping increases the chemical resistivity of AlN and reduces the selectivity by a factor of 2.

11. For the shape resonators, the devices were released from Si substrate by top side isotropic dry etching of Si in SF_6, which was the last fabrication step for the shape resonators .

12. For Lamb wave resonators 2μm Parylene was coated on the topside of the wafer for protection during backside etching.

13. LWRs released from Si substrate by backside anisotropic etching of silicon by SF_6 (Bosch Process) (6^{th} mask).

14. SiO_2 and Si_3N_4 layers were etched away by dry etching in CF_4 (step *j*).

3.2 Microfabrication Challenges

In this section we present the microfabrication challenges we faced during the mentioned processes in addition to the solutions we developed to address them.

3.2.1 IBE

In several steps, including TE etching and defining the in-plane dimension of the device, IBE was employed as the etching tool. Photoresist (PR) was the mask material in all the IBE processes which shows the selectivity of 2:1 in AlN etching. The burning of the PR was the first challenge we faced in the IBE process. Figure 3.2 shows the 4μm PR which exposed for 40 minutes to the IBE, PR was burned, and remover solution could not strip it. The picture was taken after one hour immersion in a hot (75°C) PR remover. Cooling of the wafer in microfabrication tools is usually

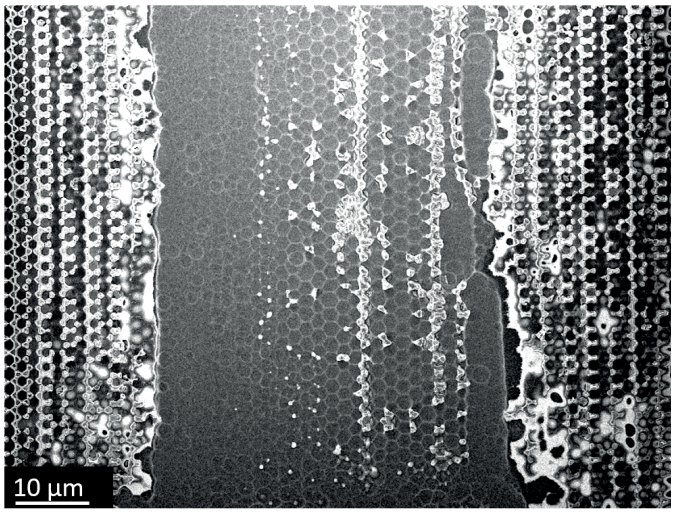

Figure 3.2: PR burning during IBE. Stripping of burned PR could be impossible. The picture was taken after one hour immersion in a hot PR remover. Initial thickness was 4μm and IBE process longed 40 minutes. The goal was etching a dense network of 2μm (diameter) holes in 1μum thick AlN thin film. A successful version of such structure is shown in Figure 3.6.

done by circulation of water or a cooling gas through the substrate holder. It means that the PR gets cool through the wafer. However, as photoresists are not good heat conductors their surface are not always cooled down efficiently. Increasing of PR thickness intensifies this issue. Thus, the PR thickness must be as thin as possible. When it is needed to use a thick PR due to process requirements (e.g.

more than 2μm), long baking of PR(e.g., 12 hours at 85°C) can reduce the risk of burning. In addition to baking, using the IBE in the pulsed form (t seconds etching, t' seconds waiting) can improve the process yield significantly. The principle of employing the pulsed-IBE technique is not letting the PR to reach to the burning point. That is the recipe we developed and used in step 10, where we needed to etch all the stack from the TE to the Si substrate level by IBE and employing 4-5 μm of PR as the mask.

Huge PR lateral etching is the other challenge in the IBE process. This caused losing the top electrode connection in REMR and TEMR fabrication (Figure 3.3) during top electrode patterning by IBE, despite having enough thick photoresist.

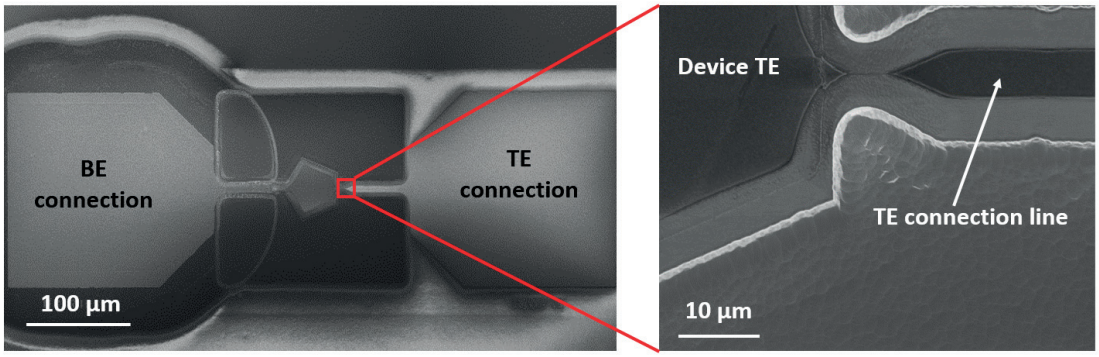

Figure 3.3: SEM image of TEMR. Lateral etching of photoresist leads to it's fast removal and exposure of the connection line to the etching ions. This resulted in top electrode connection loss.

This issue rises and gets crucial in structures with a high aspect ratio (depth of etching/opening diameter), where the critical lateral dimension is in the order of the etch depth. We intended to fabricate an array of holes (diameter 2μm) through a 1 μm thick AlN film deposited on 100nm thick Pt bottom electrode on top of a 200nm SiO_2 over a Si substrate. The distance between two neighboring holes was 2 μm. Considering the etching rates of AlN and PR by IBE, which are around 25 and 50 nm/min, respectively; 2 μm thick PR must be enough to protect the pattern during the IBE process. Despite these calculations, huge over etching up to the silicon level was observed after 40 minutes of etching, as shown in Figure 3.4. This phenomenon could be explained by lateral etching of the PR. The lateral etching arises due to the fact that the ions do not arrive perpendicular to the surface, but with a tilt of 15°. This tilt is applied to avoid shadowing effects below the PR edges. But it also leads to removal and rounding of the edges. PR re-flow which must be done to reduce fencing effect, is the next reason which makes the PR edges rounded. Once the impact angle of the ions to the rounded edges of PR approaches

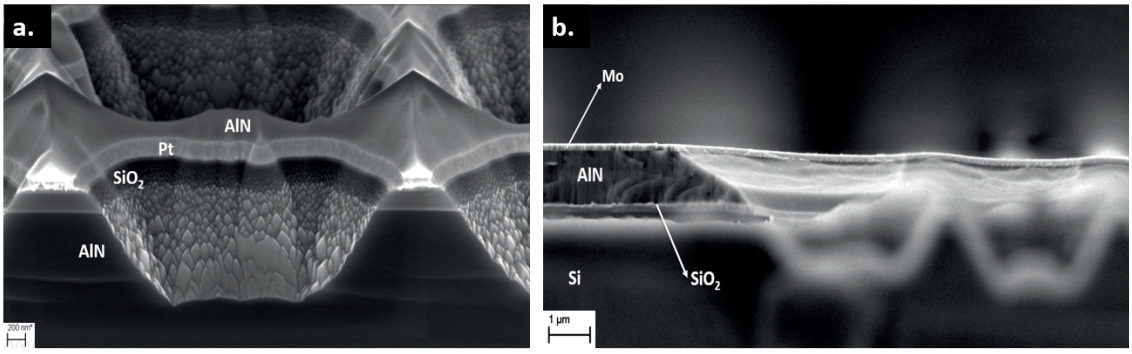

Figure 3.4: Cross section SEM image after 40 minutes IBE, initial PR thickness was $2\mu m$. The goal was etching a dense network of 2μum(diameter) holes in 1μum thick AlN thin film. (a.) Pattern region which is over-etched up to Si level. (b.) The interface of pattern and non-patterned region. This shows in non-patterned region where the lateral etching does not take place the PR remain up to end of IBE and protect the underneath layers.

to the 40°to 50°, the etching rate becomes about twice of a perpendicular incidence (Figure 3.5.a). Thus, the width of PR in the holes region is reduced almost four

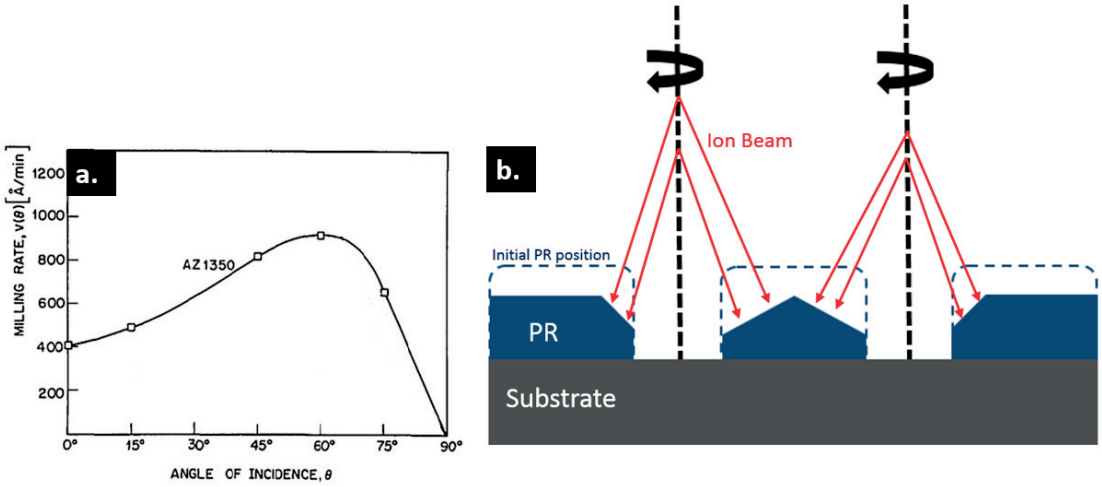

Figure 3.5: (a.) PR etch rate as a function of ions incident angle [149]. (b.) Schematic view of PR lateral etching in the structure with a high aspect ratio.

times faster than it's thickness. Figure 3.5.b illustrate this effect. This is why the PR does not survive until the end of the etch process. In the non-patterned regions the rounded edges are not exist, thus no lateral etching takes place and the PR survives until the end of the etching process and protects the bottom layers

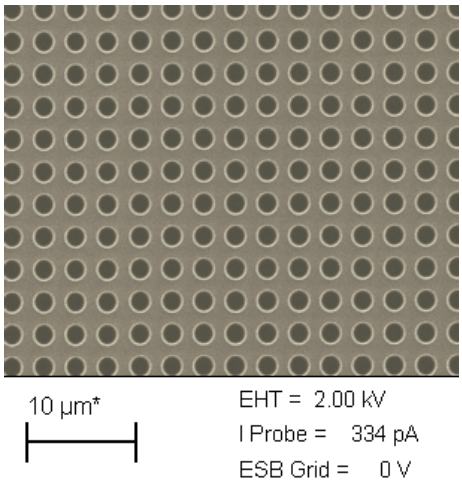

Figure 3.6: Top view SEM image of a dense network of holes ($2\mu m$ diameter) in a $1\mu m$ thick AlN. PR thickness was $3\mu m$ and IBE stopped by detecting *Pt* signal (BE) in the endpoint detection system.

(Figure 3.4.b).

To solve this problem we skipped the PR re-flow step before the IBE. We also apply no tilt to the substrate holder during the process. By these we tried to insure a perpendicular incident angle of the ions arriving on the PR surface. Furthermore, some big windows added to the design in order to enhance *Pt*, BE, signal in the end-point detection system of IBE. Figure 3.6 shows a top view SEM image of the IB etched structure after these modifications. As it is seen, the lateral etching issue did not take place and thanks to the big opened windows, over etching was also prevented. Since the etch process was stopped by detecting the *Pt* signal at the endpoint detection system. However, due to the different in the openings size, the etch rate in the relatively bigger opened windows is not the same as the etch rate in the patterned area. While the etch reached to *Pt*, BE, in big windows, it is still in *AlN* level in the patterned region. As depicted in Figure 3.7. Therefore, the etching time must be optimized individually based on the pattern structure.

Significant redeposition of the etching material, *AlN*, on the PR edges was the next challenge (Figure 3.8a). Several methods including re-flowing the PR before IBE in order to round the sharp edges, ultrasound bath, mechanical polishing and high-tilted angle IBE were tried to avoid/ eliminate the fences. High tilted IBE after resist stripping looks the most promising one to remove the fences (Figure 3.8b). The only disadvantage of this method is that the ions attack the top electrode as well as the fences. Therefore, the initial thickness of the top electrode must be modified accordingly.

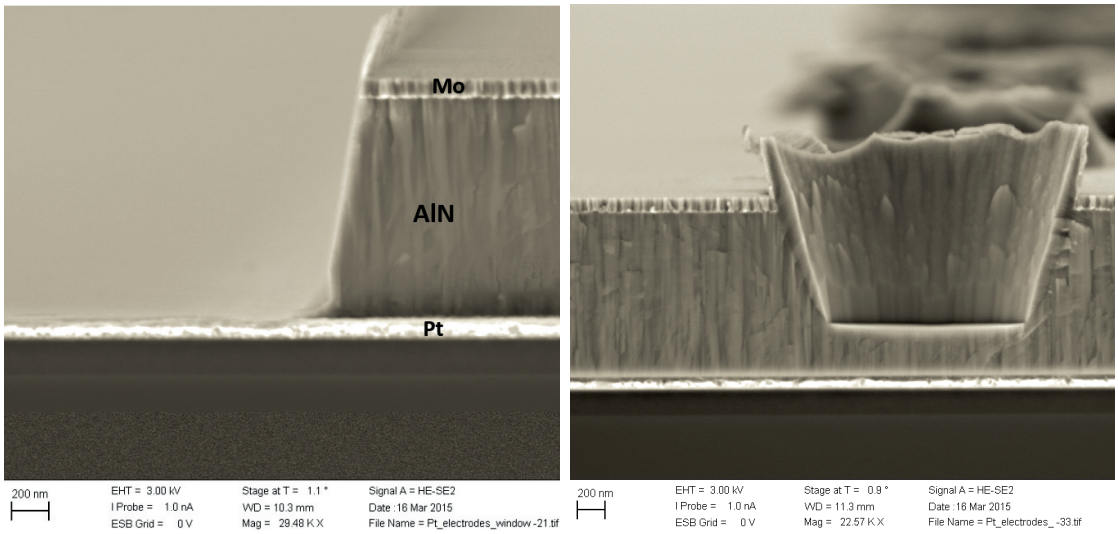

(a) (b)

Figure 3.7: Cross sectional SEM image after 50 minutes IBE shows that IBE etch rate depends on the opening size. The etch stopped by detecting the *Pt* signal. Images are different regions of a same wafer. Initial PR thickness was $3\mu m$. (a.) Relatively big opened windows to intensify BE signal in endpoint detection system. (b.) A 2 μm diameter hole in the pattern region.

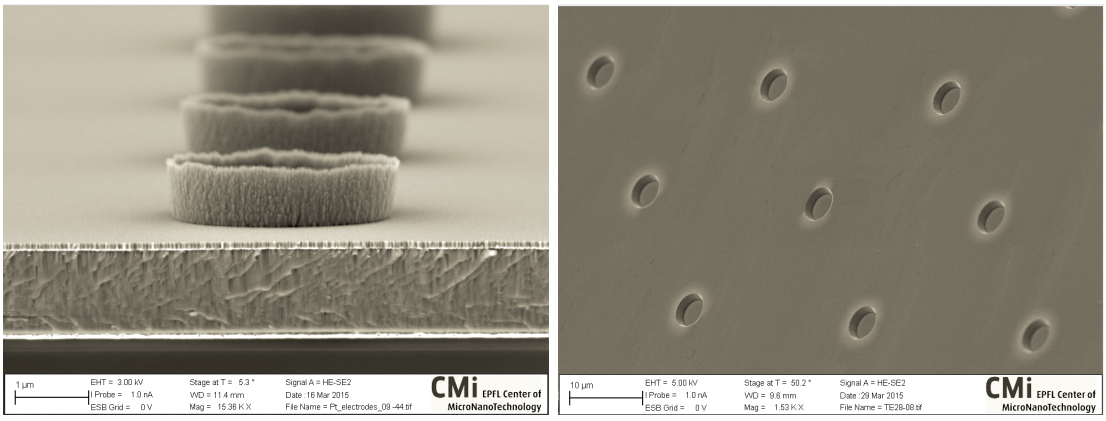

(a) (b)

Figure 3.8: Redeposition of the etched material on the PR edges produces huge fences. (a) SEM image after 40 minutes IBE process. (b) After removing fences using high angle IBE (75° tilted stage) for 4 minutes.

3.2.2 AlScN Thin Film Deposition on Patterned BE

Patterning of the BE has a significant effect on the microstructure and piezoelectric properties of deposited AlScN film, through promoting ab-normal grains growth. We already discussed the abnormal grain nucleation and growth in Chapter 2. These grains enhance the roughness of the film and reduce the piezoelectric activity. They degrade the electromechanical coupling coefficient and the quality factor. In surface acoustic wave devices, rough surfaces lead to wave attenuation and wave scattering. In this section we will describe how we attempted to prevent/minimize the growth of such grains.

Figure 3.9 shows SEM pictures and XRD patterns for 1μm thick AlScN films, sputtered with the parameters as Table 2.2, but with a different situation regarding the BE patterning. The excellent c-textured film with a dense fibrous structure obtained when the wafer was entirely covered with the BE (100nm Pt). However, in most of the piezoelectric MEMS devices, one needs to pattern the BE and keep it just on the active part of the device, as we did on the 4$^{\text{th}}$ step of our process flow (Figure 3.1.c). In our first approach, we pattern the BE in a way that it remained only on the required positions to serve BE for devices. Practically, islands of less than square millimeter of isolated Pt were kept. For instance, in one of our designs we had 150 devices distributed on a 4 inches wafer. Each device has less than 0.2 mm^2 BE. Thus, total surface area covered by BE after patterning was 30 mm^2, which almost equals to 0.4% of the total wafer surface. XRD pattern and SEM image of such a film is presented in the middle raw of the Figure 3.9. The surface is fully covered by abnormal grains and film is not anymore fully c-textured . The drop of the (0004) peak intensity is a good indicator which can show the difference of the films texture. Consequently, devices performance of such film were significantly lower than expected.

To solve this challenge, we changed our approach regarding the BE patterning. In the new approach, we keep the BE everywhere except the places it must be removed to prevent unwanted modes excitation (e.g. below the TE connection lines, to prevent unwanted BAW) and also prevent shorting of devices. By this technique, BE was left on more than 98% of the wafer surface. XRD pattern and SEM image of such a film is shown in bottom raw of the Figure 3.9. It is seen that the film is almost fully c-textured (a small peak of (103) is seen), and the surface is not anymore fully covered by abnormal gains, and dense fibrous structure of the perfect film is seen below few abnormal grains. Devices of this wafer showed an acceptable performance close to what expected from a device with an ideal film.

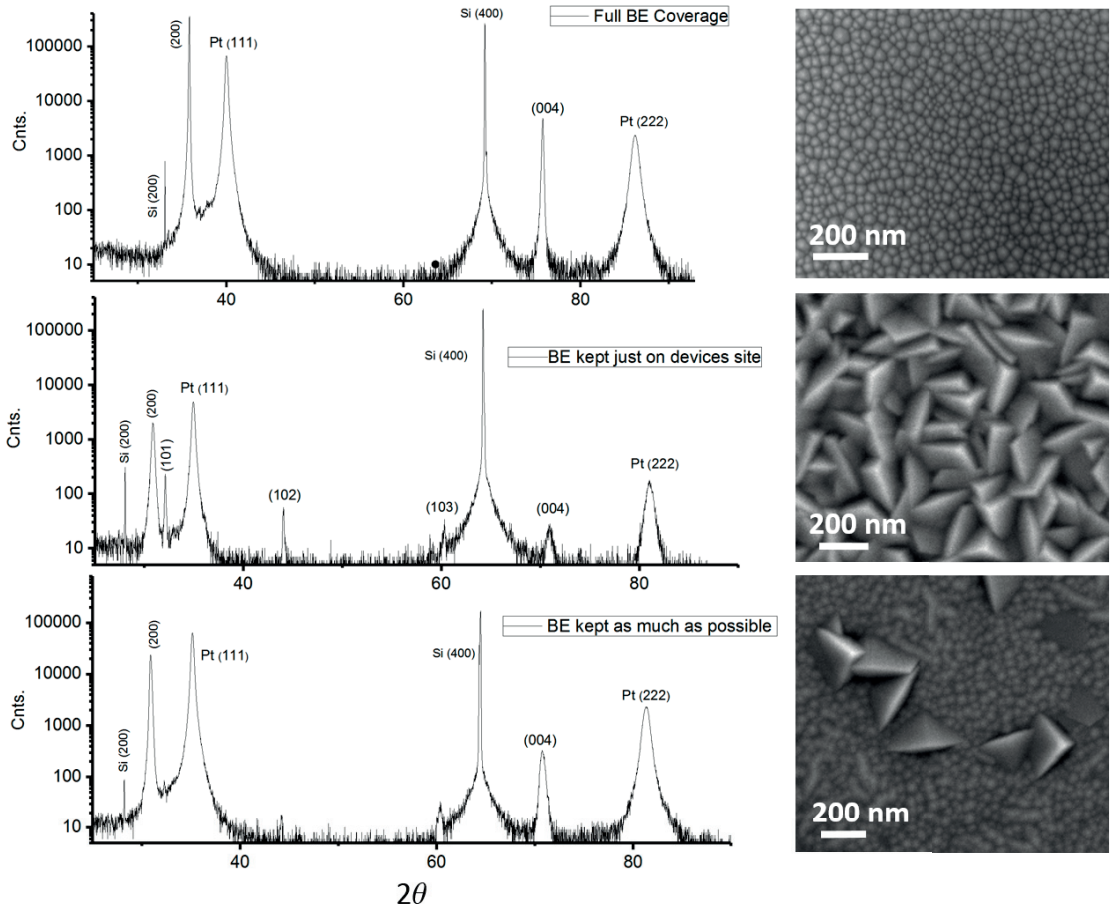

Figure 3.9: BE coverage effect on AlScN films texture and morphology. Top raw shows AlScN film sputtered on a wafer fully covered with Pt as the BE. In the middle raw the BE was patterned and less than 1% of the surface has Pt. In the bottom raw, BE was patterned but it still covers 98% of the wafer surface. All the XRD patterns are obtained from a spot with BE in the center of the wafers.

3.2.3 Interdigitated Electrodes

The phase velocities and consequently the operation frequency in Lamb wave modes is a dispersion function of film thickness over the wavelength. The wavelength is defined by the width of the Interdigitated fingers as SAW devices. Due to the design requirements which are explained in Chapter5, we needed to fabricate up to 300 IDTs with the width of 1.25μm ($\lambda = 5\mu m$). This critical dimension is close to the nominal resolution of our photolithography setup. Fingers length are defined as $30\lambda = 150\mu$m. Photolithography of such a long, narrow and dense structure of fingers could be quite challenging since the PR adhere to the surface in a relatively

small surface while it has an elongated sidewalls fronting the developer solution. As a result of this situation, PR is washed away during the developing. Figure 3.10 shows an optical image of IDTs after developing. Two issues are observable: Fingers are either detached from the connection line (busbar) or in case that they have not lost the connection from busbar, they were detached from the surfaces. To

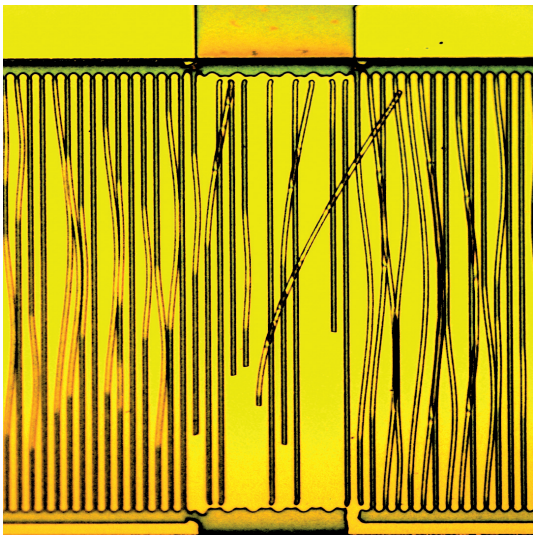

Figure 3.10: IDTs detached from busbars and also from the AlScN surface during development due to the weak adhesion to the AlScN surface.

relax these issues, we added fillets of PR in connection points of fingers to busbars in the design. Furthermore, we underexposed the PR during UV exposure step of photolithography. This leads to the under-development of the exposed regions (patterned) of PR; therefore a tiny layer of PR remains on the part of the design which is supposed to be depleted from PR. This gives integrity to the PR on the patterned and non-patterned surface. This tiny part will be etched during the etching step. This extra required etching must be considered in etching time and also PR thickness calculations. Applying these modifications resulted in successful photolithography and etching of IDT fingers as shown in Figure 3.14.

3.2.4 Opening Access to the BE through the AlScN Film

To characterize shape resonators, BE must be accessible. To do so, we needed to etch 1 to 2 μm (depending on the device design) thick AlScN thin film and stop on BE (Figure 3.1.b). At the first try, we used IBE. The fencing and PR burning issues were solved as described in the previous section. However, stopping the IB etch on BE before over etching of it, which leads to connection loss, was the IBE

challenge for this step. Since the size of the BE-openings ($200\mu m \times 200\mu m$) is almost negligible in the wafer area scale, no Pt (the BE) signal was detectable by the endpoint detection system. Putting some big openings in the design to monitor Pt signal was not an efficient reference in this step due to the dependency of the etch rate to opening size, as presented in Figure 3.7.

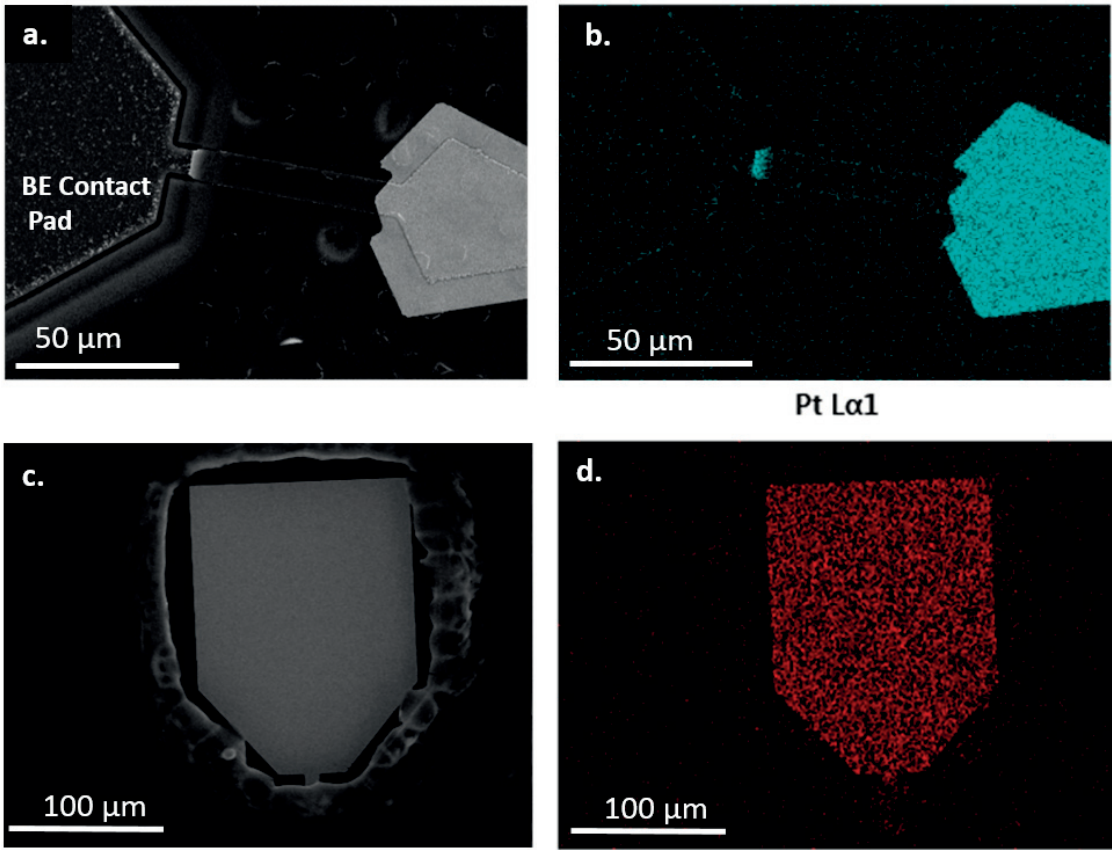

Figure 3.11: Top view SEM images of the openings in AlScN film to access the BE. (a.) AlScN etched by IBE. (b.) Pt-EDX map of the image (a.) shows that the BE was etched away by IBE, while on device site the Pt of the TE is clearly observed. (c.)AlScN etched away by hot phosphoric acid. (d.) Pt-EDX map of the image (c.) shows that the etch stopped successfully on Pt, BE.

Wet etching of AlScN was the next option. Hot phosphoric acid (70°C-90°C) is a standard enchant for AlN thin film [150, 151], but these temperatures do not work for AlScN. It seems that Sc content increases corrosion resistivity of AlN. More than one hour of etching was needed to etch 2μm AlScN with phosphoric acid (85% volume) at 70°C. We have increased the temperature to 130°C, which resulted in a fast etch rate around 500 nm/min. Two points must be considered for

a successful wet etching with such a hot phosphoric acid: *I.* Phosphoric acid at this temperature is quite aggressive. Long baking of PR (e.g. overnight) is essential to avoid PR burning. *II.* The acid etches the AlScN almost isotropically, so the lateral under-etch must be considered in the design. The opened via to access the BE must have enough distance from anchors. Otherwise, the film will be etched away underneath the anchors which practically leads to the loss of the anchor. Figure 3.11 shows the result of IBE and wet etching of AlScN to open access to the BE.

3.2.5 Devices Release

Device liberation from the Si substrate was the last step of fabrication. Several issues must be taken into account to perform this step successfully. Backside etching of the Si substrate with the conventional Bosch process was employed to liberate the shape resonators as well as the lamb wave resonators from the Si substrate. One must consider that the Si etch rate in the Bosch process is a function of opening (surface) size, since the plasma accesses to the Si surface through the opening and in continue evacuation of the etched Si particles also takes place through the opening. Therefore, devices with a significant difference in opening size cannot be liberated together. In this case, the bigger devices are getting open, while the small ones still have plenty of Si (Figure 3.12.a and b). Continuing the etching process to liberate all devices results in breaking of devices which have been liberated earlier. Figure 3.12.c and d.

Based on this experience, we separated devices according to their opening size. The lamb wave resonators which has the relatively big opening area e.g. 300μm $\times$400μm were liberated with the Bosch process. The advantage of this approach is the plasma has direct access to the backside of the device. Therefore, when the Si is etched away, the oxide and nitride layers can be etched as well with Cl_2 chemistry (in another tool). Figure 3.14 shows the lamb wave resonator which is liberated from Si, SiO_2 and Si_3N_4 layers by the described method.

Device with smaller opening size was liberated from the Si substrate by isotropically etching of Si from the topside, as depicted in the process flow (Figure 3.1.i). Anchors which were usually broken during backside Bosch process opening were survived with this technique. Despite the Bosch process which is a standard method for deep Si etching and details are well known (e.g., etch rate, opening size effect aspect ratio effect), topside isotropic etching of the Si substrate is a recent approach. M.Rinaldi already used XeF_2 for this purpose [46], but our etching tool works based on fluorine and chlorine dry etch chemistry. Therefore, we needed to investigate how big the opening must be, and how long we need to etch to perform a successful

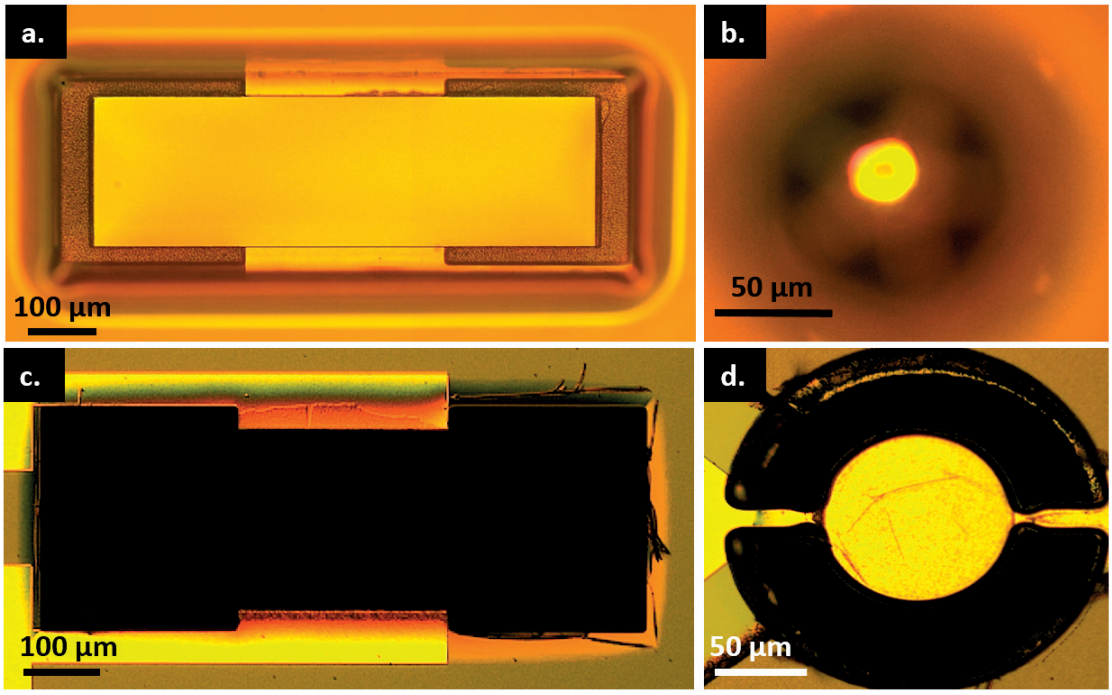

Figure 3.12: Optical images of devices back sides (a. and b.) and front sides (c. and d.) during the Bosch process. Si etch rate in the Bosch process is affected by opening size. Lamb wave devices which have a bigger opening (a) opened faster than the smaller device like REMR (b). Continuing the etching process in order to liberate small devices (d), resulted in breaking of the devices which had been liberated earlier (c).

liberation. We also need to know the etch rate to make the design in a way that enables us to liberate the active area of the device without digging underneath of the connection line and pads. To have such design we need to know the exact etch rate of the Si, then make the opening (area exposing to the plasma) in a proper distance from the device and from the connection lines and pads. To answer these questions, we first applied the etch process on a dummy wafer with real designs of the shape resonators, then we made FIB cut in the etch profile to see the etch rate and quality.(Figure 3.13). SEM images showed that 49μm lateral etch took place in 30 minutes, which gives a lateral etch rate of 1.63 μm/s.

The disadvantage of this method (top side liberation) is that there is no direct access of plasma to the oxide and nitride layer below the bottom electrode. Thus, it is almost impossible to remove these layers which act as a mass loading on resonators and must be considered in resonance frequency calculations and modelings. It also affects the device performance due to the leakage of the sound wave from BE to

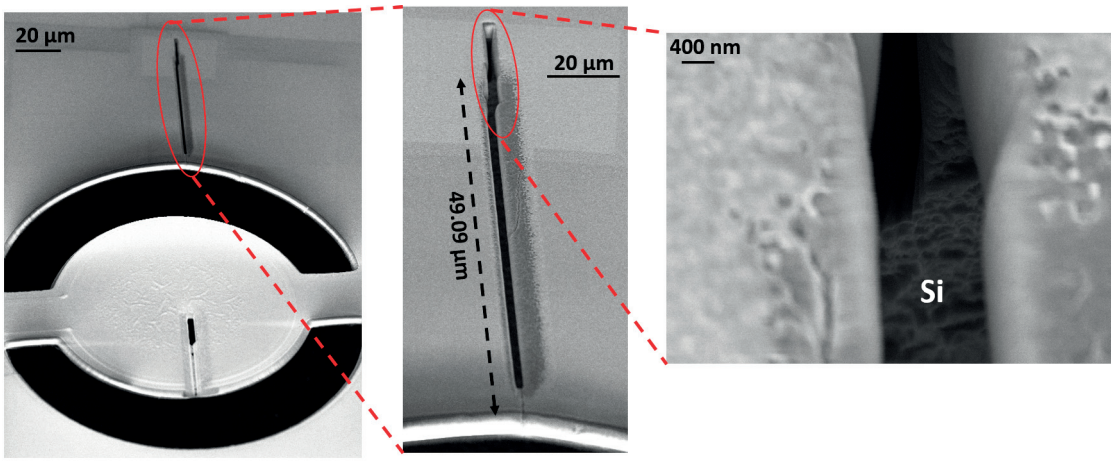

Figure 3.13: FIB study on dummy wafer to investigate Si etch rate in topside liberation process. The device exposed to the SF_6 plasma for 30 minutes. SEM image shows that the Si etched away 49 μm far from the opening.

these layers.

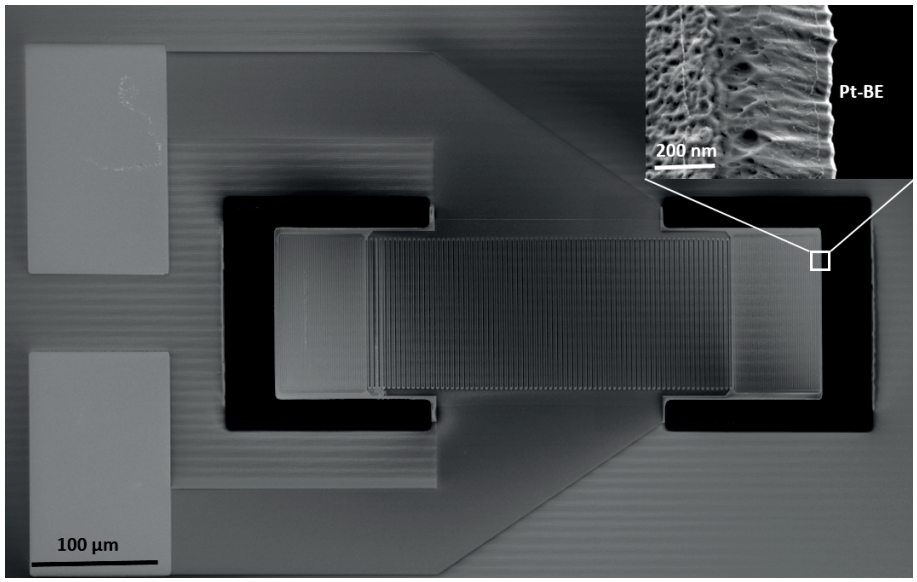

Figure 3.14: Lamb wave resonator released from the substrate by the Bosch process. The oxide and nitride layers below the Si layer were etched away by Cl_2 dry etching. Membrane is fully released up to the level of bottom electrode Pt.

3.2.6 Stress Control

Two types of cracking were observed in membranes during liberation (from the Si substrate) process. Both employed liberation technique, Bosch process and topside isotropic etching of Si, were identical regarding the cracks initiation. The first type of crack was generated from sharp edges of designs (sharp corners) in the liberation masks. As it can be seen in Figure 3.15. We managed to solve this issue by rounding the sharp edges and give them at least a radius of 20μm. The second types of cracks took place at the border of BE. Patterning of the Pt bottom electrode is needed to define the resonator active area, as depicted in process flow in Figure 3.1.c. It means that the AlScN was afterwards deposited on a stepped surface which had islands of Pt (111) and the rest was covered by SiO_2 which was already roughened by IBE (because of the above Pt layer patterned by IBE). Beside the roughness of the steps borders which can induce a crack in the AlScN

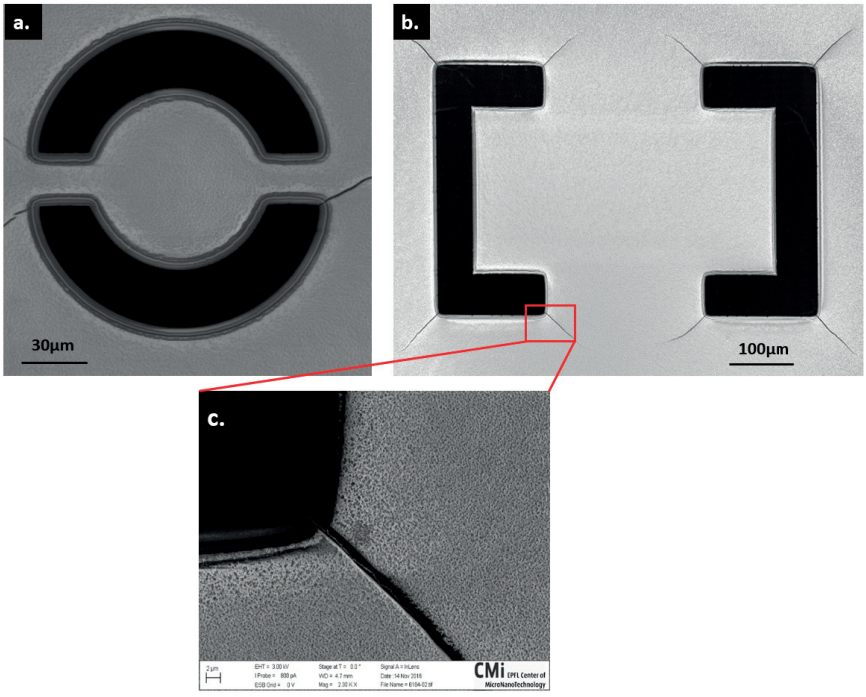

Figure 3.15: Cracks generated from sharp corners during the liberation process. (a.) REM. (b.) LWRs frame. (c.) Magnified sharp corner

thin film due to the height difference, it is a significant stress gradient between the AlScN film grown on the Pt layer and the film grown on the oxide layer [152]. The 1.2μm thick AlScN film on Pt (111) exhibits stresses up to 200 MPa, and on oxide layer up to -200 MPa. Therefore, AlScN film could face up to 400 MPa

stress at the step of the patterned bottom electrode. Such a stress gradient is a potential source for crack generation during the liberation process. (Figure 3.16.). Solving this problem, we introduced a 200 nm thick low-stress Si_3N_4 layer on the

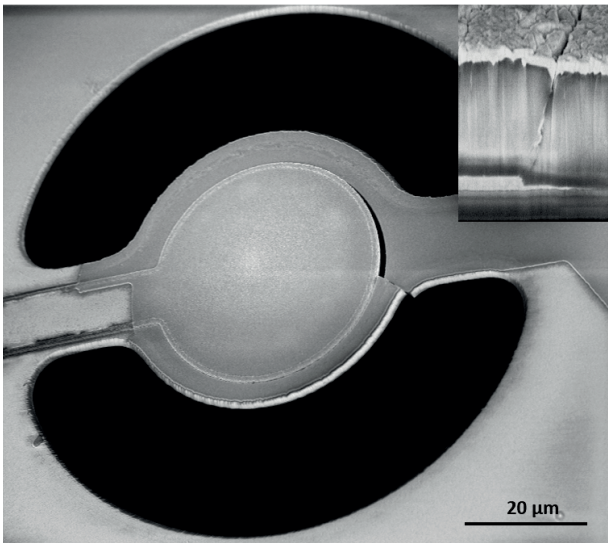

Figure 3.16: Membranes cracked due to the stress gradient in the border of the bottom electrode.

Si substrate below the oxide layer. This thickness of nitride layer introduces tensile stress around 300 MPa on the oxide layer, resulting in net stress less than 100 MPa for AlScN on the patterned bottom electrode border. Besides the stress profile modification, we reduced cracking probability by making the BE step oblique (less height difference). To achieve this, we introduced 45°tilt on the substrate holder during the BE IBE, which resulted in an inclined transition at the BE borders. Applying these modifications, all the designed devices fabricated and liberated successfully. Figure 3.17 shows fabricated shape resonators.

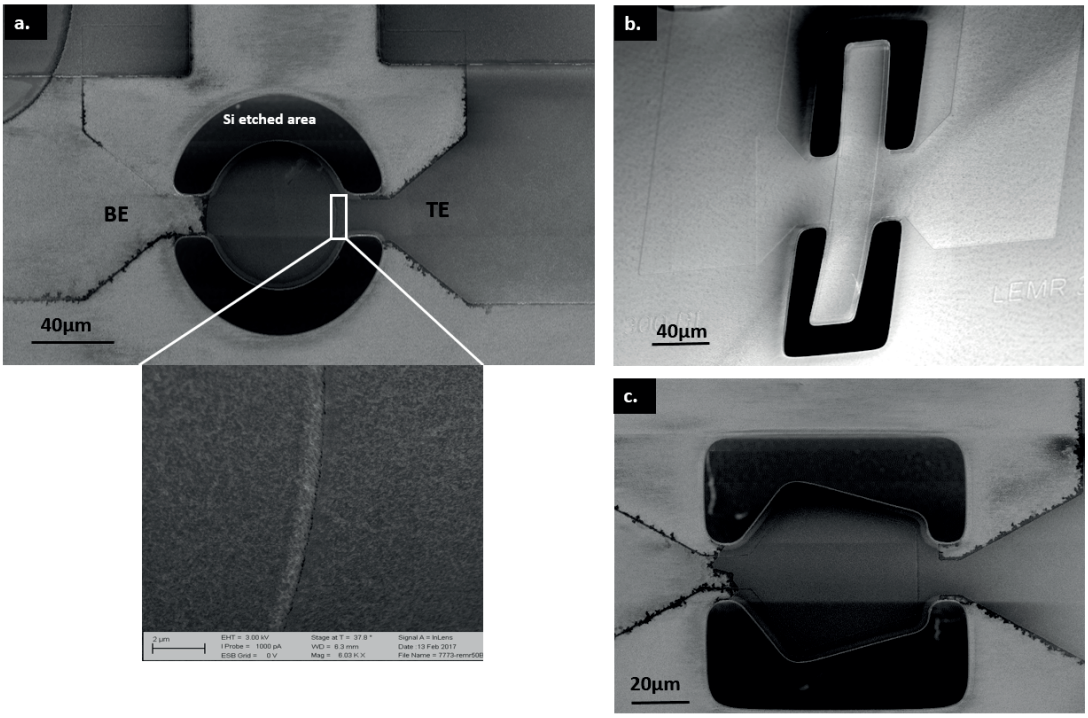

Figure 3.17: Rounding the sharp edges and introducing the nitride layer, resulted in disappearing of cracks in the liberation process. (a.) Shows the REM resonator. No crack observed in BE border. (b.) LEMR successfully liberated without any crack. Bending of the membrane shows that the membrane is still under stress.

Chapter 4

Material Parameter Extraction for Complex AlScN Thin Film

4.1 Introduction

The novel thin film alloy of $AlN_{(1-x)}$-$ScN_{(x)}$, a solid solution between the piezoelectric wurtzite AlN and the non-piezoelectric rocksalt structure ScN, exhibits extraordinarily high piezoelectric coefficients for a nitride material [38, 39] Since its discovery by Akiyama and coworkers, many researchers confirmed the increase of piezoelectricity with increasing Sc content, [109, 111, 112, 124, 127, 129, 135, 153, 154] reaching a maximum at the limit of the wurtzite stability somewhere between 40 and 50% of Sc on the cation site [128]. The piezoelectric coefficients increase by about a factor of 4 for the case of charge per stress coefficients (d-tensor), and about a factor 2.5 for the case of charge per strain coefficients (e-tensor). Computational modeling in the frame of density functional theory (DFT) confirmed very well the increase of the piezoelectric coefficients, accompanied by a decrease of the stiffness as a function of Sc content [108,113]. The piezoelectric constants are a factor of 5 to 10 smaller than the ones of good ferroelectric thin films of PZT ($PbZr_{0.53}Ti_{0.47}O_3$) and PMN-PT ($PbMg_{0.33}Nb_{0.67}O_3$ - $PbTiO_3$). However, for many applications, the dielectric constant (ε) is very relevant as well. In AlScN, ε is 50 to 100 times smaller than in PZT thin films. For sensors and vibration energy harvesters, the voltage response plays an important role. It is proportional to e/ε and thus about 10 times larger with AlScN thin films compared to the mentioned ferroelectric thin films. Furthermore, the signal to noise ratio, which is proportional to $e^2/\sqrt{\varepsilon.tan\delta'}$, is still superior with AlScN, because losses are much smaller in AlN and AlScN. For power generation in energy harvesters a figure of merit of e^2/ε is derived from the current×voltage product [109, 155]. In this case, both materials families have

competing performances when choosing a high Sc concentration. In ultrasound applications, for which the piezoelectric coupling $e^2/c.\varepsilon$ is relevant [111, 112] (c means the relevant stiffness constant), AlScN might be preferred for its easier integration onto silicon. AlScN is thus a very competitive material for many MEMS applications. In the lower GHz range, in which mobile phone communication takes place, the much higher acoustic quality factor of the AlN family is the decisive property for the realization of low-loss RF filters. The basis for mass applications is already prepared by the very successful exploitation of AlN thin films in radio frequency (RF) filters for mobile phones [1618]. AlN thin films have indeed many favorable properties (see, e.g., ref [61, 107] and references therein) for RF applications up to about 10 GHz [156]. Like AlN, its alloy with ScN is semiconductor compatible. The required (0001)-textured, polycrystalline wurtzite thin films are deposited like AlN at relatively low temperatures by means of RF or pulsed DC magnetron sputtering processes [86]. In RF applications, the high piezoelectric coupling of AlScN can increase the width of passband filters for mobile phones, and thus enable to increase the data rate, or number of users. In addition, new types of micro resonators will have enough performance to become interesting for mobile communication. In the wider MEMS field, the high piezoelectric coupling opens up many new applications in the domain of sensors, vibration energy harvesters, micro actuators, and microfluidics. The functional units can be active cantilevers, bridges, membranes, and transducers generating surface acoustic waves (SAW) [120, 157]. As the growth of AlScN films is more delicate compared to AlN films, optimization of material perfection for a high mechanical quality factor, and mechanical stress control are some of the major issues in works towards industrialization. In addition, the wide compositional range of the solid solution wurtzite phase requires detailed investigations and correlation between properties and composition for proper design of microacoustic components. In the general case, a full set of elastic, dielectric, and electromechanical coefficients is required. From the scientific point of view, the comparison of measured properties with the ones obtained by computational DFT modeling is of very high interest in order to understand the electro-mechanical phenomenon on the level of the unit cell. Property parameters are preferentially extracted either from SAW devices [65] or from single mode resonators. The latter depends on a very reduced set of coefficients [66]. The precise experimental extraction of piezoelectric constants of AlScN thin film was often hampered by some practical factors such as complicated fabrication processes [66] or difficulties in the growth of high-quality (0001) textured thin films [158]. SAW device characterization and simulation were employed by Tang et al. to evaluate the constants reported by Caro et al. for 32%, 40% and 43% Sc content [159]. However, it should be noted that the parameter calculation through the SAW characterization has a certain uncertainty since all 11 materials parameters must be considered for an

overall fitting [160]. Normally, properties are suitably measured in single crystal films, or perfectly c-textured films with a hexagonal symmetry. Sound velocities can be precisely determined if all involved layers are included in the calculations. This article describes the extraction of materials parameters for shear and longitudinal waves using the same device resonating in the thickness mode. This is realized by a technique using a film with slightly tilted c-planes [98], allowing in principle for the determination of 6 (c_{33}, c_{55}, e_{33}, e_{15}, ε_{33}, ε_{11}) of the 11 independent materials parameters from one thin film bulk acoustic resonator (TFBAR). The interesting point is that all the 6 coefficients are determined from one type of resonator, which we call dual mode, disc-shaped TFBAR. Such a technique reduces the fabrication effort as compared to the use of two different resonators, and in addition, the obtained values are valid for exactly the same film. It is therefore not necessary to fabricate a specific resonator for shear mode excitation only, as proposed in the work of Konno et al. [66]. An unforeseen complication in the growth of the AlScN thin film motivated us to extend the method to a double layer with two different film morphologies. The film started growing in the desired slightly tilted (0001)-texture, but after about 200 nm, new grains nucleated, covering at the end completely the first layer. TEM nano-diffraction mapping showed that this second layer contains mostly heavily tilted grains. Such a phenomenon of c-axis instability was discovered earlier [127]. In this work, we found that the occurrence of such abnormally oriented grains is more frequent on electrically isolated, small electrodes, as typically required in devices. Films deposited on wafers that were fully covered by a Pt(111) film did not show this phenomenon with the given process. It is not the aim of this article to report on such grain formation, which is treated in reference [126]. In this work, the statistics of grain tilts are used to define a finite element model (FEM), and to calculate the basic shear and longitudinal thickness resonances as appearing in the impedance spectrum. Comparison with the measured electrical impedance allows then for the derivation of single crystal elastic and even piezoelectric properties. Using the combination of TEM results which constrain and validate the FEM models, we can describe how the disordered second layer contributes to the piezoelectric response. To the knowledge of the authors, such TEM-FEM approach was never applied before to polycrystalline piezoelectrics. The article is organized as follows: The fabrication of the device, and the measurement of the electrical impedance are described in Section 4.2. In Section4.3, resonance frequencies and coupling constants are calculated for the case of unloaded single crystal wurtzite plates with tilted c-planes. The obvious discrepancy with the experiment, lead to the TEM study of microstructure and grain orientation, which is presented in Section 4.4. Section 4.5 deals with an analytical model considering all layers in the device, and the finite element modeling of the complex layer with multiple grain orientations.

4.2 Device Fabrication and Characterization

Polycrystalline, textured $Al_{0.85}Sc_{0.15}N$ films were deposited in a pulsed DC, reactive, magnetron sputtering process in a chamber attached to a cluster tool (Spider machine from Pfeiffer). The target was a 200 mm diameter, 6 mm thick plate of nominal $(AlN)_{0.835}$-$(ScN)_{0.175}$ hot pressed powder alloy. Prior to the deposition, the system was pumped down to a base pressure below 10^{-7} mbar. The applied DC power amounted to 1500W, the pulse sequence had a duty cycle of 90%, and the substrate was subjected to an RF power of 4W. The deposition temperature was set at 350 ℃. These parameters are identical those used by Matloub et al. [109,111] in the same tool. 100 nm thick, (111)-textured Pt thin films were used as bottom electrodes. Such films are known to promote the (0001)-orientation of AlN [87,161] and AlScN [109]. The slightly tilted growth was achieved due to a built-in feature of planar, magnetron sputter sources, which provide a net oblique flux at the border region of the wafer when operated in a static way. This leads to a small tilt of the c-planes of a few degrees [30]. We preferred such a small tilt in a standard tool, rather than to apply substrate tilting for enhancing the tilt effect [41,122,162]. A robust, 5-mask, CMOS compatible microfabrication route has been developed for the fabrication of the free standing TFBARs. Figure 4.1 shows schematically the employed process flow applied on a 100 mm diameter silicon wafer. First, a 200 nm thick SiO_2 layer was grown by wet oxidation. Next, a 200 nm thick low-stress Si_3N_4 layer was deposited by LPCVD, serving to compensate the compressive stress of the oxide. This step is crucial to prevent cracking of the anchors (bridges) during the later releasing step. Both dielectric buffer layers together are also important for the reduction of parasitic capacitances and losses between the contact pads since silicon forms a lossy conductor [147,148]. A 220 nm thick Pt film was sputter deposited at 350℃and was subsequently patterned by Ion Beam Etching (IBE) to form the bottom electrode. A 1.27 μm thick $Al_{0.85}Sc_{0.15}N$ thin film was deposited subsequently. The 200 nm thick, Pt top electrode was deposited and patterned with the same techniques as the bottom electrode. Hot phosphoric acid (85 vol% H_3PO_4 at 130℃) was used to remove the AlScN film for the opening of the bottom electrode contacts. A contact metallization of 200 nm Au on 30 nm Cr was selectively deposited by sputter deposition combined with a lift-off process using a LOR resist. This metallization improves the electrical contact between probe tips and contact pads and enhances the mechanical durability of the tips. Subsequently, the $AlScN/Si_3N_4/SiO_2$ layer stack was patterned by pulsed IBE using photoresist (PR) as a masking material. This process thus defines the in-plane confinement of the liberated plate. The active resonator area is defined by the top electrode. Finally, devices were released from the Si substrate by top-side isotropic dry etching of Si in SF_6. The selectivity between PR and AlScN in the IBE process

was about 1:2. The Si_3N_4/SiO_2 bilayer was maintained as membrane support. It is in general difficult etch AlScN. Dry etching in Cl_2 chemistry is the standard method for etching AlN thin films, however, this process is not efficient enough for AlScN etching. It was observed that the Sc doping increases the chemical resistivity of the nitride film. The selectivity with regard to PR is reduced by a factor of 2. The dry etching of AlScN in an IBE reactor showed good results, when the fences were removed by variation of the impact angle.

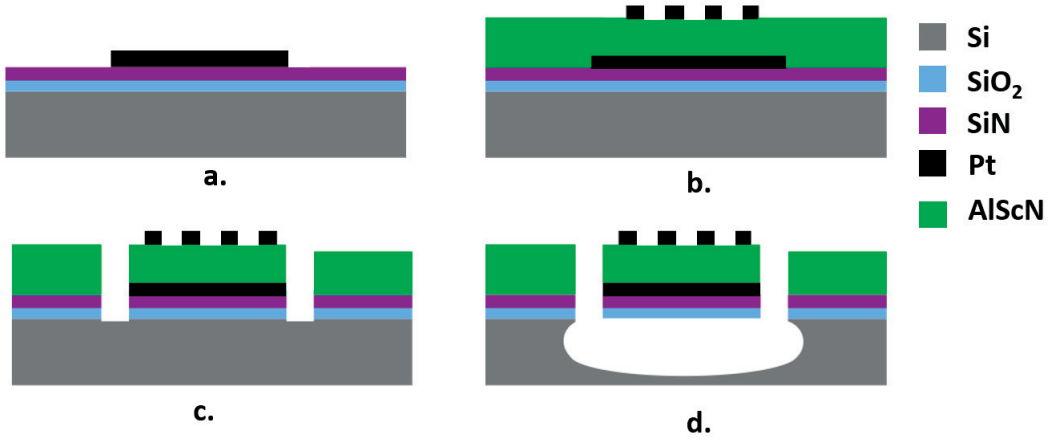

Figure 4.1: Schematic view of the process flow of the AlScN piezoelectric resonators. The drawn section is orthogonal to the two bridges with the contact lines. (a.) Deposition of the supporting layers and the bottom electrode, including patterning of the latter; (b.) deposition of AlScN, Pt and top electrode etching; (c.) Definition of the contours of the resonator plate by IBE of the complete layer stack; (d.) isotropic dry etching in SF6 from the top side to liberate the resonators from the substrate. The opening of the access to the bottom electrode by wet etching, and the gold deposition onto the contact pads are not visible in these drawings.

The fabricated resonators were characterized by means of an HP 8720D Vector Network Analyzer. The impedance value $\mid Z \mid$ is plotted as a function of frequency in Figure 4.2 for two devices on the same wafer. The results look at the first sight as expected: The longitudinal mode shows up at about twice the frequency of the shear mode resonance, and is much stronger than the latter, because the z-axis tilting is expected to be small. Indeed, the experimental coupling for the shear mode was derived as k_s^2=0.36% and 0.41 % for sample 1 and 2, respectively, and corresponds well to tilting angles in the range from 3.5°-5° [41, 141]. However, the experimental coupling for the longitudinal mode, derived as k_L^2= 0.70% for both devices, is significantly lower than expected. The analytical single crystal

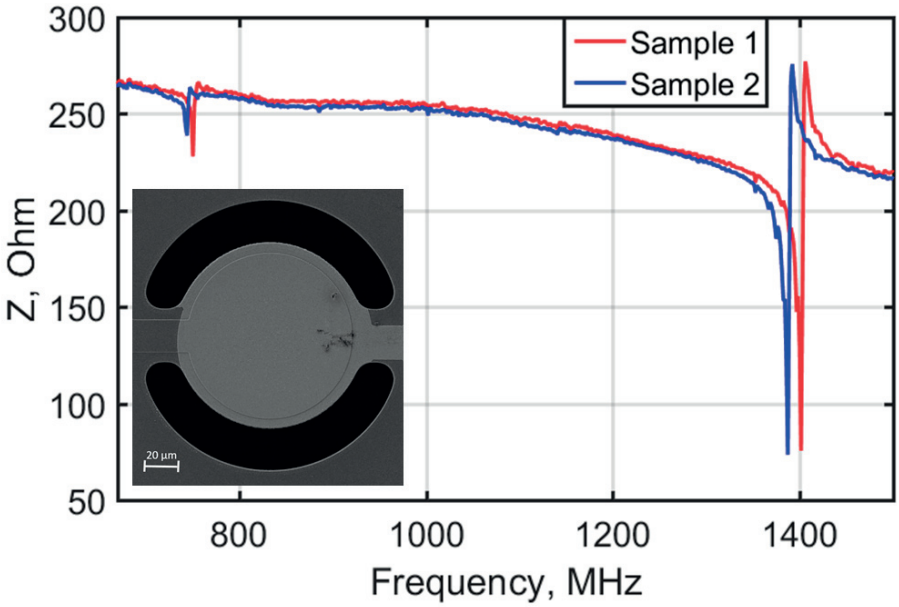

Figure 4.2: Absolute impedance value measured at two TFBAR devices. The insert shows an SEM top view of one of them.

plate model developed in the following section predicted a longitudinal coupling coefficient of $k_L^2 = 7.6$ %. The loading by the passive layers of the resonator does not explain such a large reduction. Using the analytical model that includes the loading effects, as presented in Section 4.5, and applied for the case of a single active layer, one even would expect a coupling of $k_L^2 = 8.3\%$. For this reason, a TEM investigation was carried out at a FIB cross section in order to find the reason for such reduction (see Section 4.4).

It is worth mentioning that same type of devices showed the radius extensional mode resonance at 38 MHz. This characteristic is employed by our partner to extract material parameters s_{11}^E and s_{12}^E. They also characterized besides the REMR , the length extensional mode resonators (LEMRs), which were fabricated in the same wafer as the discussing disc shape resonators to determine d_{31} and s_{11}^E. Results are published in reference [163]. It means that the dual mode disc shape resonator is capable of delivering 8 out of 11 independent material parameters.

4.3 Theory of Thickness Mode Resonances of Unloaded Single Crystal Wurtzite Plate with Tilted c-planes

In this section, the tilting of the polar axis is theoretically analyzed with regard to coupling and sound velocity. We consider first the simple case with no tilting. AlScN belongs to the hexagonal point symmetry group (6mm), which has 11 independent materials constants, including density ρ, stiffness constants c_{11}, c_{12}, c_{13}, c_{33}, c_{44}, piezoelectric constants e_{33}, e_{31}, e_{15} and dielectric constants ε_{11} and ε_{33} [76, 164]. In an ideal (unloaded) thin film bulk acoustic wave resonator made of a perfect (0001) oriented film, the resonance results from a longitudinal wave running along the crystallographic [0001] direction (polar axis), which is trapped in the film slab of thickness t. The formed stationary wave corresponds to a thickness resonance. The fundamental mode has a wavelength of $\lambda = t/2$, and the parallel resonance frequency (f_p) is calculated as:

$$f_p = \frac{v_l}{2t} = \frac{1}{2t}\sqrt{\frac{c_{33}^D}{\rho}} \tag{4.1}$$

where V_L is longitudinal sound velocity, t is the film thickness and c_D^{33} is the stiffness constant at constant field D . The difference between f_p and series resonance f_s is governed by the coupling coefficient:

$$k_t^2 = \frac{e_{33}^2}{c_{33}^D \varepsilon_0 \varepsilon_{33}^S} \approx \frac{\pi^2}{4}\frac{f_p - f_s}{f_p} \tag{4.2}$$

Thus, we can determine precisely the parameters c_{33}^D and e_{33} from the resonance, when knowing the dielectric constant. In the real case, it is essential to take into account the mass loading effect of the electrodes and further layers in the structure [26] (described in the complete 1D model in Section 4.5). The shear coefficients c_{44}^E and e_{15} can be determined from a thickness shear mode resonance [66, 165]. A pure shear mode resonance occurs when the applied electric field is perpendicular to the polar direction. In the general case, when the electric field is neither parallel nor orthogonal to the polar direction, shear and longitudinal strains are generated at the same time. Thickness mode resonances occur for both, albeit at different frequencies, because shear and longitudinal waves differ in their sound velocities (see, e.g., [121]). In a pure shear mode, the stiffness constant can be determined from the series resonance frequency as follows:

$$f_s = \frac{V_S}{2t} = \frac{1}{2t}\sqrt{\frac{c_{44}^E}{\rho}} \tag{4.3}$$

where V_S is the shear sound velocity. The piezoelectric constant e_{15} can be obtained from the respective coupling term:

$$k_{15}^2 = \frac{e_{15}^2}{c_{44}^D \varepsilon_{11}^s} \tag{4.4}$$

The dielectric constant of the film, $\varepsilon_{33,f}$ can be determined by off-resonance parallel plate capacitance measurements. This quantity is related to the fully clamped dielectric constant, ε_{33}^S, through the Equitation 4.5 [61].

$$\varepsilon_{33,f} = \varepsilon_{33}^S + e_{31}^2/c_{33}^E \tag{4.5}$$

The density can be determined by X-ray reflectivity (XRR) [166, 167], or even by the mass determination of a film of known thickness. For finding the stiffness matrix of a tilted wurtzite, we consider that the point group 6mm leads to isotropy in the plane perpendicular to the c-axis. For a fourth rank tensor, like the rigidity, this corresponds to the cylindrical symmetry. Tilting the c-axis around the Y-axis (tilt angle θ) maintains the mirror plane my intact, and we obtain a stiffness tensor for a monoclinic symmetry. In this system, we name the tensors $C^{'}$ (at constant E) for the stiffness, $e^{'}$ for the piezoelectricity, and $\varepsilon^{'}$ for the dielectric constants [168, 169].

$$C' = \begin{pmatrix} c_{11}^{'} & c_{12}^{'} & c_{13}^{'} & 0 & c_{15}^{'} & 0 \\ c_{21}^{'} & c_{22}^{'} & c_{23}^{'} & 0 & c_{25}^{'} & 0 \\ c_{31}^{'} & c_{32}^{'} & c_{33}^{'} & 0 & c_{35}^{'} & 0 \\ 0 & 0 & 0 & c_{44}^{'} & 0 & c_{46}^{'} \\ c_{51}^{'} & c_{52}^{'} & c_{53}^{'} & 0 & c_{55}^{'} & 0 \\ 0 & 0 & 0 & c_{46}^{'} & 0 & c_{66}^{'} \end{pmatrix},$$

$$e' = \begin{pmatrix} e_{11}^{'} & e_{12}^{'} & e_{13}^{'} & 0 & e_{15}^{'} & 0 \\ 0 & 0 & 0 & e_{24}^{'} & 0 & e_{26}^{'} \\ e_{31}^{'} & e_{32}^{'} & e_{33}^{'} & 0 & e_{35}^{'} & 0 \end{pmatrix}, \tag{4.6}$$

$$\varepsilon' = \begin{pmatrix} \varepsilon_{11}^{'} & 0 & 0 \\ 0 & \varepsilon_{22}^{'} & 0 \\ 0 & 0 & \varepsilon_{33}^{'} \end{pmatrix}$$

For the calculation of the velocities we solve the wave propagation equations (see Appendix. A), which describe the coupled electro-elastic wave propagation in a piezoelectric medium [170]:

$$\begin{cases} c_{ilmn}^E \frac{\partial^2 U_m}{\partial x_l \partial x_n} + e_{mil} \frac{\partial^2 \phi}{\partial x_l \partial x_m} = \rho \frac{\partial^2 U_i}{\partial^2 t} \\ c_{ilmn}^E \frac{\partial^2 U_l}{\partial x_i \partial x_m} - \varepsilon_{il} \frac{\partial^2 \phi}{\partial x_i \partial x_l} = 0 \end{cases} \qquad (i, l, m, n = 1, 2, 3) \tag{4.7}$$

U_m is mechanical displacement, e_{mil} is the piezoelectric tensor, c^E_{ilmn} is elastic moduli, ε_{il} is permittivity, ρ is material density, and ϕ is electrical potential. The phase velocity of quasi-longitudinal waves (V_L) and quasi-shear wave (V_S) can be determined by solving Equation 4.8 yielding:

$$\begin{aligned} V_L &= \sqrt{\frac{\widetilde{C'_{55}}+\widetilde{C'_{35}}}{2\rho}+\sqrt{\left(\frac{\widetilde{C'_{33}}-\widetilde{C'_{55}}}{2\rho}\right)^2+\left(\frac{\widetilde{C'_{55}}+\widetilde{C'_{35}}}{2\rho}\right)^2}}, \\ V_S &= \sqrt{\frac{\widetilde{C'_{33}}+\widetilde{C'_{55}}}{2\rho}-\sqrt{\left(\frac{\widetilde{C'_{33}}-\widetilde{C'_{55}}}{2\rho}\right)^2+\left(\frac{\widetilde{C'_{55}}+\widetilde{C'_{35}}}{2\rho}\right)^2}} \end{aligned} \tag{4.8}$$

where, $\widetilde{c'_{55}} = c'^D_{55} + \frac{e'^2_{35}}{\varepsilon'_{33}}$, $\widetilde{c'_{35}} = c'^D_{35} + \frac{e'_{35}e'_{33}}{\varepsilon'_{33}}$ and $\widetilde{c'_{33}} = c'^D_{33} + \frac{e'^2_{33}}{\varepsilon'_{33}}$ are stiffened elastic constants. The effective piezoelectric constants are defined as [171]:(Equation 4.9)

$$\begin{cases} e^{L,S}_{eff} = e'_{35}sin\alpha + e'_{33}cos\alpha, \\ e^{S}_{eff} = e'_{35}cos\alpha - e'_{33}sin\alpha \\ tan(2\alpha) = \frac{2\widetilde{c'_{35}}}{\widetilde{c'_{33}}-\widetilde{c'_{55}}} \end{cases} \tag{4.9}$$

Where, α is the angle between longitudinal wave propagation direction and Z axis. The effective electromechanical coupling is: :

$$\left(k^{L,S}_{eff}\right)^2 = \frac{(e^{L,S}_{eff})^2}{e'_{33}\ \rho V^2_{L,S}} \tag{4.10}$$

Using Equations 4.10 and 4.8, and knowing the materials parameters we can calculate V_S and V_L, as well as both coupling coefficients as a function of the c-axis tilting angle, θ. The result for $Al_{0.85}Sc_{0.15}N$ is shown in Figure 4.3. The materials parameters used in the calculation were ab-initio values reported by Caro et al. [113] : $c_{11} = c_{22} = 334.75$ GPa, $c_{12} = c_{21} = 129.44$ GPa, $c_{13} = c_{23} = c_{31} = c_{32} = 109.75$ GPa, $c_{33} = 283.25$ GPa, $c_{44} = c_{55} = 101.88$ GPa and $c_{66} = 102.66$ GPa. The rest of the stiffness tensor elements are zero. Non zero piezoelectric tensor elements are: $e_{15} = e_{24} = -0.347\ C/m^2$, $e_{31} = e_{32} = 0.688\ C/m^2$ and, $e_{33} = 1.716\ C/m^2$. The dielectric permittivity, $\varepsilon_{33} = 14.1$ and dielectric loss of 0.001 are extracted by direct capacitance measurements below the resonance frequency. The mass density of ρ= 3280 kg/m^3 was experimentally measured by XRR methods [86, 120] on a

PANalytical XPert Pro MRD diffractometer with a Ge (220) hybrid monochromator filtering the Cu-K1 radiation.

The phase velocities and the coupling constants for shear and longitudinal modes as a function of tilt angle are depicted in Figure 4.3. Like in AlN, the phase velocity for the shear wave is about half of the one of the longitudinal wave [172–174]. Applying a situation with a homogeneously tilted c-axis by 3.5°, a shear mode frequency of 733 MHz and a longitudinal mode frequency of 1290 MHz were calculated. The measured values are 2.5% and 9% higher, respectively. While this is almost in agreement with the model, the coupling shows a very strong deviation in the case of the longitudinal mode. Instead of 7.5% only 0.7% are measured. The measured 0.36 to 0.41% for the shear mode coupling, however, shows a good agreement with a tilt angle of the c-planes of 3 to 5 degrees. The bullet points in Figure 4.3.b illustrate the discrepancies. Small couplings for both modes are expected for large tilts of about 60°, but not for the expected small tilting angles. Although the free plate model does not consider the loading by the electrodes, it is enough accurate to conclude that the piezoelectric film does not exhibit properties as expected. For this reason, a TEM investigation was performed in order to elucidate the microstructure of the AlScN thin film in the device.

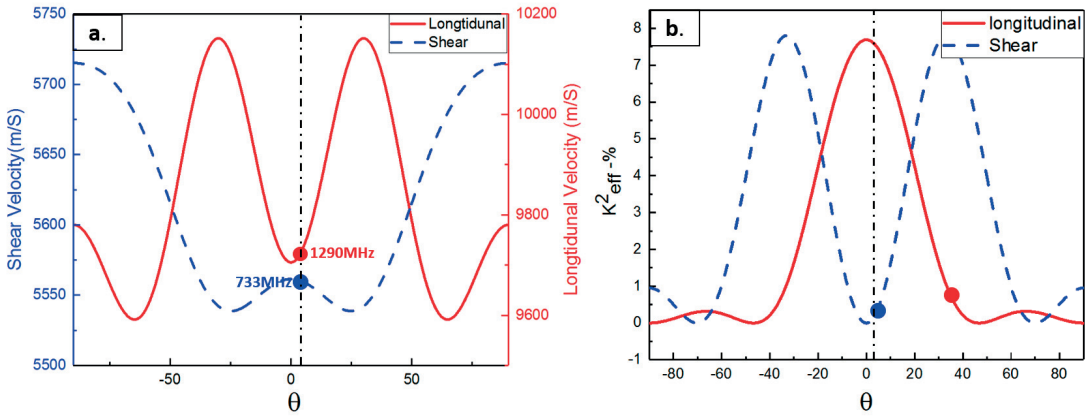

Figure 4.3: Theoretical properties of a free $Al_{0.85}Sc_{0.15}N$ single crystal plate having a tilt of the c-axis by the angle θ based on ab-initio material constants reported by Caro et al. [113]. (a.) Sound velocities V_S and V_L as a function of θ. The dashed line shows the $\theta = 3.5°$ position, corresponding to the tilt measured by TEM nano-diffraction (see section 4.4); (b.) Effective coupling constants as a function of θ . The experimental values are bulleted out on the curves.

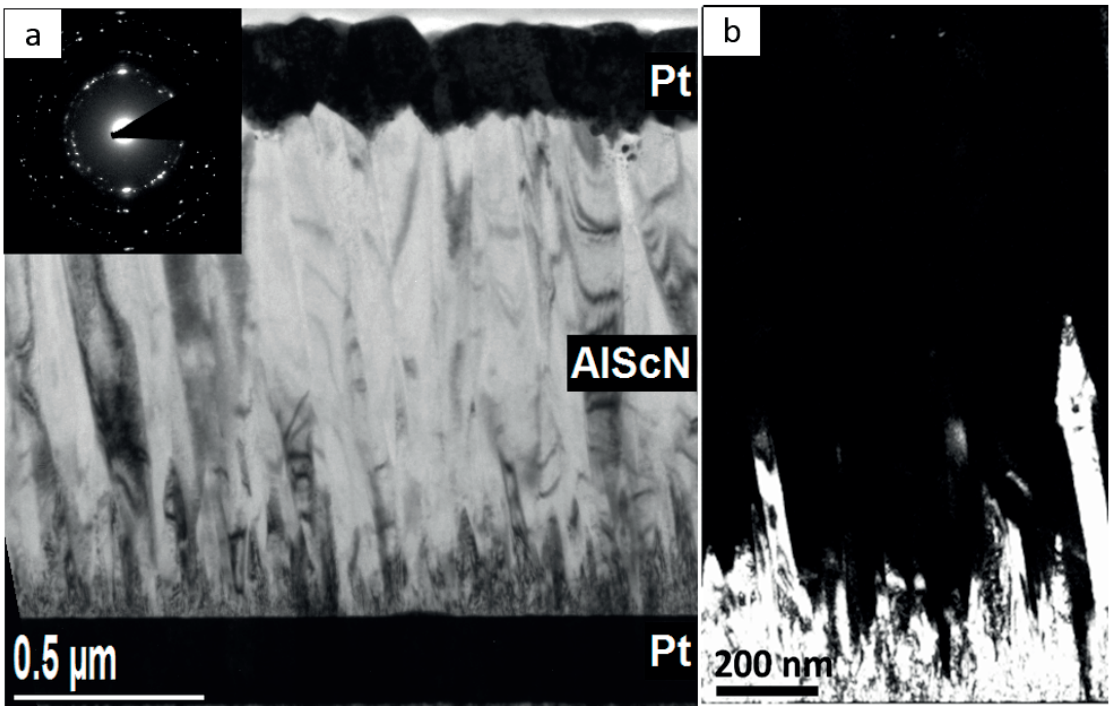

Figure 4.4: (a.) Bright Field and SAED pattern of the AlScN film. (b.) Dark-field images in which (0002)-oriented grains appear bright. In this example, the bright areas correspond to 23% of the total AlScN thickness.

4.4 Microstructural analysis

A FIB-lamella was cut from the investigated resonator in the radial direction (tilt direction) of the wafer in order to investigate the microstructure of AlScN film. The majority of boundaries of the columnar grains show an inclination of around 10° with respect to the substrate normal, as observed in bright-field (BF) images (Figure 4.4.a). The dark-field (DF) images obtained from the (0002) diffraction spot along the substrate normal show that the crystallites growing from the Pt bottom electrode are (0001)-textured. The DF image shows that the c-axis texture is lost during film growth. The quantitative analysis of DF images from different regions of the sample reveals that the height of the textured region varies in the range of 15%-23% of the film thickness (Figure 4.4.b). This phenomenon of deviating (0001)-textures in w-$Al_xSc_{1-x}N$ films was first reported by Fichtner et al. [127]. Protruding cone-like crystallites with other orientations were reported to occur as a result of an interface instability phenomenon. In our case, however, the instability does not occur at the interface, but in later growth stages (with a few exceptions),

as explained in ref. [126].

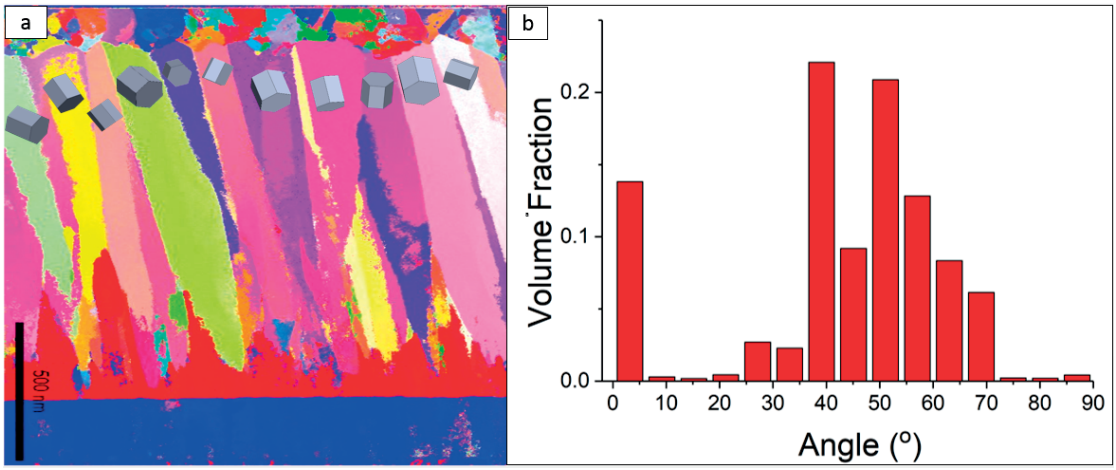

Figure 4.5: (a.) TEM nanodiffraction combined with Automated Crystal Orientation Mapping of the AlScN film in the studied device. The inserted hexagonal cylinders show the crystallographic orientation of the grains. (b.) Histogram showing the volume fraction as a function of tilt angle. The width of the angle interval is 5°. The population with the smallest tilt angle corresponds to the red layer with a slight tilt of an average of 3.5°.

In order to assess quantitatively the orientation of the disordered grains, nanodiffraction mapping was performed by an ACOM-TEM [136, 175]. The result of the analysis is shown in Figure 4.5.a. The colors in the maps are given according to the c-axis orientation with respect to the substrate normal. Red corresponds to (0002) orientation, blue to $(11\bar{2}0)$ and green to $(10\bar{1}0)$ in the hexagonal wurtzite lattice. The (111) texture of the Pt layer was given blue color. We observed that the (0001) film texture (red) was lost after 300 nm above the Pt bottom electrode. In this initial layer (red) - making up 15% of the film volume the c-planes are tilted by 3.5° with respect to the substrate plane (note that grain boundaries are more tilted). This value corresponds well to the expected tilt. The hexagonal unit cell symbols inserted in Figure 4.5.a show the orientation of the corresponding grains in the upper part of the film. The distribution of the polarization direction with respect to the substrate normal is shown in Figure 4.5.b It is interesting to note that the deviation in the tilt angle varies mostly between 35° and 70°. This point is discussed in a ref. [126].

Based on the microstructural analysis, it can be concluded that 15%-23% of the totally 1270 nm thick AlScN film is c-oriented with a tilting of around 3.5° with respect to the substrate normal. Above this region, the film is losing it's

(0002)-texture and shows a variety of orientations with high tilt angles in the range of 3°5 to 70°, leading as observed to a small coupling of the longitudinal wave. The texture analysis does not imply any information on the polarity of the c-axis. As this one might be random, the upper layer might be not piezoelectric at all, in the average.

4.4.1 Experimental Details of the TEM Tools and Methods

The Automated Crystal Orientation Mapping (ACOMTEM) with the NanoMegas AS- TAR system [136,175,176] employed in this work using a transmission electron microscope (TEM), which collects and indexes nanodiffraction patterns over a scanned area of $2\mu m^2$. The spatial resolution of this system on a TEM exceeds that of standard EBSD techniques, being determined by the electron probe size and the scan step size. Scanning nanodiffraction system identifies crystal phase and orientation at every point in the sample with nanometer spatial resolution. The standard TEM investigations were performed on a 200 kV Tecnai Osiris TEM. NanoMegas ASTAR system was mounted on the JEOL 2200FS and has spatial resolution of 2nm with a C2 aperture of 10 μm.

4.5 Analytical and FEM Models of the Composite Transducer

For a more precise extraction of elastic and piezoelectric properties of the piezoelectric film, its microstructure must be considered. We performed two different approaches for simulation calculations. In both cases, the AlScN thin films were approximated by a bilayer, separated by a simple plane. The first, 240 nm thick layer is considered to be a perfect (0002)-oriented layer with a 3.5° tilt. The upper layer is treated first as a film with random polar direction, and piezoelectric coefficients of value zero. This approximation is treated as an analytical 1-dimensional (1D) model. In the second approach, the upper layer is simulated by finite element calculations, which includes sections of different orientations of piezoelectric AlScN material, thus simulating the grains with tilted c-planes as observed by TEM.

4.5.1 Analytical 1-Dimensional Model

The layer sequence of the 1D-model is drawn in Figure 4.6, together with the parameters governing the boundaries between the different media. The variable F means the forces, U the velocities, and V the electrical potentials. The exact

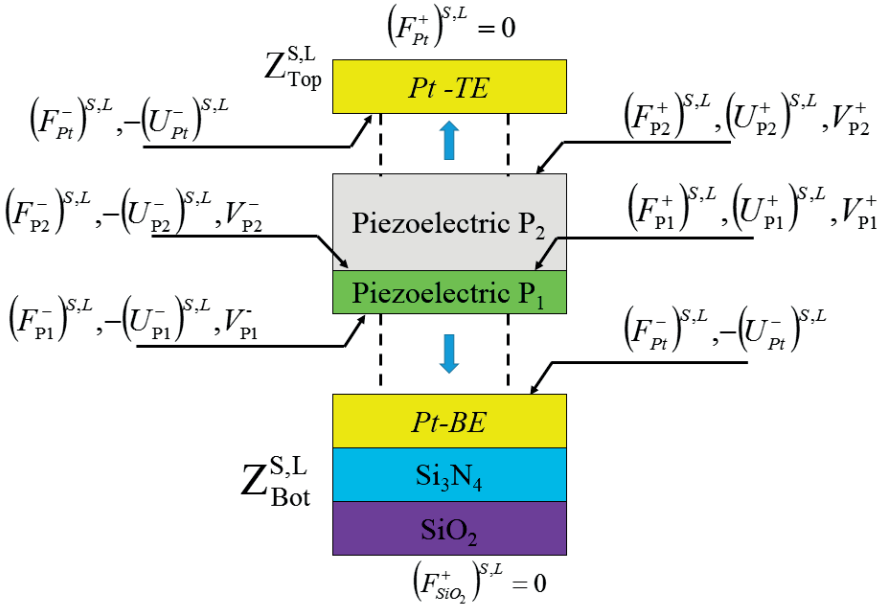

Figure 4.6: Schematic of the 1D model of the composite dual mode resonator consisting of two piezoelectric layers, the loading at the top and bottom interface (Z_{Top} and Z_{Bot}), and the two boundary conditions for free vibration ($F_{SiO_2} = F_{Pt} = 0$).Schematic of 1- D model of the composite dual mode resonator consisting of two piezoelectric layers and boundary conditions implemented for the transfer matrix calculations.

solution to this linear problem was found by the application of the transfer matrix method. For the electrical impedance calculation, the transfer matrix formalism implemented as described by Bloomfield [177]. As a result of this analytical model, the impedance for the longitudinal wave, Z^L , and the shear wave, Z^S , were determined as follows:

$$Z^{S,L} = \frac{V_0^{S,L}}{I^{S,L}} = \frac{a_{31}\left(a_{13} - a_{23}Z_{\text{Bot}}^{\text{S,L}}\right)\left(Z_{\text{Top}}^{\text{S,L}} + a_{32}\right)}{Z_{\text{Bot}}^{\text{S,L}}a_{21}\left(Z_{\text{Top}}^{\text{S,L}} + a_{22}\right) - a_{11}\left(Z_{\text{Top}}^{\text{S,L}} + a_{12}\right)} + a_{33} \tag{4.11}$$

where a_{ij} (i,j=1,2 and 3) are elements of transfer matrix **A** (see Appendix. B) relating the top of the second layer to the bottom of the first layer. $Z_{\text{Bot}}^{\text{S,L}}$, $Z_{\text{Top}}^{\text{S,L}}$ are the acoustic impedance of the bottom and top layers respectively. The total electrical impedance of the composite dual mode resonator is a superposition of

the shear and the longitudinal mode, as described in [171]:

$$Z_{\text{Total}} = Z^S + Z^L - \frac{1}{i\omega C_0} \tag{4.12}$$

where ω and C_0 are the angular frequency and static capacitance of the transducer, respectively. The model was fitted to the experimental impedance data using the target function F as follows:

$$F = [|Z_{Total}(c_{44}, c_{33}, e_{15}, e_{33}, \theta) - Z_{Experiment}|^2] \tag{4.13}$$

For the small tilting in layer P1, the stiffness constants c_{12}, and c_{11} as well as the transverse piezoelectric coefficient e_{31} do not play a substantial role and are assumed to be constant, i.e., they were assumed to be equal to the values given in Section 4.3. As a first guess, the layer P2 was considered to be a non-piezoelectric layer. This would be the case when the polar axis of the grains would point randomly in all directions. For simplicity, all piezoelectric constants e_{kl} were assumed to be zero. Regarding stiffness constants for this layer, we assume that every tilt angle occurs with the same probability, and that the stiffness can be averaged over all grains, as the electrode size is much larger than the grain size. Assuming that the tilt of the polar axis occurs only around one axis, as described in Section 4.3, the average stiffness ($\bar{c}_{ij}^D$) is obtained as an average over all angles:

$$c_{ij}^D = \frac{1}{\pi} \int_0^\pi (c_{ij}^{\prime D}) \theta d\theta \tag{4.14}$$

Note that the stiffness at constant D-field must be used, if piezoelectricity is switched off. In a first step, the frequency of the series resonance, f_s, is matched to the experimental value by varying c_{44}, and c_{33} for both the shear and the longitudinal mode. Then, the parameters c_{44}, and c_{33} are fixed, and the optimization is continued by varying the piezoelectric parameters e_{15}, and e_{33} in order to fit size and width of the resonances. Since the electromechanical coupling is defined by the distance between series resonance f_s, and parallel resonance f_p, the matching of both frequencies yields the coupling factors: k_L^2 equal 0.52%, and k_S^2 equal 0.16%. These values are much closer to the experimental values than the ones predicted for a fully piezoelectric film with a 3.5° tilt. Nevertheless, k_S^2 is too small. This indicates that the second layer P2 is not fully passive as assumed in the 1D analytical model. The calculated parameters from this model are presented in the first column of Table 4.1.

4.5.2 FEM Model of 2.5 Dimensions

From the TEM microstructural analysis, we know that the layer P2 comprises wurtzite grains with c-axis tilting angles in the range from 20° to 90°. In order to implement the observed tilt angles in a model, we passed to finite element modeling based on the COMSOL 5.3 version with the option of so-called 2.5D simulation. This allows for a significant reduction in computation time as compared to the classical 3D simulation. A $1\mu m$ wide resonator section is simulated with symmetrical boundary conditions in the lateral directions. In this model, the AlScN film consists of two layers. The first layer (P1) is 240 nm thick (corresponding to average 19% volume fraction obtained in TEM study) c-textured AlScN with 3.5° tilting in c-axis. The second layer (P2) consists of the 8 different orientation of grains. Grain orientations and volume fractions were taken from the TEM analysis data presented in Figure 4.5, omitting the grains with volume fraction less than 1%. The simulated structure is schematically shown in Figure 4.7. The same fitting procedure applied to the analytical model was implemented in this case. Table 4.1 presents the constants determined with the help of the 2.5 D model. Figure 4.8 compares the experimental, 1D analytical model and 2.5D FEM grain model impedance characteristics.

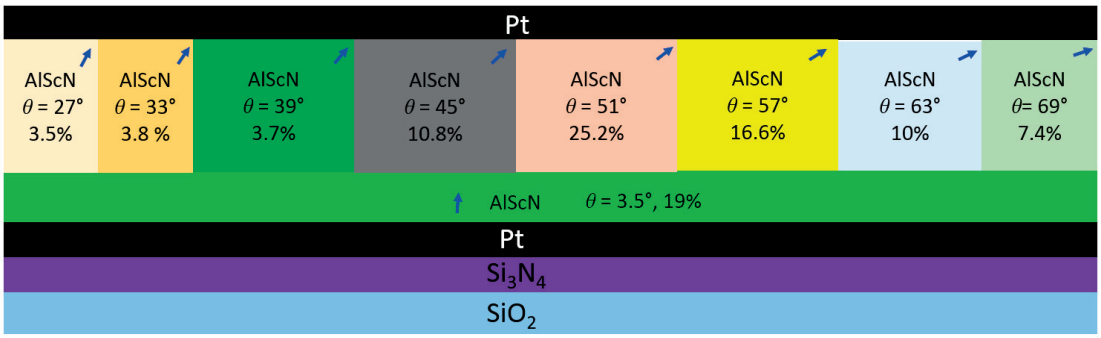

Figure 4.7: Resonator cross section using for 2.5 D finite element simulation. The arrows indicate the polar directions in the various sections.

With the FEM approach, we are able to address the question whether the abnormal grains maintain the sign of the vertical component of their polarization as in the first layer or not. This corresponds to the question is whether the tilt angle θ of the polar c-axis in abnormal grains is smaller than 90° or whether values above 90° occur as well. In the TEM observations, we cannot see the difference. However, the acoustic response is different for the two cases. In the case that the volume fraction with a tilt of $\theta + 180°$ is equal to the one of θ , the piezoelectric activity is

Table 4.1: Material parameters of the double layer dual mode resonator extracted from 1D analytical calculations (1D) and 2.5D FEM simulation (2.5D) in comparison with the experiment (EXP), and literature data from ab-initio calculations [113] (with and without HSE correction) and an experimental TFBAR result from reference [112]. The numbers in bold letters are results, the numbers in italics are fitted to the experiment.

Parameter	1D	2.5D	Exp k^2	Ab-inito,HSE	Ab-inito	Exp from [112]
c_{33}[Gpa]	273	**277**	-	310	283	270
c_{44}[Gpa]	89	**101**	-	112	102	-
e_{33}[C/m^2]	1.92	**1.88**	-	1.72	1.71	2.14
e_{15} [C/m^2]	-0.34	**-0.40**	-	-0.35	-0.32	-
k^2_{eff-L}(%)	0.35	0.71	0.70	-	-	12
k^2_{eff-S}(%)	0.21	0.40	0.41	-	-	-

almost canceling out, resulting in a k_L^2 of 0.14%, and k_S^2 of 0.05%. Comparison to the experimental result shows that there is an average piezoelectric activity of the upper layer adding to the one of the first layer, meaning that most of the tilt angles in the abnormal grains are less than 90°, and we can assign polar axes directions as sketched in Figure 4.7. The obtained value for the stiffness constant c_{33}^E of 277 GPa appears to be quite realistic. It is 11% smaller than the ab-initio value adjusted to the AlN endpoint, and 2% smaller than the non-adjusted ab-initio value. At the same time, it is 3% larger than an earlier experimental value from Moreiro et al. derived from a TFBAR resonance. The shear stiffness constant c_{44}^E as derived in our work shows the same relative deviations from the ab-initio values. In this case, there is no earlier experimental value available. The obtained piezoelectric coefficient e_{33} is 9% larger than predicted by ab-initio results from Caro et al. and 14% smaller than the previous experimental result. The e_{15} coefficient is 12% larger than the ab-initio value. Here we have no other experimental results available. The overall picture of the results shows that in general we have an agreement within about 10% with the ab-initio values adjusted to the AlN endpoint. The

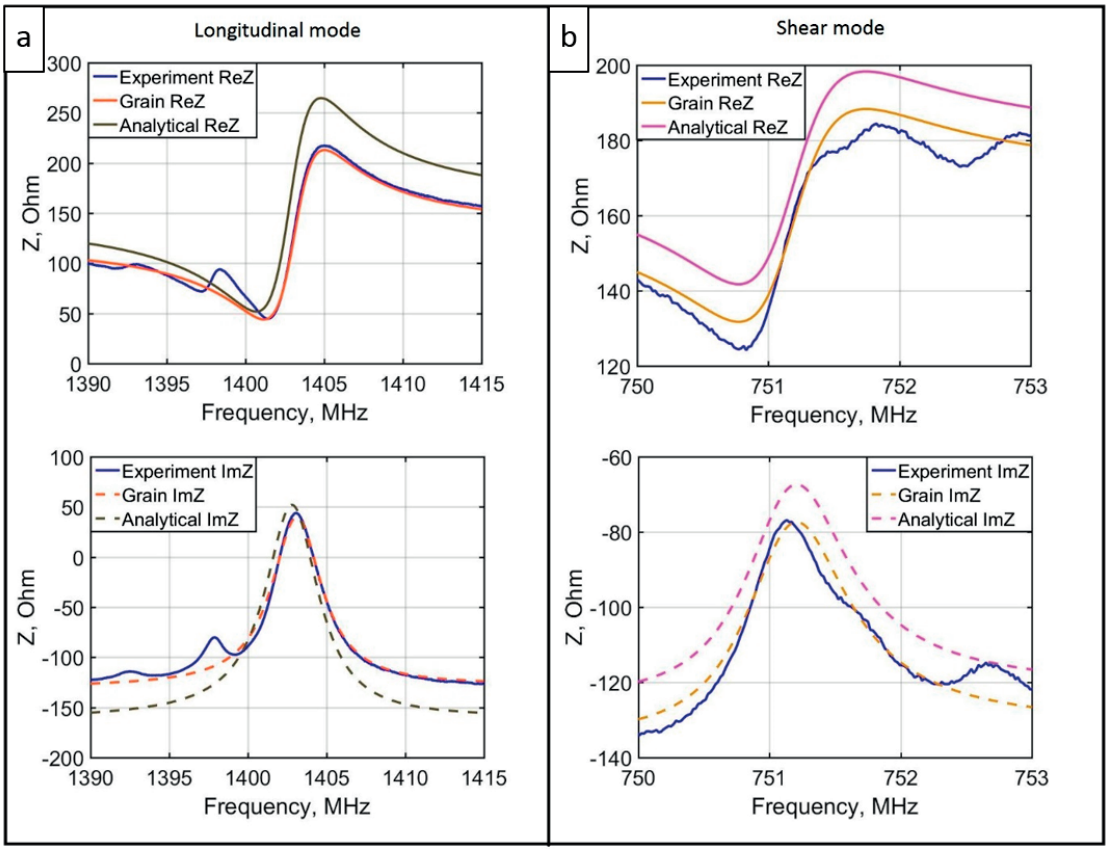

Figure 4.8: Comparison of the impedance characteristics of the experimental curve with simulated curves produced by extracted parameters from 1D and 2.5 D models.

experimental elastic constants c_{33} and c_{44} fit better to the non-adjusted ab-initio values. At the same time, the experimental piezoelectric constants turned out to be larger than the ones delivered by ab-initio calculations.

4.6 Conclusions

In this chapter, we extracted the material parameters c_{33}, c_{44}, e_{33}, e_{15}, ε_{33} for $Al_{0.85}Sc_{0.15}N$ thin film by characterizing, and modeling dual mode disc shape BAW resonators. A 3.5° tilting of the c-axis in the c-textured film resulted in the excitation and appearance of the shear mode resonance in addition to the longitudinal mode. As the film did not grow in the planned (0001) texture throughout the whole thickness, a novel approach had to be adopted for property determination. The

large tilt angles of the grains in the upper part of the film were assessed by TEM nano-diffraction combined with Automated Crystal Orientation Mapping. A finite element model (2.5D FEM) was constructed having in a second layer the misaligned grains with the orientations as found in TEM, and represented with the same volume fractions. The electrical impedance was calculated and fitted to the experimental impedance measured as a function of frequency. The constants c_{33}^E and e_{33} were determined from the basic longitudinal mode and c_{44}^E, and e_{15} were calculated from the basic shear mode. This method allowed also to make a statement about the overall piezoelectric activity of the upper layer with the misaligned grains. The latter pick-up the polarity from the first layer, meaning that the polar axis is tilted up to 90°, but not beyond. It is not clear whether this relation is caused by the secondary nucleation process, or caused by other growth conditions, like the on bombardment. The low longitudinal coupling in the misaligned layer originates mostly from the large tilt angles, and not from (hypothetical) grains that would have inverted polarity. Such a model yielded clearly much lower coupling coefficients. This was also the case for an analytical model considering a double layer with a passive upper layer. The final values giving the best fit to experiment are: $c_{33}^E = 277$ GPa, $c_{44}^E = 101$ GPa, $e_{33} = 1.88$ C/m^2, e_{15}=-0.40 C/m^2, $\varepsilon_{33} = 14.1$ and $\rho = 3280$ kg/m^3 for the investigated film with 15% Sc. These values agree within about 10% with the ab-initio values adjusted to the AlN endpoint, whereby the elastic constants fit better to the non-adjusted ab-initio values. The experimental piezoelectric constants turned out to be larger than the ones delivered by ab-initio calculations.

Chapter 5

$Al_{1-x}Sc_xN$ Lamb Wave Resonators

5.1 Free Standing and Solidly Mounted Lamb Wave Resonators based on $Al_{0.85}Sc_{0.15}N$ thin film

Introduction

In recent years, more and more frequency bands were assigned for mobile phone communication. The totality of bands is now ranging from 0.3 to 3.8 GHz [7, 8]. The currently dominating electroacoustic technologies are based on surface acoustic waves (SAW) on mainly $LiNbO_3$ single crystal surfaces, and thin film bulk acoustic waves (BAW) in AlN thin films. The SAW devices are more suitable for the lower frequency range, and the BAW devices for the higher frequency range. BAW devices are based on thin film bulk acoustic wave resonators (TFBAR). Their resonance frequency is inversely proportional to the film thickness. The lower frequency limit is imposed by a thickness limit for the piezoelectric thin films, beyond which fabrication costs become too high, and film integration too cumbersome. It is of high interest to dispose of an electroacoustic technology that would allow thin film technology for accessing the lower frequency range in order to cover a wider frequency range. Of course, the excellent features of AlN TFBARs in terms of acoustic quality, electromechanical coupling, thermal stability, and power handling should be maintained. In this context, lamb wave resonators attracted much attention. Their frequency is depending not only on the layer thickness, but also on the period of the interdigitated electrodes. The lowest order symmetric mode

(S_0) of AlN lamb wave resonators was explored since 2002 [178]. Such devices excel with a high phase velocity close to 10000 m/s, a weak phase velocity dispersion, a small temperature coefficient of frequency, and a high quality factor (Q). However, only moderate electromechanical coupling factors (k^2) are possible with pure AlN. J. Bjurstrom et al. reported k^2 of 0.85% and a Q of 880 at 570MHz, which gives a figure of merit Qk^2 for filter applications of 7.4 [42]. Chih-Ming Lin et.al achieved k^2 of 1.0% at 850 MHz, yielding a FoM of 8.9 [49,179]. They managed to boost the quality factor by employing biconvex edges. They also reported a k^2 of 0.18% with Q of 3280 (FoM equal to 5.9) at 490 MHz with AlN contour mode resonator [51] having a similar architecture as an LWR. The low coupling and figure of merit of AlN LWRs were an obstacle for the exploitation of such devices. This will possibly change with the advent of AlScN thin films, consisting of a solid solution of AlN and ScN (i.e., $Al_{1-x}Sc_xN$). Those grow in the piezoelectric wurtzite structure for an Sc content up to about x=40% when using suitable sputter deposition processes.

The piezoelectric coefficients of such thin films are much larger than the ones of AlN [39]. The use of AlScN will thus increase the piezoelectric coupling of Lamb wave devices. This was recently confirmed by the work of Konno et al. They obtained LWR resonators with a $Al_{0.6}Sc_{0.4}N$ thin film, and reported a k^2 of 7.3% and a FoM of about 8 at 2.6 GHz [165]. Hence, despite of the large increase of the coupling, the FoM did not improve.

In this work, we investigated Lamb wave devices theoretically and experimentally with $Al_{0.85}Sc_{0.15}N$ thin films. Two types of Lamb wave resonators (LWR) were fabricated: Freestanding (liberated from the substrate), and - for the first time - solidly mounted LWRs. In the latter, the substrate is acoustically decoupled by an acoustic Bragg reflector. With the free standing structures resonating at around 1.2 GHz, we again obtained FoMs of the same size as previously reported, i.e., 7 to 10. However, employing a Bragg mirror, significantly improved the figure of merit, reaching values close to 30. Such a value gives realistic perspectives for applications.

Design and FEM simulations

Lamb wave resonators can have three configurations regarding the bottom electrode. No bottom electrode, floating bottom electrode and grounded bottom electrode. The bottom electrode version (lateral field excitation in the reference [178]) shows a higher coupling than the one without bottom electrode (often referred to as IDT version in analogy to SAW devices) [36,49,178–180]. The floating bottom electrode has the advantage that only one voltage $Ue^{i\omega t}$ is needed for it's excitation, and that no via holes to the bottom electrode need to be fabricated.

The second pole of the Interdigitated electrode is connected to the ground signal, and the floating BE electrode is supposed to acquire the intermediate voltage $Ue^{i\omega t}/2$.

The grounding of the bottom electrode would need in addition a second AC signal with opposite polarity ($-Ue^{i\omega t}$) for feeding the second pole of the Interdigitated electrode. In this way, the BE would float at zero volt and could be connected to ground. However, there is no obvious gain in doing like this. In this work, we thus chose the floating bottom electrode configuration with one single AC signal. The thickness of the AlScN thin films was fixed to be 1μm for all devices. The free standing structures had wavelengths (λ) of 6 and 8 μm. In the case of the SMR structure, a single wavelength of 5 μm was chosen. The Interdigitated structures had 150 fingers (75 periods) in the active part, and 40 fingers in the floating reflector gratings placed in each side. The materials constants for the simulations were partially taken from previous experiments [181] (c_{33}=277 GPa, c_{55}=101 GPa, e_{33}=1.88 C/m^2, e_{15} =-0.40 C/m^2, ε_{33}=14.1) and from ab-initio data as published by Caro et al. [113] (c_{11}=366 GPa, c_{12}=143 GPa, c_{13}= 124 GPa, e_{31}= -0.69 C/m^2). For an estimation of the Q-factors, a mechanical quality Qm of 1000 was assumed for AlScN. The specific conductivity was programmed as 35.5×10^6 S/m for the Al film on top of AlScN, and 8.9×10^6 S/m for the Pt film below the AlScN.

In the SMR configuration, the Bragg reflector has to work well at the chosen operation frequency of 1.4 GHz. An AlScN thickness of 1 μm together with a wavelength λ=5μm were found to be optimal for this frequency, considering the loading effect of the reflector structure. Lamb wave modes emit a mixture of longitudinal and shear modes into the underlying substrate. Both modes must be considered in the reflector design. For pure modes, the ideal Bragg reflectors are multilayers of $\lambda/4$ layers [182]. As shear and longitudinal waves have different velocities, their wavelengths are different at a given frequency. Hence, Bragg reflectors used to reflect the longitudinal bulk waves are not the same as those used to reflect the shear bulk waves. A trade-off must therefore be found, to reflect the mixture of longitudinal and shear bulk waves emitted by the Lamb modes into the Bragg reflector. To deal with this problem, we introduced a weight factor R ($0 \leq R \leq 1$) defining the degree of longitudinality of the emitted wave mixture, where R=1 corresponds to a purely longitudinal bulk wave, and R=0 corresponds to a purely shear bulk wave. Tungsten (W) and SiO_2 were chosen as high and low impedance layers, having an acoustic impedance ratio of 7.9 This pair is a standard solution for thickness mode resonators with AlN [183]. The thickness of the SiO_2 layer was then the obtained as: $t_{SiO_2} = R \times \lambda_{L(SiO_2)}/4 + (1-R) \times \lambda_{S(SiO_2)}/4$, where λ_L and λ_S are longitudinal and shear wavelength respectively. The same formula was employed to calculate the thickness of the W layers. FEM predicted the value of R=0.3 as the optimal choice with the 5 layers SiO_2/W/SiO_2/W/SiO_2.

Since tungsten is a conductor, the reflector area must be restricted to the resonator area. Otherwise, all contacts and conductor lines on the wafer are connected by a parasitic capacitance.

Microfabrication

A 5-mask, CMOS compatible microfabrication route has been developed for the fabrication of the free-standing Lamb wave resonators. Figure 5.1 shows schematically the employed process flow applied on a 100 mm diameter silicon wafer and a top view SEM image of a fabricated device. First, a 200 nm thick SiO_2 layer was grown by wet oxidation. Next, a 200 nm thick low-stress Si_3N_4 layer was deposited by LPCVD, serving to compensate for the compressive stress of the oxide. This step is crucial to prevent cracking of the anchors (bridges) during the later releasing step. Both dielectric buffer layers together are also important for the reduction of parasitic capacitances and losses between the contact pads since silicon forms a lossy conductor [147, 148]. A 50 nm thick Pt film was sputter deposited at 350℃and was subsequently patterned by Ion Beam Etching (IBE) to form the bottom electrode. A 1μm thick $Al_{0.85}Sc_{0.15}N$ thin film was deposited by the same sputtering parameters as described in reference [181]. The 80 nm thick, aluminum top electrodes were sputtered deposited at room temperature and patterned by dry etching in Cl_2 gas. Subsequently, the $AlScN/Si_3N_4/SiO_2$ layer stack was patterned by pulsed ion beam etching (IBE) using photoresist (PR) as a masking material. This process thus defines the in-plane dimensions of the resonators. Finally, devices were released from the Si substrate by back-side anisotropic dry etching of Si in SF_6 (Bosch process), followed oxide and nitride removal by dry etching in CF_4.

The fabrication of the SMR device started with the deposition of two pairs of W/SiO_2 layers, their patterning, a SiO_2 deposition by CVD covering conformally all the reflectors and filling the gaps between them, followed finally by a global planarization by means of chemical mechanical polishing (CMP) in order to obtain a flat and smooth surface finishing with the last SiO_2 layer of the reflector. The Al top electrode thickness was chosen as 120 nm. FEM simulations indicated a higher coupling with this thickness.

Results and Discussions

Simulated and measured admittance amplitudes are shown in Figure 5.2 for 6 and 8μm wavelength. An almost perfect agreement between experiment and theory were obtained. The experimental coupling factors reach 92% and 95% of theoretical ones, and the frequencies fit very well together. This indicates that the value of

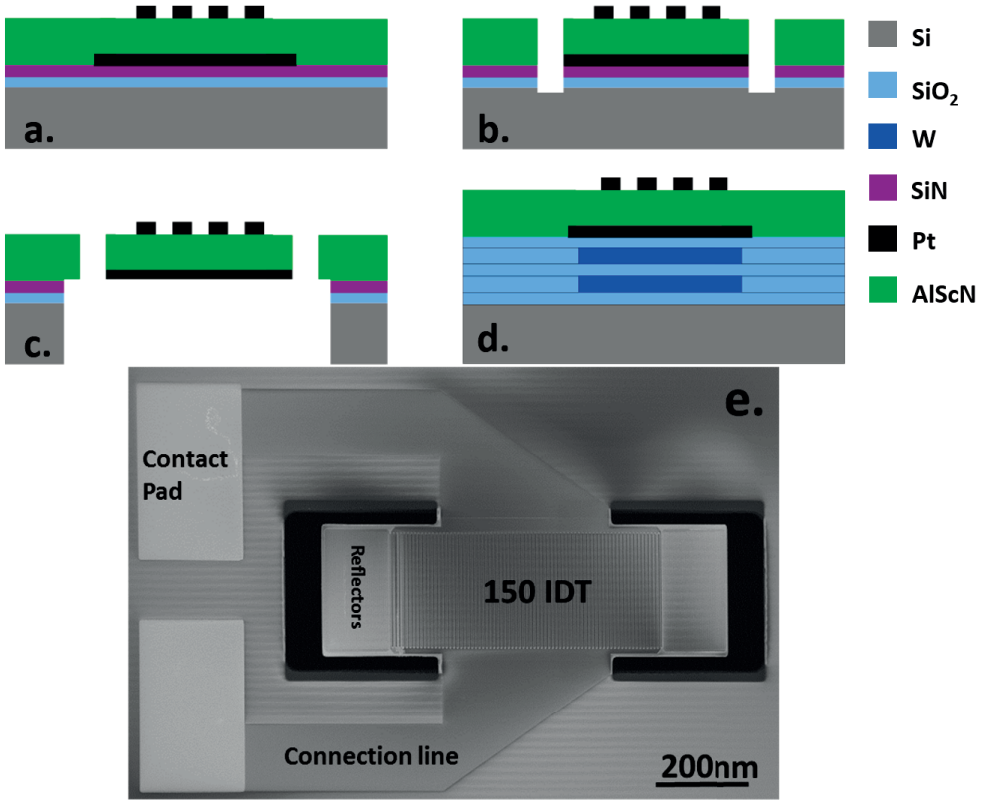

Figure 5.1: Schematic cross sections of the fabricated resonators: The free standing LWR after layers depositions and top electrode patterning (a), after front side liberation (b), and final device after backside liberation (c). The SMR-LWR is shown in the final state (d). The SEM picture shows a top view of a free LWR resonator with 150 IDT fingers, having reflectors of 40 fingers on both sides (e).

the e_{31} coefficient as well as the mix of elastic constants meet quite well reality. Small spurious modes were observed for all geometries, in both simulations and experiments. This seems to be one of the known drawbacks of free standing Lamb wave resonators [45, 184]. We did not consider the anchors and their contribution in loss mechanism in the FEM models, while in a real situation, these anchors are noticeable loss sources in LWRs [185]. This might explain why the experimental Q-factors are smaller than the predicted ones.

In experimental results small wiggles have been observed periodically every 11 MHz. The considerable point is that these ripples and their repeating frequency are identical in all devices, independent from IDTs width and operating frequency. Therefore, it must come from a source which is in common for all devices. All devices are fabricated on a 385μm thick silicon wafer. Considering the sound

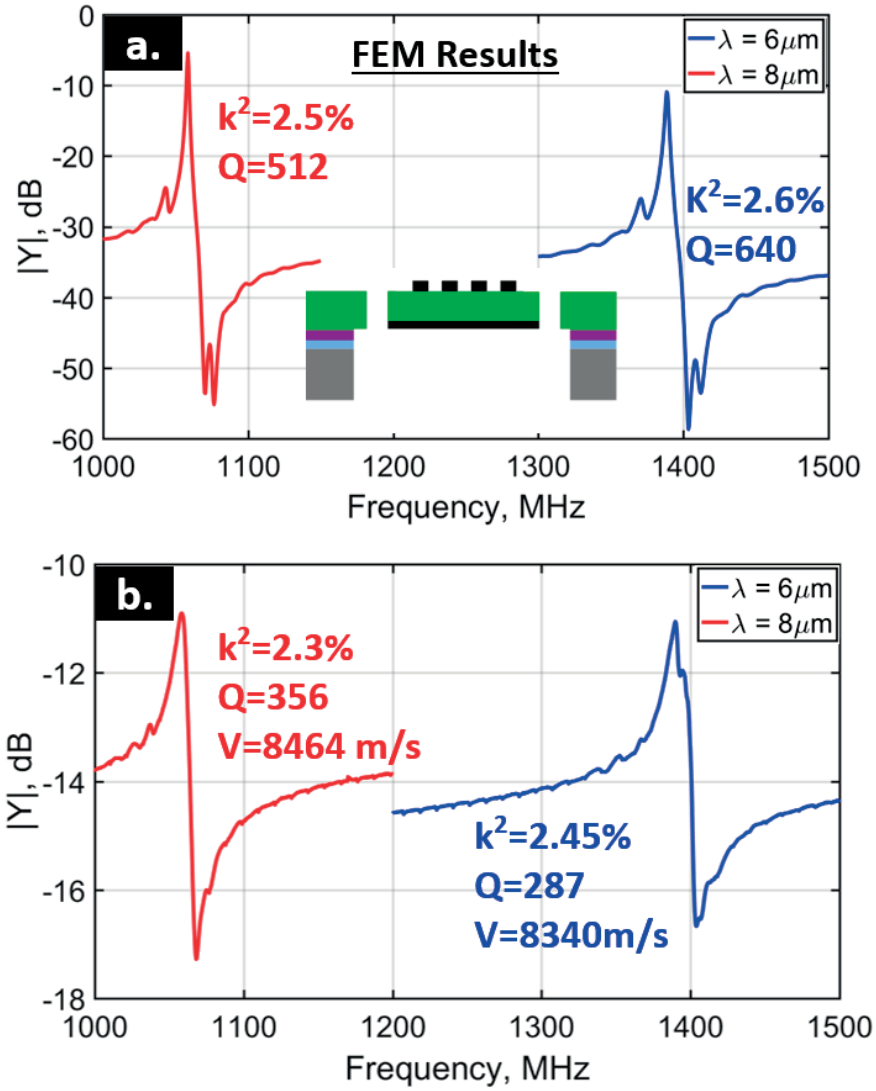

Figure 5.2: Absolute value of the admittance for free LWRs with 6 and 8 μm wavelengths. (a) FEM simulation; (b) Experimental result.

propagation velocity of 8440 m/s in the Si, gives BAW resonance frequency of 10.96 MHz for the 385μm Si cavity. Hence, one can say that the wiggles appear due to a small region with an overlap of the top and the bottom electrode in the anchor region above solid silicon, which leads to the excitation of standing bulk waves through the silicon substrate.

We also simulated the LWR S_0 modes of a free plate with periodic boundary conditions, hence for the case of LWRs extending to infinity (Figure 5.3). The phase

velocities of the measured devices fit very well to the theoretical values. However, the coupling constants differ quite a lot: The infinite model leads to a coupling of 4.5. to 4.7% in the h/λ range of 0.125-0.2. These values are about twice as high as obtained from FEM simulations of the real structure, and from the fabricated devices. The obvious difference between the infinity model and the one of the real structure are the reflectors, and the bus bars. It is interesting to note in this context that Yantchev and Katardjiev [178] reported that their realized resonators with reflectors had only a coupling of 1%, while the simple model with an infinite plate was calculated to have 2.5% coupling. This is a similar relative relation. The logical conclusion is that the reflectors are not working in an ideal way, and cost much more reactive energy than the Bragg reflector in an SMR-TFBAR, for which the lost coupling is almost negligible (about 0.2% of 6.7%).

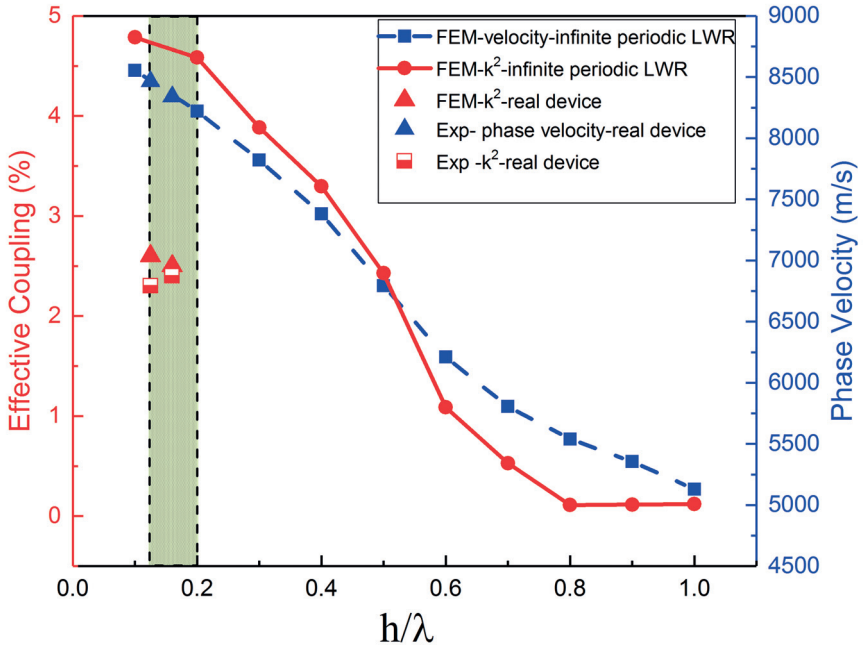

Figure 5.3: Phase velocity and coupling k^2 as a function of the h/λ for the Lamb wave mode S_0 in a h=1 μm thick $Al_{0.85}Sc_{0.15}N$ plate with interdigitated top electrodes and a floating bottom electrode. Periodic boundary conditions were applied. The two theoretical behaviors are compared with experimental data.

The results of the SMR-LWR devices are presented in Figure 5.4 The experimental coupling coefficient (k^2 of 2.29%) is slightly lower than with the free LWR,

but higher than FEM value of 2.14% obtained from FEM. Most remarkably, the quality factor of this SMR-LWR device is dramatically improved with respect to the freestanding structures, and reached a value of 1278. This Q factor is in fact close the predicted one. As a consequence, a very impressive FoM of nearly 30 is obtained. The relative difference in resonance frequencies is only 1.3%, indicating again a good choice of the involved elastic constants. The parasitic resonances observed in the FEM results, as well as those in the experimental ones are thought to stem from a non-ideal match of the SMR layers with the actual acoustic impedance of AlScN. The lower losses as compared to freestanding devices can be explained by the absence of anchors, and eventually also by the absence of couplings to the large number of structural resonances that are possible in a plate.

The FEM simulations show that the coupling coefficient of the SMR-LWR is relatively reduced by 12% as compared to the free LWR. Smaller degradation of this type are also known from thickness mode resonators (SMR-TFBAR) [23, 24]. These losses occur when the elastic waves in the Bragg structure are not entirely reflected back with the right phase into the active layer. From the experimental point of view, the performance of the device on the Bragg reflector shows very good agreement with what we expect from FEM. k^2 of 2.29% with quality factor equal to 1278, which yields a FOM of 29.3.

Conclusions

In this work, we fabricated Lamb wave resonators for the S_0 mode, based on 1 μm thick $Al_{0.85}Sc_{0.15}N$ thin films. The realized devices were of the membrane type (liberated from the Si substrate) and of the SMR type. The latter was built on a 5-layer W/SiO_2 Bragg reflector. In all cases, an excellent agreement was obtained between the predicted and measured characteristics with regard to resonance frequency and piezoelectric coupling. The quality factors of the SMR devices were found to be much larger than the ones of the free structures. We achieved a figure of merit of 29 (Q=1278, k^2=2.29%) at an operation frequency of 1430MHz, which is so far the best performance ever realized with a MEMS-type lamb wave resonator in this frequency range. The reason for the improved quality factor of the SMR device is not precisely known yet. However, it must be linked to obvious differences: the absence of bridges, and of competing plate modes when using a Bragg reflector as an acoustic insulator. Furthermore, it could also be that the lateral reflector gratings reflect the waves in a more coherent way back into the resonator. In the freestanding structures, there might also be some interferences between the reflector gratings and the borders of the suspended plate. Finite element simulations show in addition that the infinitely extended plate exhibits a twice higher coupling coefficient k^2 than a finite plate equipped with lateral

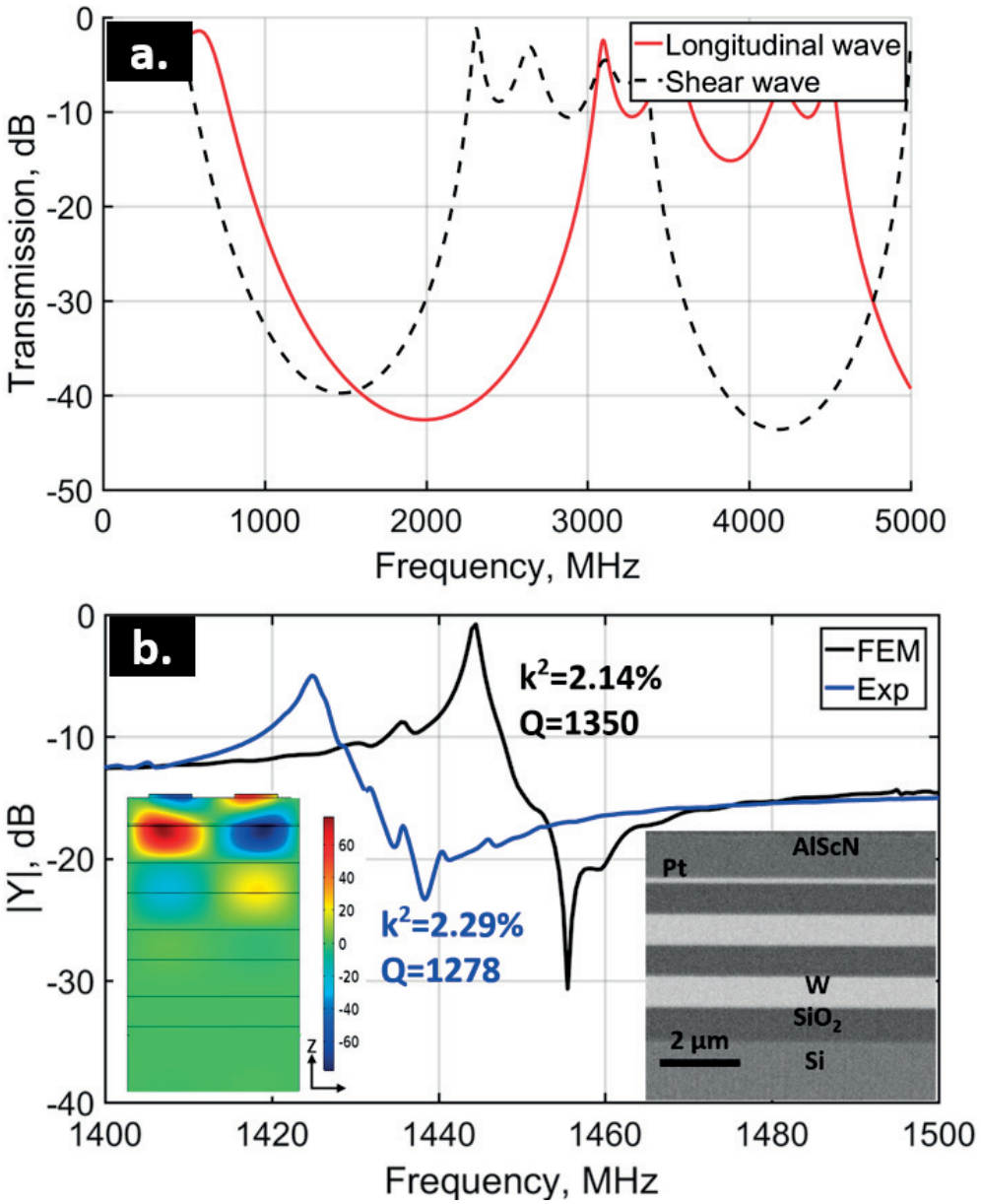

Figure 5.4: (a) Theoretical transmission of the Bragg mirror implemented in the fabricated devices, as derived by FEM. (b) The absolute value of the admittance of the SMR device obtained from FEM simulation and device measurement. The FEM cross section shows the size of the strain component S_z for the case of a two finger model with periodic boundary conditions. The SEM cross section was made at a FIB cut through a device.

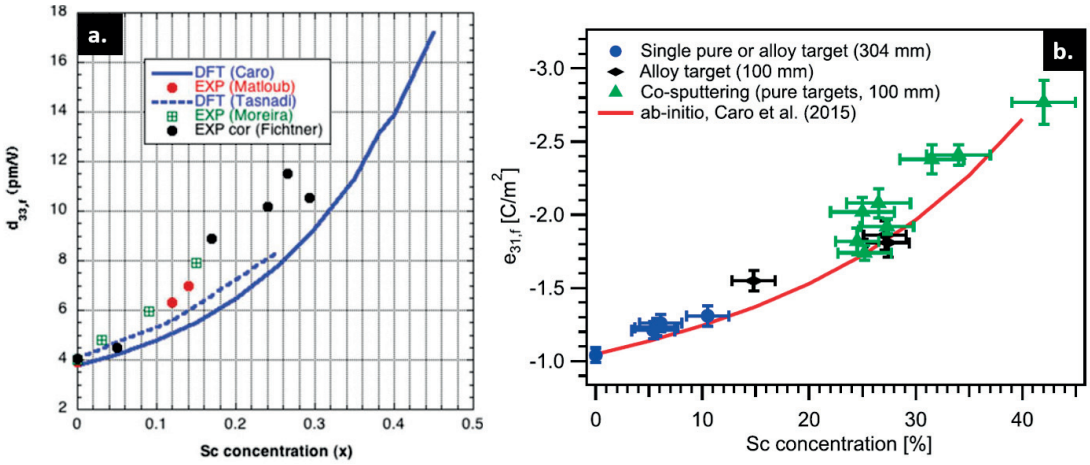

Figure 5.5: (a.) Longitudinal piezoelectric coefficient, $d_{33,f}$, as function of Sc concentration [61]. (b.) Transversal piezoelectric coefficient, $e_{31,f}$, as function of Sc concentration [128].

reflector gratings.

5.2 Solidly Mounted Lamb Wave Resonators with $Al_{0.7}Sc_{0.3}N$ Thin Film

Excellent performance of SM-LWRs with the 15% Sc AlScN film motivated us to fabricate SM-LWRs with 30% Sc film. Increasing the Sc content to 30% improves the $e_{33,f}$ and $d_{33,f}$ about 40% and 60% respectively, in comparison to 15% Sc AlScN film, and consequently expected to improve the coupling coefficient significantly (Figure 5.5). Konno already reported k^2 of 7% for LWR with 40% Sc film; however, the low Q of his devices resulted in FoM equal to 8 which is in the range of the pure AlN-LWRs performance [165]. Therefore, the SMR approach which boosts the Q while keeps the k^2 almost untouched, is of interest to achieve high performance (FoM) LWR devices which can satisfy the RF filter application requirements.

One challenge with the design of AlScN based devices with various Sc% concentration is the lack of sufficient experimental data regarding material parameters. This issue is more severe with higher Sc concentrations. Ab-initiation calculations are one of the main resources to provide the required data. In this project, our partner in IMTEK and CTR were responsible for providing the material parameters (calculated by DFT) and proposing designs of the devices, respectively. Two sets of materials parameters proposed (by our partner in IMTEK) for AlScN film with

30% Sc: $\rho = 3320Kg/m^3$,

$$
\begin{aligned}
c &= \begin{pmatrix} 282 & 122 & 144 & 0 & 0 & 0 \\ 122 & 282 & 144 & 0 & 0 & 0 \\ 144 & 144 & 253 & 0 & 0 & 0 \\ 0 & 0 & 0 & 104 & 0 & 0 \\ 0 & 0 & 0 & 0 & 104 & 0 \\ 0 & 0 & 0 & 0 & 0 & 80 \end{pmatrix} Gpa \\
e &= \begin{pmatrix} 0 & 0 & 0 & 0 & -0.35 & 0 \\ 0 & 0 & 0 & -0.35 & 0 & 0 \\ -0.72 & -0.72 & 2.24 & 0 & 0 & 0 \end{pmatrix} C/m \\
\varepsilon &= \begin{pmatrix} 18.9 & 0 & 0 \\ 0 & 18.9 & 0 \\ 0 & 0 & 20.5 \end{pmatrix}
\end{aligned}
\tag{5.1}
$$

and the second set is as follows:$\rho = 3320Kg/m^3$,

$$
\begin{aligned}
c &= \begin{pmatrix} 303 & 144 & 125 & 0 & 0 & 0 \\ 144 & 303 & 125 & 0 & 0 & 0 \\ 125 & 125 & 253 & 0 & 0 & 0 \\ 0 & 0 & 0 & 102 & 0 & 0 \\ 0 & 0 & 0 & 0 & 102 & 0 \\ 0 & 0 & 0 & 0 & 0 & 80 \end{pmatrix} Gpa \\
e &= \begin{pmatrix} 0 & 0 & 0 & 0 & -0.23 & 0 \\ 0 & 0 & 0 & -0.23 & 0 & 0 \\ -0.72 & -0.72 & 2.38 & 0 & 0 & 0 \end{pmatrix} C/m \\
\varepsilon &= \begin{pmatrix} 19 & 0 & 0 \\ 0 & 19 & 0 \\ 0 & 0 & 21 \end{pmatrix}
\end{aligned}
\tag{5.2}
$$

With these material parameters, our partner in CTR simulated LWR devices with different ratio of h/λ. They reported the best coupling, which is 5.09%, for the $\lambda = 5\mu$m and $h = 600$nm. Figure 5.6 shows the unit cell of the simulated structure which repeated with periodic boundary conditions. It means that the simulation results are representing a LWR with an infinite number of IDT. 50 nm Pt serves

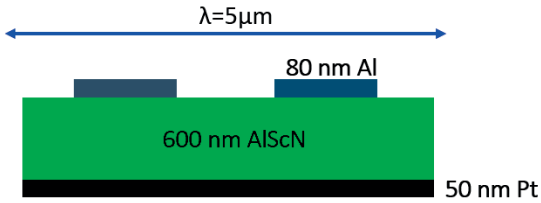

Figure 5.6: Unit cell of the LWR device with 30% Sc film used in FEM. A LWR with an infinite number of IDTs were modeled by applying a periodic boundary condition on this unit cell.

the floating bottom electrode and IDTs made of 80 nm thick Al. The S_0 mode resonance was expected to take place at 1397.68 MHz.

Two types of Bragg reflectors were employed. W/SiO_2 and AlN/SiO_2 which have acoustic impedance ratio for longitudinal wave (Z_L) of 7.9 and 3, respectively [13]. The higher Z_L of the alternating layers means that less number of layers are required to get the maximum reflection. Therefore, the W/SiO_2 mirror is preferred in this sense. However, the W is a conductive material; thus, it must be patterned (on the wafer) and confined just below the resonator cavity. Otherwise, it electrically connected all devices through the parasitic capacitances. Practically, one needs to make a photolithography and then an etching process for each W layer. The patterning of the W layer also produces shoulders (height difference) in the next SiO_2 layer. The shoulders must be avoided since their height will grow by deposition of the next pair (W/SiO_2), which can lead to film cracking in these regions. Chemical mechanical polishing (CMP) applied on SiO_2 layers to remove the shoulders and achieve a flat surface. These extra fabrication steps make the W/SiO_2 mirror more costly than the SiO_2/AlN mirror in which the layers are just deposited on each other. The number of the alternating layers and their thicknesses are calculated as it is explained in Section 5.1 by our partners in CTR. The highest coupling for the W/SiO_2 mirror is achieved when the R=0.3 with five layers (two layers of W) and for AlN/SiO_2 mirror, the highest coupling is achieved by seven layers (three layers of AlN) with R=1. Figure 5.7 shows the SEM cross-section of the fabricated Bragg reflectors and the corresponding transmission characterization.

FEM calculation, done by CTR, is used to simulate SM-LWR. To do so, the model of LWR unit cell (Figure 5.6) is defined on both types of Bragg mirrors with periodic boundary conditions. It means simulation results are representing a device with an infinite number of IDTs. Both sets of the material constants were used for the simulations. Table 5.1 presents simulations results.

As it was already observed with 15% Sc film LWRs, for 30% Sc devices, the

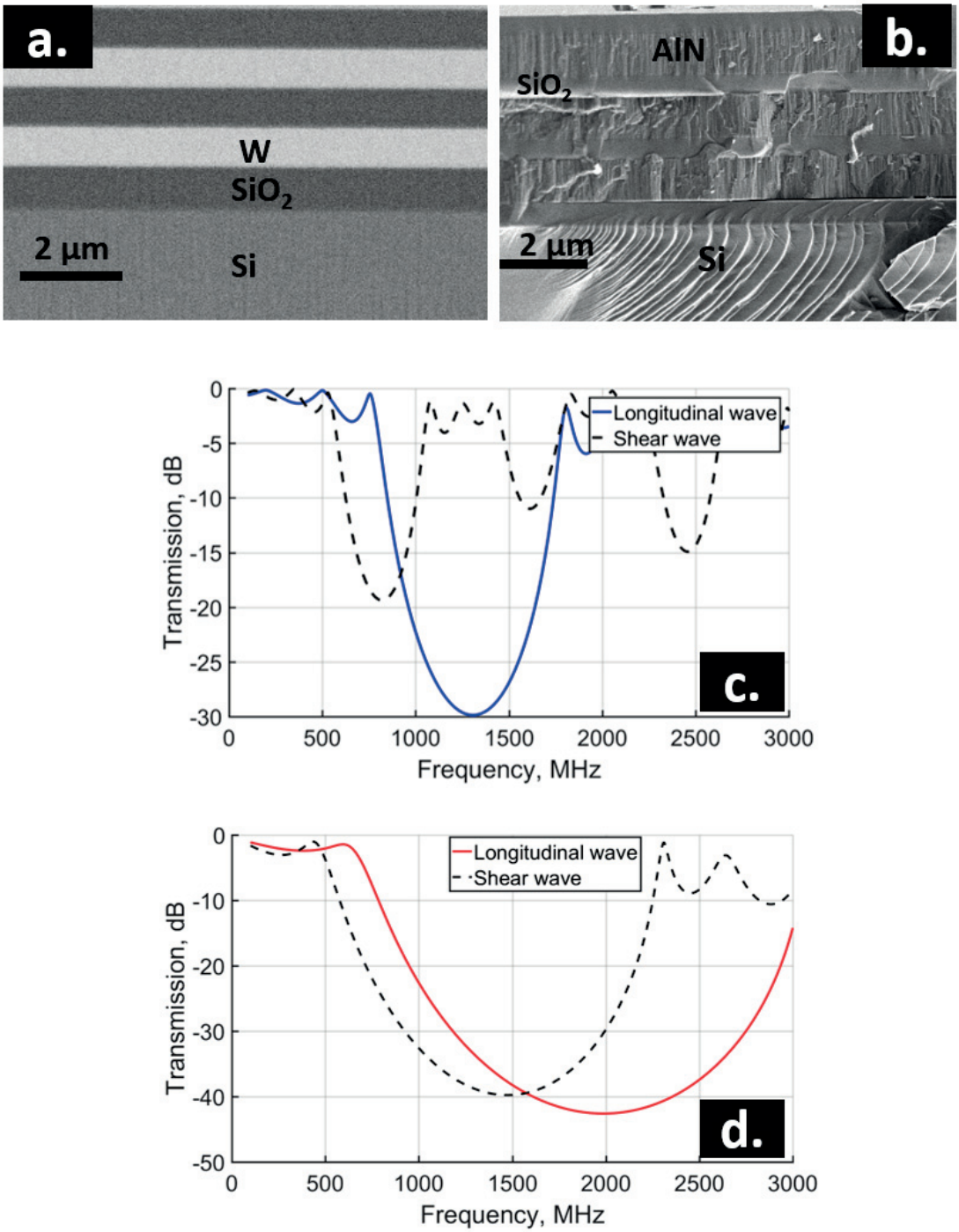

Figure 5.7: Cross section SEM images of Bragg reflectors. Bragg mirror includes (a.) Five layers of W/SiO_2. (b.) Seven layers of AlN/SiO_2. Transmission characteristic of the AlN/SiO_2 mirrors (c.) and W/SiO_2 mirror(d.).

Table 5.1: FEM results for the $Al_{0.7}Sc_{0.3}N$ based LWR devices with an infinite number of IDTs. Device unit cell depicted in Figure 5.6. Two sets of material constants were employed. The two last raws presents the experimental data of LWR with 300 IDTs, for more convenient comparison with FEM results.

LWR with infinite IDTs	F_r (MHz)	F_a(MHz)	k^2(%)	V (m/s)
Liberated(constants5.1)	1294.19	1338.23	6.58	6470
Liberated(constants5.2)	1397.68	1434.2	5.09	6988.4
On W/SiO_2 BM (constants5.1)	1362	1395.46	4.81	6810
On W/SiO_2 BM (constants5.2)	1440.99	1468.47	3.74	7205
On AlN/SiO_2 BM (constants5.1)	1323	1350	4.07	6615
On AlN/SiO_2 BM (constants5.2)	-	-	-	-
Exp with 300 IDT-AlN/SiO_2 BM	1269	1293	4.6	6345
Exp with 300 IDT-W/SiO_2 BM	1317	1345	5.2	6585

free standing type shows higher coupling coefficient than the SMR type (in FEM). As explained, the coupling reduction in SMRs takes place when elastic waves in the Bragg structure are not entirely reflected back with the correct phase into the active layer. However, the overall performance of SMR devices was significantly higher than free standing ones. Therefore, we just fabricated SMR-type devices with the 30% Sc film. It is also seen that (in Section 5.1) the k^2 of real devices were smaller than the simulated devices with an infinite number of IDTs. This issue originates from the fact that in the real device with limited numbers of IDTs, the wave does not trapped perfectly in the resonator plate. Thus, smaller k^2 is expected for the real structure with 30% Sc than what predicted by FEM (Table 5.1). It is also notable that the two types of Bragg reflectors do not show the same performance in FEM. The maximum efficiency for the W/SiO_2 mirror is achieved by five alternating layers (two layers of W), while seven layers is required for the AlN/SiO_2 mirror including three AlN layers. This comes from the fact that the acoustic impedance ratio on W/SiO_2 is around 2.7 times bigger than this ratio

at the AlN/SiO_2 interface [13]. Furthermore, the W/SiO_2 mirror shows attenuation around -40db for the both longitudinal and shear waves at the targeted resonance frequency (around 1400 MHz), while the AlN/SiO_2 mirror shows the attenuation around -30 db for the longitudinal wave and around -3db for the shear wave. See Figure 5.7. This results in higher coupling for the LWR on the W/SiO_2 mirror than the LWR on the AlN/SiO_2 mirror. The device on the AlN/SiO_2 mirror has lower resonance frequency than the device on W/SiO_2. It is due to the thicker SiO_2 layer below the Pt bottom electrode in AlN/SiO_2 mirrors, which acts as a mass loading on the resonator.

Real devices consist of 100, 200, and 300 IDTs which confined with 60 shorted reflectors on sides. The fabrication process is identical as what explained for SM-LWR with 15% Sc film.(Figure 5.1). Figure 5.8 shows a top view SEM image of a fabricated device.

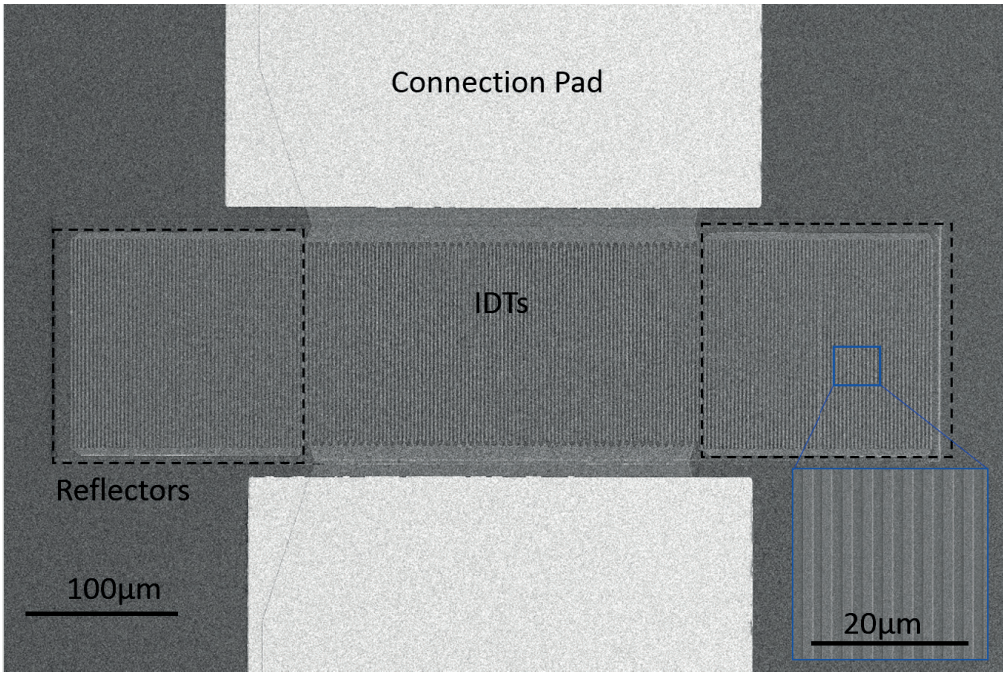

Figure 5.8: SEM image of an SM-LWR with 30% Sc AlScN film with 200 IDTs and 60 reflectors on sides.

As FEM predicted, LWR on the W/SiO_2 shows higher coupling and consequently higher FoM than the devices on the AlN/SiO_2 mirror. For both types of Bragg mirrors, devices with 300 IDTs show the best performance. Figure 5.9 shows the admittance characteristic of LWR devices with 300 IDTs on both types of Bragg mirrors. The impressive FoMs of 70 and 59 were achieved for the LWRs on W/SiO_2

and AlN/SiO_2 Bragg mirrors, respectively. To the best of author's knowledge, these values are by far the highest performance for MEMS-type LWRs which has been reported so far.

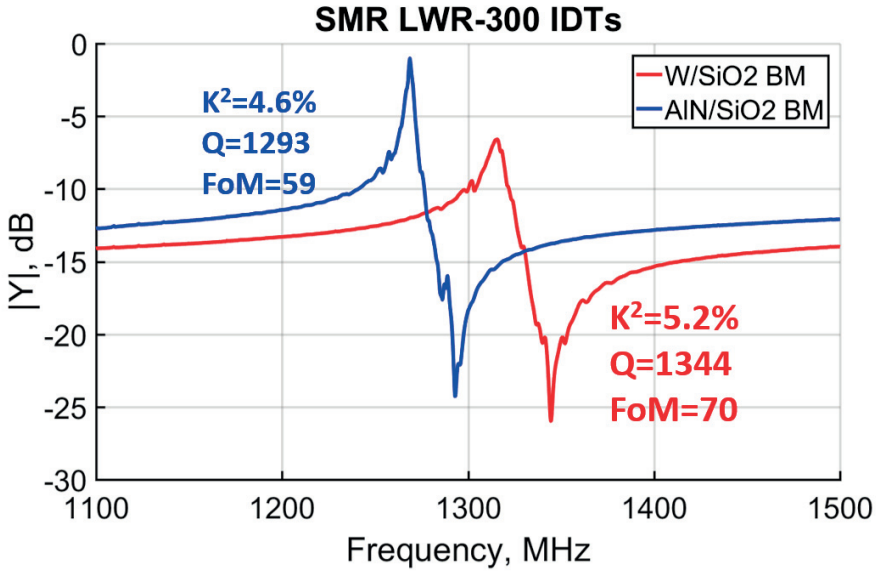

Figure 5.9: Admittance characteristic of LWRs with 300 IDTs on both types of Bragg mirrors. LWR on W/SiO_2 mirror shows higher coupling and FoM.

Decreasing the number of IDTs, reduces the FoM. One should notice that the wavelength is defined by IDTs, therefore reducing the number of them can result in broadening the wavelength of the excited wave. That's why reducing IDTs number usually reduces the quality factor and increases the coupling. As it is seen in Figure 5.10, the device with 100 IDts shows higher coupling than the device with 200 IDTs, which shows higher coupling than the device with 300 IDts.

The resonance frequency of the real device (with 300 IDTs) is smaller than what predicted by FEM with both sets of material constants (Table 5.1). It can show that the stiffness constants might be overestimated in DFT calculations. On the other hand, the coupling coefficients of real devices are bigger than the couplings of FEM, even though, the LWRs in FEM models have an infinite number of IDTs and real devices have 300 IDTs. It seems that the piezoelectric coefficients, e, are underestimated in DFT results. The noticeable point is that these mismatches in resonance frequency and coupling were not the case for the device with 15% Sc film. One can suggest, DFT calculation gets larger deviation from real values in high Sc content.

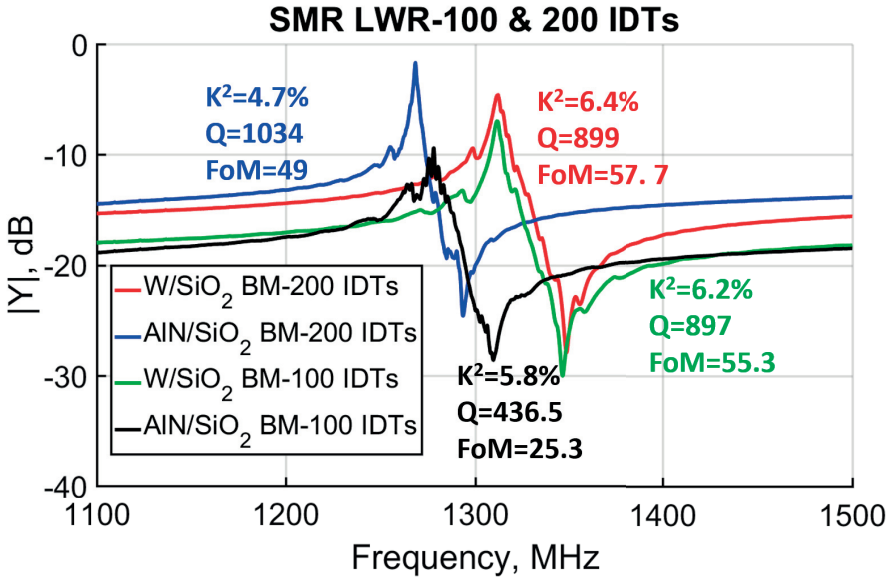

Figure 5.10: Admittance characteristic of LWRs with 200 and 100 IDTs on both types of Bragg mirrors. Decreasing the number of IDTs, reduces Q and FoM.

Chapter 6

Summary and Outlook

6.1 Summary

In this thesis, we study the potential of AlScN based Lamb wave resonators for RF filter applications. We fabricated LWRs with 15% and 30% Sc AlScN thin films. Design of the devices was delivered by the project collaborators at CTR. Firstly, we made free standing LWRs with 1μm thick AlScN thin film containing 15% of Sc. Wavelengths (λ) of 6 and 8 μm were chosen according to the FEM dispersion curves calculation. These wavelengths showed highest electromechanical coupling (k^2) in the affordable limits of our microfabrication facilities. An excellent agreement between the FEM predictions and measured characteristics with regard to resonance frequency and piezoelectric coupling was obtained. The k^2 values were around 2.5% which is 2.5 times higher than k^2 of the AlN based LWRs in the archival literature. This improvement clearly shows the enhanced piezoelectric response of Sc doped AlN. However, the moderate quality factor in the range of 200 to 400, results in the FoM to be around 8, which is the typical reported value for Al(Sc)N based LWR in the literature. In the next step, we employed a five layer Bragg reflector (SiO_2/W/SiO_2/W/SiO_2) to make solidly mounted (SM)-LWR. This improved the quality factor significantly without severe reduction of k^2. We achieved a FoM equal to 30 (Q = 1300 and k^2 = 2.3%) at the resonance frequency of 1400 MHz which is the highest reported value to the best of our knowledge.

In the next step, we increased the Sc content to 30% ($Al_{0.70}Sc_{0.30}N$) to achieve higher FoM and furtherer improvement of the k^2. FEM simulation predicted the best performance for the 600 nm thick film with $\lambda = 5\mu$m. We also employed a new type of Bragg reflector beside the SiO_2/W mirror. The new Bragg reflector contained seven layers of SiO_2 and AlN (SiO_2/AlN/SiO_2/AlN/SiO_2/AlN/SiO_2). The fabrication process of this mirror is easier and cheaper, but it is not as efficient

as the W/SiO_2 mirror. Results are unprecedented for LWRs. LWR on the W/SiO_2 mirror gave FoM of 70, Q of 1350 and k^2 of 5.2% , and LWR on the AlN/SiO_2 mirror gave FoM of 59, Q of 1300 and k^2 of 4.6% .

The reason for the improved quality factor of the SMR device is not precisely known yet. However, it must be linked to some obvious differences: the absence of bridges, and of competing plate modes when using a Bragg reflector as an acoustic insulator. Furthermore, it could also be that the lateral reflector gratings reflect the waves in a more coherent way back into the resonator. In the free-standing structures, there might also be some interferences between the reflector gratings and the borders of the suspended plate.

FEM prediction was quite accurate for the LWRs with 15% Sc film. However, there was a mismatch between the experimental results for the LWR with 30% Sc film and the FEM predictions. This difference comes from the values of the material constants used in FEM models. For 15% Sc film, the material parameters are extracted from the shape resonators characterization, which is one of the most accurate way to obtain material constants. Whereas, in the case of the 30% Sc film, the constants are obtained from DFT calculations.

The design of piezoelectric MEMS devices generally requires a full set of elastic, dielectric, and piezoelectric material constants. This issue is more severe for the complex mode resonators such as Lamb waves. Exciting pure mode resonances is one the most precise methods to obtain material parameters. We have done this for 15% Sc AlScN thin film through the design, fabrication, and characterization of shape resonators, including dual-mode thickness extensional and thickness shear mode resonator, radius extensional mode resonators and length-extensional mode resonators. In this work, we characterized the dual mode thickness extensional and thickness shear mode resonator to extracted the material parameters c_{33}, c_{44}, e_{33}, e_{15}, and ε_{33} for the $Al_{0.85}Sc_{0.15}N$ thin film. A 3.5° tilting of the c-axis in the c-textured film resulted in the excitation and appearance of the shear mode resonance in addition to the longitudinal mode (dual mode). As the film did not grow in the planned (0001) texture throughout the whole thickness, a novel approach had to be adopted for property determination. The large tilt angles of the grains in the upper part of the film were assessed by TEM nano-diffraction combined with Automated Crystal Orientation Mapping. A finite element model (2.5D FEM) was constructed having in a second layer the misaligned grains with the orientations as found in TEM, and represented with the same volume fractions. The electrical impedance was calculated and fitted to the experimental impedance measured as a function of frequency. The constants c_{33}^E and e_{33} were determined from the basic longitudinal mode and c_{44}^E, and e_{15} were calculated from the basic shear mode. This method allowed also to make a statement about the overall piezoelectric activity of the upper layer with the misaligned grains. The latter pick-up the polarity from the

first layer, meaning that the polar axis is tilted up to 90 °, but not beyond. It is not clear whether this relation is caused by the secondary nucleation process, or caused by other growth conditions, like the on bombardment. The low longitudinal coupling in the misaligned layer originates mostly from the large tilt angles, and not from (hypothetical) grains that would have inverted polarity. Such a model yielded clearly much lower coupling coefficients. This was also the case for an analytical model considering a double layer with a passive upper layer. The final values giving the best fit to experiment are: c_{33}^E = 277 GPa, c_{44}^E = 101 GPa, e_{33} = 1.88 C/m^2, e_{15} = 0.40 C/m^2, ε_{33} = 14.1 and ρ = 3280 kg/m^3 for the investigated film with 15% Sc. These values agree within about 10% with the ab-initio values adjusted to the AlN endpoint, whereby the elastic constants fit better to the non-adjusted ab-initio values. The experimental piezoelectric constants turned out to be larger than the ones delivered by ab-initio calculations. The radius extensional mode and length-extensional mode resonators characterized by our collaborators in IMTK. The extracted the consonants are c_{11}^E = 343 GPa, c_{12}^E = 171 GPa, c_{13}^E = 110 GPa and e_{31}= -0.63 C/m^2.

Growing high quality c-textured piezoelectric AlScN film is an absolute need for all AlScN based piezoelectric MEMS devices. One of the recently observed challenges to obtain such a film is the growth of abnormal grains (AOG) which do not have the (0002) texture. In this work, we study nucleation and growth of these grains. The presence of the AOG in AlScN films leads to a partial or total loss of the c-axis texture in the surface layer of the films. Many of the AOGs have c-axis tilts of 50°to 90°. They nucleate during the growth at grain boundaries between the (0001)-oriented grains, which dominate growth initially. Hyper-Map EDX studies allowed us to prove a segregation of the Sc at grain boundaries between such grains, at least in some cases, with an indication that this concentration is higher when the relative in-plane mismatch between neighboring grains is larger. It is plausible that larger Sc concentrations may lead to the nucleation of the cubic rocksalt structure akin to a complexion phase. As such embryonic nuclei cannot persist to stay in the rocksalt structure when approaching the average composition at a larger grain size, they revert to the wurtzite phase. This mechanism leads to a loss of the original orientation. It even appears that a large tilt of the c-axis away from the vertical direction is more favorable. AOGs grow faster than the c-oriented grains. The proposed growth mechanism to break the overall (0001)-texture considers the formation of a rocksalt nucleus in the Sc-rich complexion present at the grain interface between normal grains. In summary, the AOG growth mechanism consists of four consecutive steps:

- Sc accumulation between grains with a bad match of in-plane orientation.
- Formation of a rocksalt complexion layer with a Sc rich composition.

- Secondary nucleation and growth of wurtzite AOGs from the complexion interface
- Faster growth of AOGs because they obtain a higher incoming flux.

The conversion of the planar complexion into a vertical one at high-energy grain boundaries is at the origin of AOG growth mechanism: the Sc enriched surface layer created by preferential absorption of Al in the wurtzite phase generates at their side walls Sc-rich complexions in rocksalt phase which constitute the nuclei for AOGs. We also showed the importance of the material density and the roughness at grain boundaries. Smoother films with more coherent grain boundaries leave no space for impurity attachment and do not lead to AOGs, whereas badly matched, open grain boundaries promote Sc segregation and the nucleation of AOGs.

6.2 Outlook

In this work we advanced in processing, material characterization, and novel devices in relation with the use of AlScN thin films. We could show that the higher piezoelectric coupling offered by this material allows for new device principles, and potentially opens many new applications. Yet the work also showed the technological difficulties with this material. In the field of Lamb wave devices, we obtained very good and interesting results, but we also see that we do not understand everything, and much work is still to do for further improvements.

In thin film growth, still some work is needed to eliminate completely the occurrence of abnormally oriented grains. We have seen that electrical properties of the growth substrate play a role. But the issue is more complex. It includes surface roughness, all parameters of the sputtering process, the vacuum quality and certainly also the architecture of the process chamber with the magnetron. Further improvements must thus also include contributions from the suppliers of the sputter tools.

A big obstacle for achieving high resolution devices for micro sonics is the absence of a good dry etching process for AlScN thin films. Ion beam etching (IBE) has simply not enough selectivity with masking materials for realizing structures with an aspect ratio of one. What would be interesting is a process combining chemical dry etching with IBE. Such tools do not exist yet. However, with a growing market for AlScN, some suppliers of etching tools might work on this topic.

There are a number of open questions about the LWR. FEM results indicate that the LWRs with lateral grating type reflectors systematically show less coupling than the ones with an infinite number of IDTs. This shows that the reflectors

are not efficient in trapping the wave inside the resonator cavity. Design of the reflectors employed in this work was obtained from standard test designs for SAW devices. Finding the most efficient way to trap the Lamb wave inside the resonator plate still needs to be investigated. Open questions in the topic are: the efficiency of employing grating type reflectors vs free edges. Regarding the grating type reflectors, what is the optimum electrical connection? What would be the effect of the electrical connection on the stiffness constants and consequently on the optimum width of fingers to reflect the correct wavelength?

We have seen that FEM simulations which used the material parameters obtained from the shape resonators characterization, fitted quite well with experimental results (15% Sc- LWRs) unlike the case for the film with 30% Sc where the material constants were obtained from DFT calculations. It seems that the accuracy of DFT calculations is not maintained when the Sc content increases. Extracting material parameters from shape resonators led to promising results. Therefore, this method is advised for extracting the relevant parameters for the AlScN compositions of interest (i.e., 30% and 40% Sc).

Appendix

A.

Mathematics of shear and longitudinal waves in a tilted piezoelectric wurtzite structure

The properties of a crystal plate of a hexagonal (6mm) wurtzite structure having a tilted c-axis with respect to the plate normal by an angle of θ is derived from tensors obtained after a rotation by the angle θ for instance around the y-axis. The form of stiffness, piezoelectric, and dielectric tensors are given in the main text (Equation (4.6)). Mathematically speaking, this rotation means a transformation with the following matrices:

$$\boldsymbol{\varepsilon}' = \mathbf{A}\cdot\boldsymbol{\varepsilon}\cdot\mathbf{A}^T;\ \mathbf{C}' = \mathbf{M}\cdot\mathbf{C}\cdot\mathbf{M}^T;\ \mathbf{e}' = \mathbf{A}\cdot\mathbf{e}\cdot\mathbf{M}^T \tag{1}$$

Where:

$$\mathbf{A} = \begin{pmatrix} \cos\theta & 0 & -\sin\theta \\ 0 & 1 & 0 \\ \sin\theta & 0 & \cos\theta \end{pmatrix},$$

$$\mathbf{M} = \begin{pmatrix} A_{11}^2 & A_{12}^2 & A_{13}^2 & 2A_{12}A_{13} & 2A_{11}A_{13} & 2A_{11}A_{12} \\ A_{21}^2 & A_{22}^2 & A_{23}^2 & 2A_{22}A_{23} & 2A_{21}A_{23} & 2A_{22}A_{22} \\ A_{31}^2 & A_{32}^2 & A_{33}^2 & 2A_{32}A_{33} & 2A_{31}A_{33} & 2A_{31}A_{32} \\ A_{21}A_{31} & A_{22}A_{32} & A_{23}A_{33} & A_{22}A_{33}+A_{23}A_{32} & A_{21}A_{33}+A_{23}A_{31} & A_{21}A_{32}+A_{22}A_{31} \\ A_{11}A_{31} & A_{12}A_{32} & A_{13}A_{33} & A_{12}A_{33}+A_{13}A_{32} & A_{11}A_{33}+A_{13}A_{31} & A_{11}A_{32}+A_{12}A_{31} \\ A_{11}A_{21} & A_{12}A_{22} & A_{13}A_{23} & A_{12}A_{23}+A_{13}A_{22} & A_{11}A_{23}+A_{13}A_{21} & A_{11}A_{22}+A_{12}A_{21} \end{pmatrix} \tag{2}$$

Important note. Here and below, where there is no special notice, the elastic stiffness components are understood as the ones at the constant electric field c_{kl}^E .

For the velocities calculation we have to solve the differential equations which describe the coupled electro-elastic wave propagation in a piezoelectric medium:

$$\begin{cases} c_{ilmn}\dfrac{\partial^2 U_m}{\partial x_l \partial x_n} + e_{mil}\dfrac{\partial^2 \varphi}{\partial x_l \partial x_m} = \rho\dfrac{\partial^2 U_i}{\partial^2 t}, \\ e_{ilm}\dfrac{\partial^2 U_l}{\partial x_i \partial x_m} - \varepsilon_{il}\dfrac{\partial^2 \varphi}{\partial x_i \partial x_l} = 0 \end{cases} (i,l,m,n = 1,2,3), \qquad (3)$$

where U_m – mechanical displacement, e_{ilm} –piezoelectric tensor, c_{ilmn} – elastic moduli, ε_{il} – permittivity, ρ – material density, φ – electrical potential.

The amplitudes are of the form $U_i = \left(A_i e^{-jk_i Z} + B_i e^{jk_i Z}\right)e^{j\omega t}$, where, A_i, B_i are unknown amplitudes, Z is the coordinate perpendicular to the crystal plate, k_i the wavenumber, ω the angular frequency, j the imaginary number and t is the time. For a wave propagation in the Z direction, Equation (3) can be simplified to a one-dimensional form:

$$\begin{cases} \dfrac{\partial^2}{\partial z^2}\left(c'_{55}U_1 + c'_{54}U_2 + c'_{53}U_3 + e'_{35}\varphi\right) + \rho\omega^2 U_1 = 0, \\ \dfrac{\partial^2}{\partial z^2}\left(c'_{45}U_1 + c'_{44}U_2 + c'_{43}U_3 + e'_{34}\varphi\right) + \rho\omega^2 U_2 = 0, \\ \dfrac{\partial^2}{\partial z^2}\left(c'_{35}U_1 + c'_{34}U_2 + c'_{33}U_3 + e'_{33}\varphi\right) + \rho\omega^2 U_3 = 0, \\ \dfrac{\partial^2}{\partial z^2}\left(e'_{35}U_1 + e'_{34}U_2 + e'_{33}U_3 - \varepsilon'_{33}\varphi\right) = 0 \end{cases} \qquad (4)$$

The last line in Equation (4) can be rewritten as: $\dfrac{\partial^2 \varphi}{\partial z^2} = \dfrac{e'_{35}}{\varepsilon'_{33}}\dfrac{\partial^2 U_1}{\partial z^2} + \dfrac{e'_{34}}{\varepsilon'_{33}}\dfrac{\partial^2 U_2}{\partial z^2} + \dfrac{e'_{33}}{\varepsilon'_{33}}\dfrac{\partial^2 U_3}{\partial z^2}$. Replacing $\dfrac{\partial^2 \varphi}{\partial z^2}$ in Equation (4), this one can be written as:

$$\begin{cases} \left(c'_{55} + \dfrac{\left(e'_{35}\right)^2}{\varepsilon'_{33}}\right)\dfrac{\partial^2 U_1}{\partial z^2} + \left(c'_{54} + \dfrac{e'_{35}e'_{34}}{\varepsilon'_{33}}\right)\dfrac{\partial^2 U_2}{\partial z^2} + \left(c'_{35} + \dfrac{e'_{35}e'_{33}}{\varepsilon'_{33}}\right)\dfrac{\partial^2 U_3}{\partial z^2} + \rho\omega^2 U_1 = 0 \\ \left(c'_{45} + \dfrac{e'_{34}e'_{35}}{\varepsilon'_{33}}\right)\dfrac{\partial^2 U_1}{\partial z^2} + \left(c'_{44} + \dfrac{\left(e'_{34}\right)^2}{\varepsilon'_{33}}\right)\dfrac{\partial^2 U_2}{\partial z^2} + \left(c'_{43} + \dfrac{e'_{34}e'_{33}}{\varepsilon'_{33}}\right)\dfrac{\partial^2 U_3}{\partial z^2} + \rho\omega^2 U_2 = 0 \\ \left(c'_{35} + \dfrac{e'_{33}e'_{35}}{\varepsilon'_{33}}\right)\dfrac{\partial^2 U_1}{\partial z^2} + \left(c'_{34} + \dfrac{e'_{33}e'_{34}}{\varepsilon'_{33}}\right)\dfrac{\partial^2 U_2}{\partial z^2} + \left(c'_{33} + \dfrac{\left(e'_{33}\right)^2}{\varepsilon'_{33}}\right)\dfrac{\partial^2 U_3}{\partial z^2} + \rho\omega^2 U_3 = 0 \end{cases} \qquad (5)$$

In matrix form, this set of equations reads as:

$$\begin{pmatrix} c'_{55}+\dfrac{(e'_{35})^2}{\varepsilon'_{33}} & c'_{54}+\dfrac{e'_{35}e'_{34}}{\varepsilon'_{33}} & c'_{35}+\dfrac{e'_{35}e'_{33}}{\varepsilon'_{33}} \\ c'_{45}+\dfrac{e'_{34}e'_{35}}{\varepsilon'_{33}} & c'_{44}+\dfrac{(e'_{34})^2}{\varepsilon'_{33}} & c'_{43}+\dfrac{e'_{34}e'_{33}}{\varepsilon'_{33}} \\ c'_{35}+\dfrac{e'_{33}e'_{35}}{\varepsilon'_{33}} & c'_{34}+\dfrac{e'_{33}e'_{34}}{\varepsilon'_{33}} & c'_{33}+\dfrac{(e'_{33})^2}{\varepsilon'_{33}} \end{pmatrix} \cdot \frac{\partial}{\partial Z}\begin{pmatrix} U_1 \\ U_2 \\ U_3 \end{pmatrix} + \begin{pmatrix} \rho\omega^2 & 0 & 0 \\ 0 & \rho\omega^2 & 0 \\ 0 & 0 & \rho\omega^2 \end{pmatrix} \cdot \begin{pmatrix} U_1 \\ U_2 \\ U_3 \end{pmatrix} = 0 \qquad (6)$$

Inserting the functions of $U_i = \left(A_i e^{-jk_i Z} + B_i e^{jk_i Z}\right)$ and their derivatives, knowing that $k_i=\omega/V$ and taking into account the symmetry of the problem, we obtain:

$$\begin{pmatrix} c'_{55}+\dfrac{(e'_{35})^2}{\varepsilon'_{33}}-\rho V^2 & 0 & c'_{35}+\dfrac{e'_{35}e'_{33}}{\varepsilon'_{33}} \\ 0 & c'_{44}-\rho V^2 & 0 \\ c'_{35}+\dfrac{e'_{33}e'_{35}}{\varepsilon'_{33}} & 0 & c'_{33}+\dfrac{(e'_{33})^2}{\varepsilon'_{33}}-\rho V^2 \end{pmatrix} \cdot \begin{pmatrix} k_1^2\left(A_1 e^{-jk_1 z}+B_1 e^{jk_1 z}\right) \\ k_2^2\left(A_2 e^{-jk_2 z}+B_2 e^{jk_2 z}\right) \\ k_3^2\left(A_3 e^{-jk_3 z}+B_3 e^{jk_3 z}\right) \end{pmatrix} = 0 \quad (7)$$

Equation (7) has a nontrivial solution when the determinant of the left matrix is zero.

Solving the system of the linear Equations (7) we obtain the solutions for velocity:

$$V_L = \sqrt{\frac{c_{33}^D + c_{55}^D}{2\rho} + \sqrt{\left(\frac{c_{33}^D - c_{55}^D}{2\rho}\right)^2 + \left(\frac{c_{35}^D}{\rho}\right)^2}}; \quad V_{S_1} = \sqrt{\frac{c'_{44}}{\rho}}; V_{S_2} = \sqrt{\frac{c_{33}^D + c_{55}^D}{2\rho} - \sqrt{\left(\frac{c_{33}^D - c_{55}^D}{2\rho}\right)^2 + \left(\frac{c_{35}^D}{\rho}\right)^2}} \quad (8)$$

where $c_{55}^D = c'_{55} + \dfrac{(e'_{35})^2}{\varepsilon'_{33}}$; $c_{35}^D = c'_{35} + \dfrac{e'_{35}e'_{33}}{\varepsilon'_{33}}$; $c_{33}^D = c'_{33} + \dfrac{(e'_{33})^2}{\varepsilon'_{33}}$ are stiffened elastic constants in the rotated coordinate system. From Equation (8) we can see that the velocities V_L and V_{S_2} are depending on piezoelectric coefficients. Effective piezoelectric constants for the two piezoactive quasi-longitudinal and quasi-shear waves V_L and V_{S_2} respectively, can be determined by the calculation of the unknown amplitudes *A* and *B,* and the angle α between the quasi-longitudinal wave displacement U_3 and the *Z* axis. We don't make here a long calculation, but give just the final result of Equation (8).

$$e_{eff}^L = e'_{35}\sin\alpha + e'_{33}\cos\alpha; \; e_{eff}^S = e'_{35}\cos\alpha - e'_{33}\sin\alpha$$

$$\tan(2\alpha) = \frac{2c_{35}^D}{c_{33}^D - c_{55}^D} \qquad (9)$$

More details can be found in ref. [170].

The effective electromechanical coupling factors for the quasi-longitudinal and quasi-shear wave are finally obtained as: $\left(k_{eff}^{L}\right)^2 = \frac{\left(e_{eff}^{L}\right)^2}{e'_{33}\rho V_L^2}; \left(k_{eff}^{S}\right)^2 = \frac{\left(e_{eff}^{S}\right)^2}{e'_{33}\rho V_S^2}$ (10)

B.

One dimensional model for the composite resonator

The one dimensional (1D) model of our structure is depicted in Figure 6 of the main text. It consists of the two stacked piezoelectric layers P_1 and P_2 with different crystallographic orientations. These piezoelectric layers form the composite transducer which is able to excite quasi-longitudinal and quasi-shear waves. The transducer mechanically loaded at the top and bottom boundaries. Each piezoelectric layer is considered as a three-port transducer (Figure 1) as described by Bloomfield [176].

On the acoustic port: $F = -AT$ is a mechanical force on the boundary, A is the area, T is stress, $U_n^- = \frac{\partial \xi_n(0)}{\partial t}$, $U_n^+ = \frac{\partial \xi_n(d_n)}{\partial t}$ are the particle velocities of the material, ξ_n is a displacement, d_n is the thickness of the n^{th} layer. The electrical port variables are the voltages at the layer boundaries, V_n^-, V_n^+, and the electrical currents I_n. The voltage applied across layer n is $V_n = V_n^- - V_n^+$.

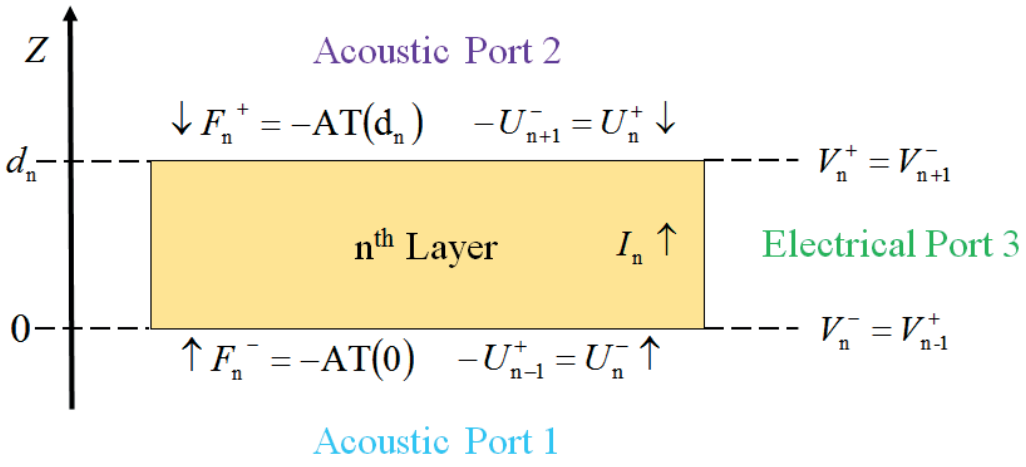

Figure 1. Boundary conditions of the n^{th} layer as a three-port element.

The variables at the bottom surface (–) of a layer are related to the variables at the top surface (+) by the transfer matrix **T**. The layers that are electrically connected in series have the common current *I*. Since the resonator is dual mode, one has to calculate the transfer matrix for the both quasi-shear (*S*) and quasi-longitudinal (*L*) wave. For a composite resonator consisting of the two piezoelectric layers with different orientations in general case it can be said:

$$\begin{pmatrix} \\ \left(F_{\mathrm{P}_2}^{+}\right)^{S,L} \\ \left(U_{\mathrm{P}_2}^{+}\right)^{S,L} \\ \left(V_{\mathrm{P}_2}^{+}\right)^{S,L} \\ I^{S,L} \end{pmatrix} = \mathbf{T}_{\mathrm{P}_2} \cdot \mathbf{T}_{\mathrm{P}_1} \begin{pmatrix} \\ \left(F_{\mathrm{P}_1}^{-}\right)^{S,L} \\ \left(-U_{\mathrm{P}_1}^{-}\right)^{S,L} \\ \left(V_{\mathrm{P}_1}^{-}\right)^{S,L} \\ I^{S,L} \end{pmatrix}, \qquad (11)$$

where $\mathbf{T}_{\mathrm{P}_1}$ and $\mathbf{T}_{\mathrm{P}_2}$ are the transfer matrixes for the piezolayer P_1 and P_2 respectively, and $V_0^{S,L} = \left(V_{\mathrm{P1}}^{-}\right)^{S,L} - \left(V_{\mathrm{P2}}^{+}\right)^{S,L}$ is the voltage between the bottom surface of the layer P_1 and top surface of the layer P_2.

$$\mathbf{T}_{\mathrm{P}} = \begin{pmatrix} \cos\beta_{\mathrm{P}}^{\mathrm{S,L}} & jZ_{\mathrm{P}}^{S,L}\sin\beta_{\mathrm{P}}^{\mathrm{S,L}} & 0 & -j\left(h_{\mathrm{P}}^{S,L}/\omega\right)\left(1-\cos\beta_{\mathrm{P}}^{\mathrm{S,L}}\right) \\ j\left(Z_{\mathrm{P}}^{S,L}\right)^{-1}\sin\beta_{\mathrm{P}}^{\mathrm{S,L}} & \cos\beta_{\mathrm{P}}^{\mathrm{S,L}} & 0 & -\left(h_{\mathrm{P}}^{S,L}/\omega\right)\left(Z_{P}^{S,L}\right)^{-1}\sin\beta_{\mathrm{P}}^{\mathrm{S,L}} \\ -\left(h_{\mathrm{P}}^{S,L}/\omega\right)\left(Z_{\mathrm{P}}^{S,L}\right)^{-1}\sin\beta_{\mathrm{P}}^{\mathrm{S,L}} & -j\left(h_{\mathrm{P}}^{S,L}/\omega\right)\left(1-\cos\beta_{\mathrm{P}}^{\mathrm{S,L}}\right) & 1 & j\left(1-\sigma_{\mathrm{P}}^{\mathrm{S,L}}\sin\beta_{\mathrm{P}}^{\mathrm{S,L}}\right)/\left(\omega C_{\mathrm{P}}^{0}\right) \\ 0 & 0 & 0 & 1 \end{pmatrix} \qquad (12)$$

Where: $\beta_{\mathrm{P}}^{\mathrm{S,L}} = \dfrac{\omega d_{\mathrm{p}}}{V_{S,L}}$, d_{P} is the thickness of the layer; $V_{S,L}$ are quasi-shear or quasi-longitudinal wave velocities defined in Equation 8. $C_{\mathrm{P}}^{0} = \dfrac{\mathrm{A}\varepsilon_{33}^{S}}{d_{\mathrm{P}}}$ is the static capacitance; *A* is the area of the layer and $\varepsilon_{33}^{\mathrm{S}}$ is permittivity at constant strain, $Z_{\mathrm{P}}^{S,L} = A\rho V_{S,L}$ is the acoustic impedance, calculated for a quasi-shear and quasi-longitudinal wave, respectively; $h_{\mathrm{P}}^{S,L} = \dfrac{e_{eff}^{S,L}}{\varepsilon_{33}^{\mathrm{S}}}$ is the piezoelectric coefficient for both waves and $\sigma_{\mathrm{P}}^{\mathrm{S,L}} = \dfrac{\left(k_{eff}^{L.S}\right)^2}{\beta}$.

Non-piezoelectric elastic (E) layers *Pt, Si_3N_4, SiO_2* have simplified transfer matrix of size 2×2 and obtained from the first 4 elements of the piezoelectric transfer matrix (13):

$$\mathbf{T}_{\mathrm{E}}=\begin{pmatrix}\cos\beta_{\mathrm{E}}^{\mathrm{S,L}} & jZ_{\mathrm{E}}^{S,L}\sin\beta_{\mathrm{E}}^{\mathrm{S,L}}\\ j\left(Z_{\mathrm{E}}^{S,L}\right)^{-1}\sin\beta_{\mathrm{E}}^{\mathrm{S,L}} & \cos\beta_{\mathrm{E}}^{\mathrm{S,L}}\end{pmatrix} \qquad (14)$$

Forces and partial velocity are identical at the bottom of the layer P_1 and top of the Pt electrode. Taking into account the layers beneath, we obtain:

$$\begin{pmatrix}\left(F_{\mathrm{P_1}}^{-}\right)^{S,L}\\ -\left(U_{\mathrm{P_1}}^{-}\right)^{S,L}\end{pmatrix}=\begin{pmatrix}\left(F_{\mathrm{Pt}}^{-}\right)^{S,L}\\ \left(-U_{\mathrm{Pt}}^{-}\right)^{S,L}\end{pmatrix}=\mathbf{T}_{Pt}\cdot\mathbf{T}_{Si_3N_4}\cdot\mathbf{T}_{SiO_2}\begin{pmatrix}\left(F_{SiO_2}^{+}\right)^{S,L}\\ \left(U_{SiO_2}^{+}\right)^{S,L}\end{pmatrix} \qquad (15)$$

For the top border of the layer P_2 and top *Pt* electrode:

$$\begin{pmatrix}\left(F_{\mathrm{P2}}^{+}\right)^{S,L}\\ \left(U_{\mathrm{P2}}^{+}\right)^{S,L}\end{pmatrix}=\begin{pmatrix}\left(F_{\mathrm{Pt}}^{-}\right)^{S,L}\\ \left(-U_{\mathrm{Pt}}^{-}\right)^{S,L}\end{pmatrix}=\mathbf{T}_{Pt}\begin{pmatrix}\left(F_{\mathrm{Pt}}^{+}\right)^{S,L}\\ \left(U_{\mathrm{Pt}}^{+}\right)^{S,L}\end{pmatrix} \qquad (16)$$

Because the top electrode's top border and bottom SiO_2 layer bottom border are on the air, the mechanical forces are equal to zero:

$$\left(F_{\mathrm{Pt}}^{+}\right)^{S,L}=0;\ \left(F_{\mathrm{SiO_2}}^{+}\right)^{S,L}=0 \qquad (17)$$

Substituting (17) to (16) and (15), one can calculate the acoustic impedances of the bottom and top layers respectively:

$$Z_{\mathrm{Bot}}^{\mathrm{S,L}}=\frac{\left(F_{\mathrm{P1}}^{-}\right)^{S,L}}{\left(U_{\mathrm{P1}}^{-}\right)^{S,L}}=jZ_{\mathrm{Pt}}^{S,L}\frac{Z_{\mathrm{SiO_2}}^{S,L}\left[Z_{\mathrm{Pt}}^{S,L}-Z_{\mathrm{Si_3N_4}}^{S,L}\cot\left(\beta_{\mathrm{Pt}}^{\mathrm{S,L}}\right)\cot\left(\beta_{\mathrm{Si_3N_4}}^{\mathrm{S,L}}\right)\right]-Z_{\mathrm{Si_3N_4}}^{S,L}\cot\left(\beta_{\mathrm{SiO_2}}^{\mathrm{S,L}}\right)\left[Z_{\mathrm{Si_3N_4}}^{S,L}\cot\left(\beta_{\mathrm{Pt}}^{\mathrm{S,L}}\right)+Z_{\mathrm{Pt}}^{S,L}\cot\left(\beta_{\mathrm{Si_3N_4}}^{\mathrm{S,L}}\right)\right]}{Z_{\mathrm{SiO_2}}^{S,L}\left[Z_{\mathrm{Pt}}^{S,L}\cot\left(\beta_{\mathrm{Pt}}^{\mathrm{S,L}}\right)+Z_{\mathrm{Si_3N_4}}^{S,L}\cot\left(\beta_{\mathrm{Si_3N_4}}^{\mathrm{S,L}}\right)\right]+Z_{\mathrm{Si_3N_4}}^{S,L}\cot\left(\beta_{\mathrm{SiO_2}}^{\mathrm{S,L}}\right)\left[Z_{\mathrm{Si_3N_4}}^{S,L}-Z_{\mathrm{Pt}}^{S,L}\cot\left(\beta_{\mathrm{Pt}}^{\mathrm{S,L}}\right)\cot\left(\beta_{\mathrm{Si_3N_4}}^{\mathrm{S,L}}\right)\right]}$$

$$Z_{\mathrm{Top}}^{\mathrm{S,L}}=\frac{\left(F_{\mathrm{P2}}^{+}\right)^{S,L}}{\left(U_{\mathrm{P2}}^{+}\right)^{S,L}}=jZ_{\mathrm{Pt}}^{S,L}\tan\left(\beta_{\mathrm{Pt}}^{\mathrm{S,L}}\right)$$

(18)

The electrical impedance of the composite resonator for shear and longitudinal mode:

$$Z^{S,L}=\frac{V_0^{S,L}}{I^{S,L}}=a_{34}-\frac{\left(a_{31}Z_{\mathrm{Bot}}^{\mathrm{S,L}}+a_{32}\right)\left(a_{24}Z_{\mathrm{Top}}^{\mathrm{S,L}}+a_{14}\right)}{a_{21}Z_{\mathrm{Top}}^{\mathrm{S,L}}Z_{\mathrm{Bot}}^{\mathrm{S,L}}+a_{22}Z_{\mathrm{Top}}^{\mathrm{S,L}}+a_{11}Z_{\mathrm{Bot}}^{\mathrm{S,L}}+a_{12}} \qquad (19)$$

where $a_{k,l}$ are elements of the matrix $\mathbf{A}=\mathbf{T}_{\mathrm{P_2}}\cdot\mathbf{T}_{\mathrm{P_1}}$, obtained from multiplying of the transfer matrices (13) of two layers.

The total electrical impedance of the composite dual mode resonator is:

$$Z_{\text{Total}} = Z^S + Z^L - \frac{i}{\omega C_0} \qquad (20)$$

where C_0 is the static capacitance of the transducer.

To avoid singularity in impedance calculations, a viscous loss is introduced to the stiffness constants as follows: $c_{kl} = c_{kl}^0 \left(1 + \frac{i}{2Q}\right)$ (21)

Where Q is assumed to be 1000. The finite Q leads to an imaginary part of the velocity.

Bibliography

[1] Jacques Curie and Pierre Curie. Développement par compression de l'électricité polaire dans les cristaux hémièdres à faces inclinées. *Bulletin de minéralogie*, 3(4):90–93, 1880.

[2] Malcolm E Lines and Alastair M Glass. *Principles and applications of ferroelectrics and related materials*. Oxford university press, 1977.

[3] Yuhuan Xu. *Ferroelectric materials and their applications*. Elsevier, 2013.

[4] Ramin Matloub Aghdam. Growth and properties of AlScNthin films for microwave transducers and piezoelectric energy harvesting. 2014.

[5] Klaus Prume, Paul Muralt, Florian Calame, Thorsten Schmitz-Kempen, and Stephan Tiedke. Piezoelectric thin films: Evaluation of electrical and electromechanical characteristics for mems devices. *IEEE transactions on ultrasonics, ferroelectrics, and frequency control*, 54(1), 2007.

[6] Stefan Mertin, Vladimir Pashchenko, Fazel Parsapour, Clemens Nyffeler, Cosmin S Sandu, Bernd Heinz, Oliver Rattunde, Gabriel Christmann, Marc-Alexandre Dubois, and Paul Muralt. Enhanced piezoelectric properties of c-axis textured aluminium scandium nitride thin films with high scandium content: Influence of intrinsic stress and sputtering parameters. In *Ultrasonics Symposium (IUS), 2017 IEEE International*, pages 1–4. Ieee, 2017.

[7] Robert Weigel, David P Morgan, John M Owens, Arthur Ballato, Kenneth M Lakin, Ken-Ya Hashimoto, and Clemens CW Ruppel. Microwave acoustic materials, devices, and applications. *IEEE Transactions on microwave theory and techniques*, 50(3):738–749, 2002.

[8] R. Aigner. Mems in RF filter applications: Thin-film bulk acoustic wave technology. *Sensors Update*, 12(1):175–210, 2003.

[9] Nurul Izza Mohd Nor, Kriyang Shah, Jugdutt Singh, and Zaliman Sauli. Design and analysis of wideband ladder-type film bulk acoustic wave resonator filters in ku-band. 2013, 06 2013.

[10] Lord Rayleigh. On waves propagated along the plane surface of an elastic solid. *Proceedings of the London Mathematical Society*, 1(1):4–11, 1885.

[11] RM White and FW Voltmer. Direct piezoelectric coupling to surface elastic waves. *Applied physics letters*, 7(12):314–316, 1965.

[12] David Morgan. *Surface acoustic wave filters: With applications to electronic communications and signal processing*. Academic Press, 2010.

[13] Tuomas Pensala et al. *Thin film bulk acoustic wave devices: Performance optimization and modeling*. VTT, 2011.

[14] PD Bradley, R Ruby, A Barfknecht, F Geefay, C Han, G Gan, Y Oshmyansky, and JD Larson. A 5 mm/spl times/5 mm/spl times/1.37 mm hermetic fbar duplexer for pcs handsets with wafer-scale packaging. In *Ultrasonics Symposium, 2002. Proceedings. 2002 IEEE*, volume 1, pages 931–934. IEEE, 2002.

[15] Gernot Fattinger, Alexandre Volatier, Robert Aigner, and Fabien Dumont. Baw pcs-duplexer chipset and duplexer applications. In *Ultrasonics Symposium, 2008. IUS 2008. IEEE*, pages 602–606. IEEE, 2008.

[16] Edgar Schmidhammer, Habbo Heinze, Monika Schmiedgen, Markus Mayer, and Andreas Link. 4d-2 high volume production of a fully matched 5050 pcs-cdma-baw duplexer. In *Ultrasonics Symposium, 2006. IEEE*, pages 329–332. IEEE, 2006.

[17] Hiroaki Satoh, Yasuo Ebata, Hitoshi Suzuki, and Choji Narahara. An air-gap type piezoelectric composite thin film resonator. In *39th Annual Symposium on Frequency Control. 1985*, pages 361–366. IEEE, 1985.

[18] Ken-ya Hashimoto. Baw piezoelectric resonators. In *Piezoelectric MEMS Resonators*, pages 203–220. Springer, 2017.

[19] Kiyoshi Nakamura, Hiromasa Sasaki, and Hiroshi Shimizu. A piezoelectric composite resonator consisting of a zno film on an anisotropically etched silicon substrate. *Japanese Journal of Applied Physics*, 20(S3):111, 1981.

[20] KM Lakin and JS Wang. Acoustic bulk wave composite resonators. *Applied Physics Letters*, 38(3):125–127, 1981.

[21] K. M. Lakin, J. S. Wang, G. R. Kline, A. R. Landin, Y. Y. Chen, and J. D. Hunt. Thin film resonators and filters. In *1982 Ultrasonics Symposium*, pages 466–475, Oct 1982.

[22] Rich Ruby. Micromachined cellular filters. In *Microwave Symposium Digest, 1996., IEEE MTT-S International*, volume 2, pages 1149–1152. IEEE, 1996.

[23] KM Lakin, KT McCarron, and RE Rose. Solidly mounted resonators and filters. In *Ultrasonics Symposium, 1995. Proceedings., 1995 IEEE*, volume 2, pages 905–908. IEEE, 1995.

[24] WE Newell. Face-mounted piezoelectric resonators. *Proceedings of the IEEE*, 53(6):575–581, 1965.

[25] Ken-ya Hashimoto. *RF bulk acoustic wave filters for communications*. Artech House, 2009.

[26] Kenneth M Lakin, Gerald R Kline, and Kevin T McCarron. High-q microwave acoustic resonators and filters. *IEEE transactions on microwave theory and techniques*, 41(12):2139–2146, 1993.

[27] Rich Ruby. 11e-2 review and comparison of bulk acoustic wave fbar, smr technology. In *Ultrasonics Symposium, 2007. IEEE*, pages 1029–1040. IEEE, 2007.

[28] S Marksteiner, J Kaitila, GG Fattinger, and R Aigner. Optimization of acoustic mirrors for solidly mounted baw resonators. In *Ultrasonics Symposium, 2005 IEEE*, volume 1, pages 329–332. IEEE, 2005.

[29] Abdelkrim Khelif, Mikael Wilm, Vincent Laude, Sylvain Ballandras, and B Djafari-Rouhani. Guided elastic waves along a rod defect of a two-dimensional phononic crystal. *Physical Review E*, 69(6):067601, 2004.

[30] G Carlotti, FS Hickernell, HM Liaw, L Palmieri, G Socino, and E Verona. The elastic constants of sputtered aluminum nitride films. In *Ultrasonics Symposium, 1995. Proceedings., 1995 IEEE*, volume 1, pages 353–356. IEEE, 1995.

[31] Joel Rosenbaum. *Bulk acoustic wave theory and devices*. Artech House on Demand, 1988.

[32] John G Gualtieri, John A Kosinski, and Arthur Ballato. Piezoelectric materials for acoustic wave applications. *IEEE Transactions on Ultrasonics, Ferroelectrics, and Frequency Control*, 41(1):53–59, 1994.

[33] C Vale, J Rosenbaum, S Horwitz, S Krishnaswamy, and R Moore. Fbar filters at ghz frequencies. In *Frequency Control, 1990., Proceedings of the 44th Annual Symposium on*, pages 332–336. IEEE, 1990.

[34] P Osbond, CM Beck, CJ Brierley, MR Cox, SP Marsh, and NM Shorrocks. The influence of zno and electrode thickness on the performance of thin film bulk acoustic wave resonators. In *Ultrasonics Symposium, 1999. Proceedings. 1999 IEEE*, volume 2, pages 911–914. IEEE, 1999.

[35] J Molarius, J Kaitila, T Pensala, and M Ylilammi. Piezoelectric zno films by rf sputtering. *Journal of Materials Science: Materials in Electronics*, 14(5-7):431–435, 2003.

[36] H Jaffe and DA Berlincourt. Piezoelectric transducer materials. *Proceedings of the IEEE*, 53(10):1372–1386, 1965.

[37] Yih-Hsing Pao. Elastic waves in solids. *Journal of applied mechanics*, 50(4b):1152–1164, 1983.

[38] Morito Akiyama, Kazuhiko Kano, and Akihiko Teshigahara. Influence of growth temperature and scandium concentration on piezoelectric response of scandium aluminum nitride alloy thin films. *Applied Physics Letters*, 95(16):162107, 2009.

[39] Morito Akiyama, Toshihiro Kamohara, Kazuhiko Kano, Akihiko Teshigahara, Yukihiro Takeuchi, and Nobuaki Kawahara. Enhancement of piezoelectric response in scandium aluminum nitride alloy thin films prepared by dual reactive cosputtering. *Advanced Materials*, 21(5):593–596, 2009.

[40] Chih-Ming Lin, Yung-Yu Chen, Valery V Felmetsger, Debbie G Senesky, and Albert P Pisano. Aln/3c–sic composite plate enabling high-frequency and high-q micromechanical resonators. *Advanced Materials*, 24(20):2722–2727, 2012.

[41] Johan Bjurström, Ilia Katardjiev, and Ventsislav Yantchev. Lateral-field-excited thin-film lamb wave resonator. *Applied Physics Letters*, 86(15):154103, 2005.

[42] Johan Bjurström, Ventsislav Yantchev, and Ilia Katardjiev. Thin film lamb wave resonant structures–the first approach. *Solid-state electronics*, 50(3):322–326, 2006.

[43] Ventsislav Yantchev, Johannes Enlund, J Biurström, and Ilia Katardjiev. Design of high frequency piezoelectric resonators utilizing laterally propagating

fast modes in thin aluminum nitride (aln) films. *Ultrasonics*, 45(1-4):208–212, 2006.

[44] Ventsislav Yantchev, Lilia Arapan, and Ilia Katardjiev. Micromachined thin film plate acoustic wave resonators (fpar): Part ii. *IEEE transactions on ultrasonics, ferroelectrics, and frequency control*, 56(12), 2009.

[45] Gianluca Piazza, Philip J Stephanou, and Albert P Pisano. One and two port piezoelectric higher order contour-mode mems resonators for mechanical signal processing. *Solid-State Electronics*, 51(11-12):1596–1608, 2007.

[46] Matteo Rinaldi, Chiara Zuniga, Chengjie Zuo, and Gianluca Piazza. Super-high-frequency two-port aln contour-mode resonators for rf applications. *IEEE transactions on ultrasonics, ferroelectrics, and frequency control*, 57(1), 2010.

[47] Chengjie Zuo, Nipun Sinha, Jan Van der Spiegel, and Gianluca Piazza. Multifrequency pierce oscillators based on piezoelectric aln contour-mode mems technology. *Journal of Microelectromechanical Systems*, 19(3):570–580, 2010.

[48] Chih-Ming Lin, Yun-Ju Lai, Ting-Ta Yen, Jin-Chen Hsu, Yung-Yu Chen, Debbie G Senesky, and Albert P Pisano. Quality factor enhancement in lamb wave resonators utilizing aln plates with convex edges. In *Solid-State Sensors, Actuators and Microsystems Conference (TRANSDUCERS), 2011 16th International*, pages 1512–1515. IEEE, 2011.

[49] Chih-Ming Lin, Ventsislav Yantchev, Yung-Yu Chen, Valery V Felmetsger, and Albert P Pisano. Characteristics of aln lamb wave resonators with various bottom electrode configurations. In *Frequency Control and the European Frequency and Time Forum (FCS), 2011 Joint Conference of the IEEE International*, pages 1–5. IEEE, 2011.

[50] PJ Stephanou and AP Pisano. 800 mhz low motional resistance contour-extensional aluminum nitride micromechanical resonators. In *Tech. Dig. Solid-State Sens. Actuators Microsyst. Workshop*, pages 60–61, 2006.

[51] Chih-Ming Lin, Yun-Ju Lai, Jin-Chen Hsu, Yung-Yu Chen, Debbie G Senesky, and Albert P Pisano. High-q aluminum nitride lamb wave resonators with biconvex edges. *Applied Physics Letters*, 99(14):143501, 2011.

[52] I.A. Viktorov. *Rayleigh and Lamb Waves: Physical Theory and Applications*. Ultrasonic Technology. Springer US, 2013.

[53] Gunilla Wingqvist, Lilia Arapan, Ventsislav Yantchev, and Ilia Katardjiev. A micromachined thermally compensated thin film lamb wave resonator for frequency control and sensing applications. *Journal of Micromechanics and Microengineering*, 19(3):035018, 2009.

[54] Reza Abdolvand, Hedy Fatemi, and Sina Moradian. Quality factor and coupling in piezoelectric mems resonators. In *Piezoelectric MEMS Resonators*, pages 133–152. Springer, 2017.

[55] Zhili Hao, Ahmet Erbil, and Farrokh Ayazi. An analytical model for support loss in micromachined beam resonators with in-plane flexural vibrations. *Sensors and Actuators A: Physical*, 109(1):156–164, 2003.

[56] Zhili Hao and Farrokh Ayazi. Support loss in the radial bulk-mode vibrations of center-supported micromechanical disk resonators. *Sensors and Actuators A: Physical*, 134(2):582–593, 2007.

[57] Jing Wang, Zeying Ren, and CT-C Nguyen. 1.156-ghz self-aligned vibrating micromechanical disk resonator. *IEEE transactions on ultrasonics, ferroelectrics, and frequency control*, 51(12):1607–1628, 2004.

[58] Sheng-Shian Li, Yu-Wei Lin, Yuan Xie, Zeying Ren, and CT-C Nguyen. Micromechanical" hollow-disk" ring resonators. In *Micro Electro Mechanical Systems, 2004. 17th IEEE International Conference on.(MEMS)*, pages 821–824. IEEE, 2004.

[59] J Baborowski, C Bourgeois, A Pezous, C Muller, and M-A Dubois. Piezoelectrically activated silicon resonators. In *Frequency Control Symposium, 2007 Joint with the 21st European Frequency and Time Forum. IEEE International*, pages 1210–1213. IEEE, 2007.

[60] Johannes Gerardus Smits. *Eigenstates of coupling factor and loss factor of piezoelectric ceramics*. PhD thesis, Technische Hogeschool Twente, 1978.

[61] Paul Muralt. Aln thin film processing and basic properties. In *Piezoelectric MEMS Resonators*, pages 3–37. Springer, 2017.

[62] Paul Muralt, J Antifakos, M Cantoni, R Lanz, and F Martin. Is there a better material for thin film baw applications than **A1N**? In *Ultrasonics Symposium, 2005 IEEE*, volume 1, pages 315–320. IEEE, 2005.

[63] Kenneth M Lakin. Thin film resonator technology. *IEEE transactions on ultrasonics, ferroelectrics, and frequency control*, 52(5):707–716, 2005.

[64] KS Van Dyke. The electric network equivalent of a piezoelectric resonator. *Phys. Rev*, 25(6):895, 1925.

[65] Ken-ya Hashimoto, Shuhei Sato, Akihiko Teshigahara, Takuya Nakamura, and Kazuhiko Kano. High-performance surface acoustic wave resonators in the 1 to 3 GHz range using a ScAlN/6H-SiC structure. *IEEE transactions on ultrasonics, ferroelectrics, and frequency control*, 60(3):637–642, 2013.

[66] Akira Konno, Michio Kadota, Jun-ichi Kushibiki, Yuji Ohashi, Masayoshi Esashi, Yasuo Yamamoto, and Shuji Tanaka. Determination of full material constants of ScAlN thin film from bulk and leaky lamb waves in mems-based samples. In *Ultrasonics Symposium (IUS), 2014 IEEE International*, pages 273–276. IEEE, 2014.

[67] Markys G Cain. *Characterisation of ferroelectric bulk materials and thin films*. Springer, 2014.

[68] R Aigner, J Ella, H-J Timme, L Elbrecht, W Nessler, and S Marksteiner. Advancement of MEMS into RF-filter applications. In *Electron Devices Meeting, 2002. IEDM'02. International*, pages 897–900. IEEE, 2002.

[69] Bertram Alexander Auld. *Acoustic fields and waves in solids*. , 1973.

[70] Kazuo Tsubouchi and Nobuo Mikoshiba. Zero-temperature-coefficient saw devices on aln epitaxial films. *IEEE Transactions on Sonics Ultrasonics*, 32:634–644, 1985.

[71] H Iwanaga, A Kunishige, and S Takeuchi. Anisotropic thermal expansion in wurtzite-type crystals. *Journal of Materials Science*, 35(10):2451–2454, 2000.

[72] V Cimalla, J Pezoldt, and O Ambacher. Group iii nitride and sic based mems and nems: materials properties, technology and applications. *Journal of Physics D: Applied Physics*, 40(20):6386, 2007.

[73] Michael E Levinshtein, Sergey L Rumyantsev, and Michael S Shur. *Properties of Advanced Semiconductor Materials: GaN, AIN, InN, BN, SiC, SiGe*. John Wiley & Sons, 2001.

[74] John Frederick Nye. *Physical properties of crystals: their representation by tensors and matrices*. Oxford university press, 1985.

[75] M. Brissaud. *Matériaux piézoélectriques: caractérisation, modélisation et vibration*. Collection des sciences appliquées de l'INSA de Lyon. Matériaux. Presses polytechniques et universitaires romandes, 2007.

[76] R.E. Newnham. *Properties of Materials: Anisotropy, Symmetry, Structure*. OUP Oxford, 2004.

[77] T. Shiosaki, T. Yamamoto, T. Oda, K. Harada, and A. Kawabata. Low temperature growth of piezoelectric AlN film for surface and bulk wave transducers by RF reactive planar magnetron sputtering. *Applied Physics Letters*, 36:451–454, 1980.

[78] Marc-Alexandre Dubois. *Aluminium nitride and lead zirconate-titanate thin films for ultrasonic applications: integration, properties and devices*. PhD thesis, EPFL, 1999.

[79] KL. Wang, KM. Lakin, and JK. Liu. Growth and properties of silicon films on aluminum nitride films on sapphire. *Journal of Applied Physics*, 47(4):1580–1582, 1976.

[80] Characteristics of AlN thin films deposited by electron cyclotron resonance dual-ion-beam sputtering and their application to GHz-band surface acoustic wave devices. *Japanese journal of applied physics*, 33(5S):2957, 1994.

[81] J. R. Heffelfinger, D. L. Medlin, and K. F. McCarty. On the initial stages of AlN thin-film growth onto (0001) oriented Al_2O_3 substrates by molecular beam epitaxy. *Journal of Applied Physics*, 85(1), 1999.

[82] W. Lin, L. Meng, and H. Chen, G.and Liu. Epitaxial growth of cubic AlN films on (100) and (111) silicon by pulsed laser ablation. *Applied physics letters*, 66(16):2066–2068, 1995.

[83] AJ. Shuskus, TM. Reeder, and EL. Paradis. RF-sputtered aluminum nitride films on sapphire. *Applied Physics Letters*, 24(4):155–156, 1974.

[84] H. Cheng, Y. Sun, JX. Zhang, YB. Zhang, S. Yuan, and P. Hing. Aln films deposited under various nitrogen concentrations by RF reactive sputtering. *Journal of crystal growth*, 254(1):46–54, 2003.

[85] T. Hata, E. Noda, O. Morimoto, and T. Hada. High rate deposition of thick piezoelectric zno films using a new magnetron sputtering technique. *Applied Physics Letters*, 37(7):633–635, 1980.

[86] M. Dubois and P. Muralt. Properties of aluminum nitride thin films for piezoelectric transducers and microwave filter applications. *Applied Physics Letters*, 74(20):3032–3034, 1999.

[87] M. Dubois and P. Muralt. Stress and piezoelectric properties of aluminum nitride thin films deposited onto metal electrodes by pulsed direct current reactive sputtering. *Journal of Applied Physics*, 89(11):6389–6395, 2001.

[88] M. Clement, E. Iborra, J. Sangrador, A. Sanz-Hervs, L. Vergara, and M. Aguilar. Influence of sputtering mechanisms on the preferred orientation of aluminum nitride thin films. *Journal of Applied Physics*, 94(3), 2003.

[89] H. Cheng, Y. Sun, and P. Hing. The influence of deposition conditions on structure and morphology of aluminum nitride films deposited by radio frequency reactive sputtering. *Thin Solid Films*, 434(12):112 – 120, 2003.

[90] John A Thornton. The microstructure of sputter-deposited coatings. *Journal of Vacuum Science & Technology A: Vacuum, Surfaces, and Films*, 4(6):3059–3065, 1986.

[91] JA. Thornton and D.W. Hoffman. Stress-related effects in thin films. *Thin Solid Films*, 171(1):5 – 31, 1989.

[92] G.F. Iriarte, J.G. Rodrguez, and F. Calle. Synthesis of c-axis oriented *AlN* thin films on different substrates: A review. *Materials Research Bulletin*, 45(9):1039 – 1045, 2010.

[93] M. Akiyama, K. Nagao, N. Ueno, H. Tateyama, and T. Yamada. Influence of metal electrodes on crystal orientation of aluminum nitride thin films. *Vacuum*, 74(3):699–703, 2004.

[94] J. Bai, X. Huang, and M. Dudley. High-resolution TEM observation of aln grown on on-axis and off-cut *SiC* substrates. *Materials Science in Semiconductor Processing*, 9(13):180 – 183, 2006.

[95] M. Ishihara, T. Nakamura, F. Kokai, and Y. Koga. Preparation of *AlN* and $LiNbO_3$ thin films on diamond substrates by sputtering method. *Diamond and Related Materials*, 11(36):408 – 412, 2002.

[96] R. Lanz and P. Muralt. Solidly mounted BAW filters for 8 GHz based on AlN thin films. *Ultrasonics, 2003 IEEE Symposium*, 1:178–181, 2003.

[97] H.P. Loebl, M. Klee, C. Metzmacher, W. Brand, R. Milsom, and P. Lok. Piezoelectric thin *AlN* films for Bulk Acoustic Wave (BAW) resonators. *Materials Chemistry and Physics*, 79(2-3):143–146, 2003.

[98] F. Martin, P. Muralt, M. Dubois, and A. Pezous. Thickness dependence of the properties of highly c-axis textured AlN thin films. *Journal of Vacuum Science Technology A*, 22(2):361–365, 2004.

[99] J. Bjurström. *Advanced thin film electroacoustic devices*. Acta Universitatis Upsaliensis, 2007.

[100] F. Bi and B. Barber. Bulk acoustic wave RF technology. *IEEE Microwave Magazine*, 2008.

[101] R. Ruby. Review and comparison of bulk acoustic wave FBAR, SMR technology. *Ultrasonics Symposium, IEEE*, 2007.

[102] JT. Luo, B. Fan, F. Zeng, and F. Pan. Influence of Cr-doping on microstructure and piezoelectric response of AlN films. 2009.

[103] A. Kabulski, V. R. Pagn, and D. Korakakis. Erbium alloyed aluminum nitride films for piezoelectric applications. 1129, 2008.

[104] H. Liu, F. Zeng, G. Tang, and F. Pan. Enhancement of piezoelectric response of diluted ta doped AlN . *Applied Surface Science*, 270(0):225 – 230, 2013.

[105] M. Akiyama, K. Kano, and A. Teshigahara. Influence of growth temperature and scandium concentration on piezoelectric response of scandium aluminum nitride alloy thin films. *Applied Physics Letters*, 95(16), 2009.

[106] A Alsaad and A Ahmad. Piezoelectricity of ordered $Sc_xAl_{1-x}N$ alloys from first principles. *The European Physical Journal B-Condensed Matter and Complex Systems*, 54(2):151–156, 2006.

[107] G. Piazza, V. Felmetsger, P. Muralt, Roy H. RH. Olsson III, and R. Ruby. Piezoelectric aluminum nitride thin films for microelectromechanical systems. *MRS bulletin*, 37(11):1051–1061, 2012.

[108] F. Tasnadi, B. Alling, C. Höglund, G. Wingqvist, J. Birch, L. Hultman, and I. Abrikosov. Origin of the anomalous piezoelectric response in wurtzite $Sc_xAl_{1-x}N$ alloys. *Physical review letters*, 104(13):137601, 2010.

[109] R Matloub, Mahmoud Hadad, Andrea Mazzalai, Nachiappan Chidambaram, Gilles Moulard, CS Sandu, Th . Metzger, and Paul Muralt. Piezoelectric $Sc_xAl_{1-x}N$ thin films: a semiconductor compatible solution for mechanical energy harvesting and sensors. *Applied Physics Letters*, 102(15):152903, 2013.

[110] Ruopeng Deng, Sarah R Evans, and Daniel Gall. Bandgap in $Sc_xAl_{1-x}N$. *Applied Physics Letters*, 102(11):112103, 2013.

[111] Ramin Matloub, Alvaro Artieda, Cosmin Sandu, Evgeny Milyutin, and Paul Muralt. Electromechanical properties of $Sc_{0.1}Al_{0.9}N$ thin films evaluated at 2.5 GHz film bulk acoustic resonators. *Applied Physics Letters*, 99(9):092903, 2011.

[112] Milena Moreira, Johan Bjurström, Ilia Katardjev, and Ventsislav Yantchev. Aluminum scandium nitride thin-film bulk acoustic resonators for wide band applications. *Vacuum*, 86(1):23–26, 2011.

[113] Miguel A Caro, Siyuan Zhang, Tommi Riekkinen, Markku Ylilammi, Michelle A Moram, Olga Lopez-Acevedo, Jyrki Molarius, and Tomi Laurila. Piezoelectric coefficients and spontaneous polarization of ScAlN. *Journal of Physics: Condensed Matter*, 27(24):245901, 2015.

[114] Andrea Mazzalai, Davide Balma, Nachiappan Chidambaram, Ramin Matloub, and Paul Muralt. Characterization and fatigue of the converse piezoelectric effect in pzt films for mems applications. *Journal of Microelectromechanical Systems*, 24(4):831–838, 2015.

[115] Milton Ohring. *Materials science of thin films*. Elsevier, 2001.

[116] Rajan S Naik, Joseph J Lutsky, Rafael Reif, Charles G Sodini, Andy Becker, Linus Fetter, Harold Huggins, Ronald Miller, John Pastalan, Gee Rittenhouse, et al. Measurements of the bulk, c-axis electromechanical coupling constant as a function of aln film quality. *IEEE transactions on ultrasonics, ferroelectrics, and frequency control*, 47(1):292–296, 2000.

[117] HP Löbl, M Klee, R Milsom, R Dekker, C Metzmacher, W Brand, and P Lok. Materials for bulk acoustic wave (baw) resonators and filters. *Journal of the European Ceramic Society*, 21(15):2633–2640, 2001.

[118] AL Kholkin, Ch Wütchrich, DV Taylor, and N Setter. Interferometric measurements of electric field-induced displacements in piezoelectric thin films. *Review of scientific instruments*, 67(5):1935–1941, 1996.

[119] Fazel Parsapour, Vladimir Pashchenko, Stefan Mertin, Cosmin Sandu, Nicolas Kurz, Pascal Nicolay, and Paul Muralt. Ex-situ aln seed layer for (0001)-textured al 0.84 sc 0.16 n thin films grown on sio 2 substrates. In *Ultrasonics Symposium (IUS), 2017 IEEE International*, pages 1–4. IEEE, 2017.

[120] Wenbo Wang, Patrick M Mayrhofer, Xingli He, Manuel Gillinger, Zhi Ye, Xiaozhi Wang, Achim Bittner, Ulrich Schmid, and JK Luo. High performance AlScN thin film based surface acoustic wave devices with large electromechanical coupling coefficient. *Applied Physics Letters*, 105(13):133502, 2014.

[121] Evgeny Milyutin, Sandrine Gentil, and Paul Muralt. Shear mode bulk acoustic wave resonator based on c-axis oriented aln thin film. *Journal of Applied Physics*, 104(8):084508, 2008.

[122] A Fardeheb-Mammeri, MB Assouar, O Elmazria, C Gatel, JJ Fundenberger, and B Benyoucef. C-axis inclined aln film growth in planar system for shear wave devices. *Diamond and Related Materials*, 17(7):1770–1774, 2008.

[123] Alvaro Artieda and Paul Muralt. High-q aln/sio 2 symmetric composite thin film bulk acoustic wave resonators. *IEEE transactions on ultrasonics, ferroelectrics, and frequency control*, 55(11), 2008.

[124] Agnė Žukauskaitė, Christopher Tholander, Ferenc Tasnádi, Björn Alling, Justinas Palisaitis, Jun Lu, Per OÅ Persson, Lars Hultman, and Jens Birch. Stabilization of wurtzite sc0. 4al0. 6n in pseudomorphic epitaxial scxal1-xn/inyal1- yn superlattices. *Acta Materialia*, 94:101–110, 2015.

[125] Dariusz Burak, Stefan Bader, Alexandre Shirakawa, and Kevin J Grannen. Acoustic resonator comprising acoustic redistribution layers, January 17 2017. US Patent 9,548,438.

[126] Cosmin Silviu Sandu, Fazel Parsapour, Stefan Mertin, Vladimir Pashchenko, Ramin Matloub, Thomas LaGrange, Bernd Heinz, and Paul Muralt. Abnormal grain growth in alscn thin films induced by complexion formation at crystallite interfaces. *physical status solidi (a)*, 0(0):1800569.

[127] Simon Fichtner, Niklas Wolff, Gnanavel Krishnamurthy, Adrian Petraru, Sascha Bohse, Fabian Lofink, Steffen Chemnitz, Hermann Kohlstedt, Lorenz Kienle, and Bernhard Wagner. Identifying and overcoming the interface originating c-axis instability in highly Sc enhanced aln for piezoelectric microelectromechanical systems. *Journal of Applied Physics*, 122(3):035301, 2017.

[128] Stefan Mertin, Bernd Heinz, Oliver Rattunde, Gabriel Christmann, Marc-Alexandre Dubois, Sylvain Nicolay, and Paul Muralt. Piezoelectric and structural properties of c-axis textured aluminium scandium nitride thin films up to high scandium content. *Surface and Coatings Technology*, 343:2–6, 2018.

[129] Yuan Lu, Markus Reusch, Nicolas Kurz, Anli Ding, Tim Christoph, Lutz Kirste, Vadim Lebedev, and Agnė Žukauskaitė. Surface morphology and microstructure of pulsed dc magnetron sputtered piezoelectric aln and alscn thin films. *physica status solidi (a)*, 215(9):1700559, 2018.

[130] M Ishihara, SJ Li, H Yumoto, K Akashi, and Y Ide. Control of preferential orientation of aln films prepared by the reactive sputtering method. *Thin Solid Films*, 316(1-2):152–157, 1998.

[131] Viktor Hrkac, Aaron Kobler, Stephan Marauska, Adrian Petraru, Ulrich Schürmann, Venkata Sai Kiran Chakravadhanula, Viola Duppel, Hermann Kohlstedt, Bernhard Wagner, Bettina Valeska Lotsch, et al. Structural study of growth, orientation and defects characteristics in the functional microelectromechanical system material aluminium nitride. *Journal of Applied Physics*, 117(1):014301, 2015.

[132] Olaf Zywitzki, Thomas Modes, Stephan Barth, Hagen Bartzsch, and Peter Frach. Effect of scandium content on structure and piezoelectric properties of alscn films deposited by reactive pulse magnetron sputtering. *Surface and Coatings Technology*, 309:417–422, 2017.

[133] PM Mayrhofer, H Riedl, H Euchner, M Stöger-Pollach, PH Mayrhofer, A Bittner, and U Schmid. Microstructure and piezoelectric response of yxal1-xn thin films. *Acta Materialia*, 100:81–89, 2015.

[134] S Nicolay, S Fay, and C Ballif. Growth model of mocvd polycrystalline zno. *Crystal growth & design*, 9(11):4957–4962, 2009.

[135] Agne Zukauskaite, Gunilla Wingqvist, Justinas Palisaitis, Jens Jensen, Per OÅ Persson, Ramin Matloub, Paul Muralt, Yunseok Kim, Jens Birch, and Lars Hultman. Microstructure and dielectric properties of piezoelectric magnetron sputtered w-scxal1- xn thin films. *Journal of Applied Physics*, 111(9):093527, 2012.

[136] EF Rauch and M Véron. Automated crystal orientation and phase mapping in TEM. *Materials Characterization*, 98:1–9, 2014.

[137] Jochen Lohmiller, Aaron Kobler, Ralph Spolenak, and Patric A Gruber. The effect of solute segregation on strain localization in nanocrystalline thin films: Dislocation glide vs. grain-boundary mediated plasticity. *Applied Physics Letters*, 102(24):241916, 2013.

[138] Alistair Garner, Jing Hu, Allan Harte, Philipp Frankel, Chris Grovenor, Sergio Lozano-Perez, and Michael Preuss. The effect of sn concentration on oxide texture and microstructure formation in zirconium alloys. *Acta Materialia*, 99:259–272, 2015.

[139] Vibhu Jindal and Fatemeh Shahedipour-Sandvik. Density functional theoretical study of surface structure and adatom kinetics for wurtzite aln. *Journal of Applied Physics*, 105(8):084902, 2009.

[140] Ruopeng Deng, Paul Muralt, and Daniel Gall. Biaxial texture development in aluminum nitride layers during off-axis sputter deposition. *Journal of Vacuum Science & Technology A: Vacuum, Surfaces, and Films*, 30(5):051501, 2012.

[141] Fabrice Martin, Marc-Etienne Jan, Samuel Rey-Mermet, Brahim Belgacem, Dong Su, Marco Cantoni, and Paul Muralt. Shear mode coupling and tilted grain growth of AlN thin films in BAW resonators. *IEEE transactions on ultrasonics, ferroelectrics, and frequency control*, 53(7):1339–1343, 2006.

[142] E Milyutin, S Harada, D Martin, JF Carlin, N Grandjean, V Savu, O Vaszquez-Mena, J Brugger, and P Muralt. Sputtering of (001) aln thin films: control of polarity by a seed layer. *Journal of Vacuum Science & Technology B, Nanotechnology and Microelectronics: Materials, Processing, Measurement, and Phenomena*, 28(6):L61–L63, 2010.

[143] Stijn Mahieu, Pieter Ghekiere, Diederik Depla, and Roger De Gryse. Biaxial alignment in sputter deposited thin films. *Thin Solid Films*, 515(4):1229–1249, 2006.

[144] JM Nieuwenhuizen and HBi HAANSTRA. Microfractography of thin films. *Philips Tech Rev*, 27(3):87–91, 1966.

[145] RD T Shannon and C Tfc Prewitt. Effective ionic radii in oxides and fluorides. *Acta Crystallographica Section B: Structural Crystallography and Crystal Chemistry*, 25(5):925–946, 1969.

[146] PM Mayrhofer, A Bittner, and U Schmid. High temperature stability of$Sc_xAl_{1-x}N$ (x= 0.27) thin films. In *Smart Sensors, Actuators, and MEMS VII; and Cyber Physical Systems*, volume 9517, page 95171C. International Society for Optics and Photonics, 2015.

[147] Gianluca Piazza, Philip J Stephanou, and Albert P Pisano. Piezoelectric aluminum nitride vibrating contour-mode MEMS resonators. *Journal of Microelectromechanical Systems*, 15(6):1406–1418, 2006.

[148] Gianluca Piazza, Philip J Stephanou, and Albert P Pisano. Single-chip multiple-frequency AlN MEMS filters based on contour-mode piezoelectric resonators. *Journal of MicroElectroMechanical Systems*, 16(2):319–328, 2007.

[149] LF Johnson. Evolution of grating profiles under ion-beam erosion. *Applied optics*, 18(15):2559–2574, 1979.

[150] D Zhuang and JH Edgar. Wet etching of gan, aln, and sic: a review. *Materials Science and Engineering: R: Reports*, 48(1):1–46, 2005.

[151] CB Vartuli, SJ Pearton, CR Abernathy, JD MacKenzie, F Ren, JC Zolper, and RJ Shul. Wet chemical etching survey of iii-nitrides. *Solid-State Electronics*, 41(12):1947–1951, 1997.

[152] A. Artieda, C. Sandu, and P. Muralt. Highly piezoelectric AlN thin films grown on amorphous, insulating substrates. *Journal of Vacuum Science and Technology. A, International Journal Devoted to Vacuum, Surfaces, and Films*, 28(3), 2010.

[153] Simon Fichtner, Tim Reimer, Steffen Chemnitz, Fabian Lofink, and Bernhard Wagner. Stress controlled pulsed direct current co-sputtered al1- xscxn as piezoelectric phase for micromechanical sensor applications. *APL Materials*, 3(11):116102, 2015.

[154] M Sinusía Lozano, A Pérez-Campos, M Reusch, L Kirste, Th Fuchs, A Žukauskaitė, Z Chen, and GF Iriarte. Piezoelectric characterization of sc0. 26al0. 74n layers on si (001) substrates. *Materials Research Express*, 5(3):036407, 2018.

[155] Morito Akiyama, Keiichi Umeda, Atsushi Honda, and Toshimi Nagase. Influence of scandium concentration on power generation figure of merit of scandium aluminum nitride thin films. *Applied Physics Letters*, 102(2):021915, 2013.

[156] R. Lanz and P. Muralt. Bandpass filters for 8 GHz using solidly mounted bulk acoustic wave resonators. *Ultrasonics, Ferroelectrics, and Frequency Control, IEEE Transactions*, 52(6):938–948, 2005.

[157] Jizhou Zhou, M DeMiguel-Ramos, Luis Garcia-Gancedo, Enrique Iborra, Jimena Olivares, Hao Jin, JK Luo, AS Elhady, SR Dong, DM Wang, et al. Characterisation of aluminium nitride films and surface acoustic wave devices for microfluidic applications. *Sensors and Actuators B: Chemical*, 202:984–992, 2014.

[158] MA Moram and S Zhang. ScGaN and ScAlN: emerging nitride materials. *Journal of Materials Chemistry A*, 2(17):6042–6050, 2014.

[159] Gongbin Tang, Tao Han, Qiaozhen Zhang, Kenta Yamazaki, Tatsuya Omori, and Ken-ya Hashimoto. Validity evaluation of $Al_{1-x}Sc_xN$ material constants based on SAW characteristics. *Journal of Micromechanics and Microengineering*, 26(11):115002, 2016.

[160] K Tsubouchi, K Sugai, and N Mikoshiba. AlN material constants evaluation and SAW properties on AlN/Al_2O_3 and AlN/Si. In *1981 Ultrasonics Symposium*, pages 375–380. IEEE, 1981.

[161] GF Iriarte, JG Rodríguez, and F Calle. Synthesis of c-axis oriented aln thin films on different substrates: A review. *Materials Research Bulletin*, 45(9):1039–1045, 2010.

[162] A Fardeheb-Mammeri, MB Assouar, O Elmazria, JJ Fundenberger, and B Benyoucef. Growth and characterization of c-axis inclined AlN films for shear wave devices. *Semiconductor Science and Technology*, 23(9):095013, 2008.

[163] Parsapour Fazel Kurz, Nicolas, Vladimir Pashchenko, Lutz Kriste, Vadim Lebedev, , Pascal Nicolay, Paul Muralt, and Oliver Ambacher. Determination of elastic and piezoelectric properties of al0.84sc0.16n thin films. In *Ultrasonics Symposium (IUS), 2018 IEEE International*, pages 1–4. IEEE, 208.

[164] Miguel Algueró, Carlos Alemany, Lorena Pardo, and Amador M González. Method for obtaining the full set of linear electric, mechanical, and electromechanical coefficients and all related losses of a piezoelectric ceramic. *Journal of the American Ceramic Society*, 87(2):209–215, 2004.

[165] Akira Konno, Masahiro Sumisaka, Akihiko Teshigahara, Kazuhiko Kano, Ken-ya Hashimo, Hideki Hirano, Masayoshi Esashi, Michio Kadota, and Shuji Tanaka. ScAlN lamb wave resonator in GHz range released by XeF_2 etching. In *Ultrasonics Symposium (IUS), 2013 IEEE International*, pages 1378–1381. IEEE, 2013.

[166] P Bergese, E Bontempi, and LE Depero. A simple solution to systematic errors in density determination by X-ray reflectivity: The XRR-density evaluation (XRR-DE) method. *Applied surface science*, 253(1):28–32, 2006.

[167] Vaclav Holy, Tilo Baumbach, and Ullrich Pietsch. *High-resolution X-ray scattering from thin films and multilayers*. Springer, 1999.

[168] Walter L Bond. The mathematics of the physical properties of crystals. *Bell Labs Technical Journal*, 22(1):1–72, 1943.

[169] Takahiko Yanagitani. Shear mode piezoelectric thin film resonators. In *Acoustic Waves-From Microdevices to Helioseismology*. InTech, 2011.

[170] Daniel Royer and Eugene Dieulesaint. *Elastic waves in solids II: generation, acousto-optic interaction, applications*. Springer Science & Business Media, 1999.

[171] NF Foster, GA Coquin, GA Rozgonyi, and FA Vannatta. Cadmium sulphide and zinc oxide thin-film transducers. *IEEE Transactions on Sonics and Ultrasonics*, 15(1):28–40, 1968.

[172] Hayato Ichihashi, Takahiko Yanagitani, Masashi Suzuki, Shinji Takayanagi, and Mami Matsukawa. Effect of Sc concentration on shear wave velocities in ScAlN films measured by micro-brillouin scattering technique. In *Ultrasonics Symposium (IUS), 2014 IEEE International*, pages 2521–2524. IEEE, 2014.

[173] C Deger, E Born, H Angerer, O Ambacher, M Stutzmann, J Hornsteiner, E Riha, and G Fischerauer. Sound velocity of $Al_{1-x}Sc_xN$ thin films obtained by surface acoustic-wave measurements. *Applied Physics Letters*, 72(19):2400–2402, 1998.

[174] Gunilla Wingqvist. AlN -based sputter-deposited shear mode thin film bulk acoustic resonator (FBAR) for biosensor applications-a review. *Surface and Coatings Technology*, 205(5):1279–1286, 2010.

[175] Thomas LaGrange, Kazuto Arakawa, Hidehiro Yasuda, and Mukul Kumar. Preferential void formation at crystallographically ordered grain boundaries in nanotwinned copper thin films. *Acta Materialia*, 96:284–291, 2015.

[176] Thomas LaGrange, Bryan W Reed, Mark Wall, Jeremy Mason, Troy Barbee, and Mukul Kumar. Topological view of the thermal stability of nanotwinned copper. *Applied Physics Letters*, 102(1):011905, 2013.

[177] Philip E Bloomfield. Multilayer transducer transfer matrix formalism. *IEEE transactions on ultrasonics, ferroelectrics, and frequency control*, 49(9):1300–1311, 2002.

[178] Ventsislav Yantchev and Ilia Katardjiev. Thin film lamb wave resonators in frequency control and sensing applications: a review. *Journal of Micromechanics and Microengineering*, 23(4):043001, 2013.

[179] Chih-Ming Lin, Ventsislav Yantchev, Jie Zou, Yung-Yu Chen, and Albert P Pisano. Micromachined one-port aluminum nitride lamb wave resonators utilizing the lowest-order symmetric mode. *Journal of microelectromechanical systems*, 23(1):78–91, 2014.

[180] Jie Zou, Chih-Ming Lin, CS Lam, and Albert P Pisano. Transducer design for aln lamb wave resonators. *Journal of Applied Physics*, 121(15):154502, 2017.

[181] Fazel Parsapour, Vladimir Pashchenko, Nicokas Kruz, Cosmin Sandu, La-Grangec Tomas, Yamashitad Kaoro, Lebedeve Vadim, and Muralt Paul. Material parameter extraction for complex alscn thin film using dual mode resonators in combination with advanced microstructural analysis and finite element modeling. *Submitted to Advanced functional materils.*

[182] Sumy Jose, Andre BM Jansman, Raymond JE Hueting, and Jurriaan Schmitz. Optimized reflector stacks for solidly mounted bulk acoustic wave resonators. *IEEE transactions on ultrasonics, ferroelectrics, and frequency control*, 57(12), 2010.

[183] Tuomas Pensala et al. *Thin film bulk acoustic wave devices: Performance optimization and modeling.* VTT, 2011.

[184] Hongxiang Zhang, Ji Liang, Xiaoyan Zhou, Hao Zhang, Daihua Zhang, and Wei Pang. Transverse mode spurious resonance suppression in lamb wave mems resonators: theory, modeling, and experiment. *IEEE Transactions on Electron Devices*, 62(9):3034–3041, 2015.

[185] Jeronimo Segovia-Fernandez, Massimiliano Cremonesi, Cristian Cassella, Attilio Frangi, and Gianluca Piazza. Anchor losses in aln contour mode resonators. *Journal of microelectromechanical systems*, 24(2):265–275, 2015.

Fazel Parsapour | Doctoral Assistant-EPFL

Avenue du Tir-Federal 100 – 1024 Ecublens, Switzerland
(+41)78 773 40 73 • fazel.parsapour@gmail.com

Education

PhD Student — **EPFL-Lausanne-Switzerland**
Electroceramic Thin Films Group. — *2014–2018*

Master of Science — **EPFL-Lausanne-Switzerland**
Materials Science and Engineering — *2011–2014*

Bachelor of Science — **University of Tehran-Iran**
Materials Science and Engineering — *2006–2010*

High School — **Allame Tehran-Iran**
NODET,National Organizatitin for Development of EXpetinal Talents — *2002–2006*

Projects/Thesis

Ph.D Thesis

Title: *Growth, Integration and Functional Characterization of AlScN Thin Films for RF MEMS Devices*

Period: August 2014 -Dec 2018. EPFL, Electroceramic Thin Films Group. Under Supervision of Prof.Paul Muralt.

Master Thesis

Title: *Thermally Stimulated Currents In Ferroelectric Materials*

Period: October. 2013 - March 2014. EPFL, Ceramic Lab, Under Supervision of Prof. Dragan Damjanovic.

Internship

Title: *Long Pulse IR Laser Welding of Ultra Thin Glass Sheets*

Period: March 2012 -September 2012. EMPA, Advanced materils processing Lab. Under supervision of Prof.Patrik Hoffmann.

Master Semester Project

Title: *Electro-Mechanical Properties of Electro-Ceramics*

Period: February-June. 2011-EPFL. Ceramic Lab, Under Supervision of Prof. Dragan Damjanovic.

Bachelor Thesis

Title: *Investigation of Mechanical Properties and Impression Creep Behavior of $Sn_{31.1}Pb_{3.4}Zn$ Solder Alloy.*

Period: May 2029-May 2010. 2011- University of Tehran, Metals Formability Laboratory, Under Supervision of Prof. Reza Mahmoudi.

Skills

Microfabrication: Process flows design, Masks design, Photolithography, Dry and Wet etching techniques, Thin film deposition, Vacuum technology, Advanced laser processing.

Characterisation: Electrical and mechanical characterization of thin films, Electron microscopy, XRD, Spectroscopy.

Programming And Softwares: Matlab, Comsol, Origin, Expert Layout, LaTeX, Inkscape, Microsoft Office.

Honors and Awards

• Awarded 50k-CHF Research Grant for Research in AlScN based RF MEMS-Hasler foundation, Switzerland,2018.

• Awarded Fellowship for Graduate Studies-KIKO industrial group, Iran, 2014.

• Exceptional Talents Admission for High School. National Organization of Development of Exceptional Talents, Tehran, Iran, 2002.

Languages

English:Fluent **French**:Intermediate(A2-B1) **Arabic**:Intermediate **Persian**:Mother tongue

Publications

• Free Standing and Solidly Mounted Lamb Wave Resonators Based on $Al_{0.85}Sc_{0.15}N$ Thin Film. *To be submitted.*

• Material Parameter Extraction for Complex AlScN Thin Film Using Dual Mode Resonators in Combination with Advanced Microstructural Analysis and Finite Element Modeling. *Submitted to Advanced Functional Materials.*

• Abnormal Grain Growth in AlScN Thin Films Induced by Complexion Formation at Crystallite Interfaces. *Physical status solidi (a). Page 1800569, year 2018.*

• Ex-situ AlN Seed Layer for (0001)-Textured $Al_{0.16}Sc_{0.84}N$ Thin Films Grown on SiO_2 Substrates. *IEEE Ultrasonic Symposium 2017.*

• Effective SAW Excitations on Non-Piezoelectric Substrate using AlScN Piezoelectric Thin Film BAW/SAW Hybrid transducer. *IEEE Ultrasonic Symposium 2017.*

• Properties of AlScN Thin Films for Hybrid BAW/SAW Resonator Fabrication. *European frequency and time forum 2017.*

• Hybrid BAW/SAW AlN and AlScN thin film resonator. *IEEE Ultrasonic Symposium 2016.*

Extracurricular Activities and Interests

• Semi-professional ultimate frisbee player, Member of Flyhigh Lausanne, Swiss champion 2016.

Ce document a été imprimé au Centre d'impression EPFL,
imprimerie climatiquement neutre, certifiée myClimate.